Wrocław University of Technology
Centre of Advanced Materials and Nanotechnology

Materials Science

Towards Molecular Magnets

Vol. 21 No. 2 2003

Oficyna Wydawnicza Politechniki Wrocławskiej

Materials Science is an interdisciplinary journal devoted to experimental and theoretical research into the synthesis, structure, properties and applications of materials.

Among the materials of interest are:

- glasses and ceramics
- sol-gel materials
- photoactive materials (including materials for nonlinear optics)
- laser materials
- photonic crystals
- semiconductor micro- and nanostructures
- piezo-, pyro- and ferroelectric materials
- high-T_c, superconductors
- magnetic materials
- molecular materials (including polymers) for use in electronics and photonics
- novel solid phases
- other novel and unconventional materials

The broad spectrum of the areas of interest reflects the interdisciplinary nature of materials research. Papers covering the modelling of materials, their synthesis and characterisation, physicochemical aspects of their fabrication, properties and applications are welcome. In addition to regular papers, the journal features issues containing conference papers, as well as special issues on key topics in materials science.

Materials Science is published under the auspices of the Centre of Advanced Materials and Nanotechnology of the Wrocław University of Technology, in collaboration with the Institute of Low Temperatures and Structural Research of the Polish Academy of Sciences and the Wroclaw University of Economics.

All accepted papers are placed on the Web page of the journal and are available at the address:
http://MaterialsScience.pwr.wroc.pl

The journal is supported by the State Committee for Scientific Research

Editorial Office

Łukasz Maciejewski

Editorial layout

Hanna Basarowa

Printed in Poland

Drukarnia Oficyny Wydawniczej Politechniki Wrocławskiej
Zam. nr 399/2003.

Contents

Towards Molecular Magnets

Regular papers

Materials Science, Vol. 21, No. 2, 2003

New trends in the investigations of macrocyclic magnets*

J. MROZIŃSKI[1**], A. TOMKIEWICZ[1], M. NAHORSKA[1], B. KORYBUT-DASZKIEWICZ[2]

[1]Faculty of Chemistry, University of Wrocław, F. Joliot-Curie 14, 50-383 Wrocław, Poland

[2]Institute of Organic Chemistry, Polish Academy of Sciences, Kasprzaka 44, 01-224 Warszawa, Poland

A study of a series of new type of copper(II), nickel(III) and rhenium(IV) macrocyclic complexes, having an important meaning as macrocyclic magnets is reported. Their magnetic measurements have been carried out over the temperature range 1.8 – 300 K using a Quantum Design SQUID magnetometer (MPMSxL - 5 type). The results indicate that all of them behave as weakly interacting magnets.

Key words: *heterobimetallic magnets; copper(II); nickel(III) and rhenium(IV) complexes; magnetic behaviour*

1. Introduction

In recent years, a great interest has been paid to heterometallic systems obtained on the basis of polyamine complexes and of salts derived from Prussian blue [1]. The literature covering an analogous system in which the thiocyanate group plays the role of a bridging ligand is much more scarce [2]. Due to its ambident character, the thiocyanate group, like the cyanide one, may serve as a bridging ligand. Among a large group of polyamine complexes used for the synthesis of such systems, there are planar tetra-azo copper(II) and nickel(II) complexes. They are all by the square symmetry of the metal ion, owing to which there are additional two free coordinating sites at the axial positions. The access to the metal ion is very easy when there are no substituents in the macrocyclic ring. This situation changes with the size and character of substituents, which may form a steric hindrance, preventing any coordination to the metal ion. Cyclam and its substituted derivatives [2a, 3] are the most widespread tetra-azo macrocyclic ligands. Considering the fact that in unsaturated complexes of the [14]

---

*The paper was presented at the 13th Winter School on Coordination Chemistry, Karpacz, Poland, 9–13 December, 2002.

**Corresponding author, e-mail: jmroz@wchuwr.chem.uni.wroc.pl.

dieneN$_4$ type, the N-configuration of the macrocyclic ring influences its conformation, and hence the arrangement of substitutents [4], an attempt was undertaken to study the relation between the N-configuration and the crystal structure and magnetic properties of the compounds obtained [2b].

Bivalent [Ni^{II}LCl$_2$] and trivalent nickel complexes [Ni^{III}LCl$_2$]X, (X = Cl^-, ClO_4^-), are especially interesting because of their importance in biological systems [5, 6] and catalytic oxidation reactions [7, 8]. Both nickel ions form exceptionally stable crystals with an octahedral geometry of Ni(II) and Ni(III) surround and a square-planar array of four nitrogen atoms and two Cl^- anions occupying the axial positions [9]. The nickel(II) high-spin complexes with a d^8 electron configuration present the same stereochemistry as that of the corresponding Ni(III) analogues whilst the last one is of the low-spin d^7 configuration, and contains one unpaired electron (S = ½). The properties of macrocyclic nickel complexes were investigated using magnetic and spectroscopic methods [10].

The growing need for macrocyclic ligands and their complexes has stimulated research efforts for methods of their preparation and for studying their interesting chemical and physical properties. In particular, polynuclear systems are interesting because of their magnetic interaction between metallic centres. For this reason, we synthesized a new series of highly unsaturated copper(II) macrocyclic complexes [CuL]X$_2$ (where L = 6,13-bis(dodecylaminomethylidene)-1,4,8,11-tetrazacyclotetradeca-4,7,11,14-tetraene, X = Cl^-, Br^-, PF_6^-) [11]. Magnetic properties of these compounds were compared indicating that all copper compounds studied behave as weakly interacting magnets. On the other hand, the synthesis of heteropolymetallic systems with extended structures frequently consists in self-assembly processes involving anionic building blocks, which contain a paramagnetic ion, and in assembling complexed cations able of interacting with them [12]. We present also the magnetic properties of a system built of a highly unsaturated cyclidene copper(II) complex cation and hexachlororhenium(IV) or hexabromorhenium(IV) anions.

2. Experimental

2.1. Syntheses of the complexes

All chemicals were reagent grade and were used as commercially obtained. Ni(III) complexes, [Ni^{III}LCl$_2$]$^+$, containing tetraaza macrocyclic ligands with different number of methyl groups (L = [14]aneN$_4$ (L^1), 2-Me[14]aneN$_4$ (L^2), 5,12-Me$_2$[14]aneN$_4$ (L^3), 5,7,7,12,14,14-Me$_6$[14]aneN$_4$ (L^4)) were obtained from the corresponding nickel(II) complexes by oxidation with hydrogen peroxide [13].

Complexes of [CuL]X$_2$ were prepared according to [11]. Nearly unsoluble complexes : [CuL]ReCl$_6$·H$_2$O and [CuL]ReBr$_6$ were precipitated from acetonitrile solution of [CuL](PF$_6$)$_2$ with an excess of [Bu$_4$N]$_2$ReCl$_6$ or [Bu$_4$N]$_2$ReBr$_6$, respectively.

2.2. Magnetic measurements

Magnetic studies of powdered samples were carried out by the Faraday and SQUID methods. The Faraday-method measurements were carried out over the 4.5 –300 K range of temperatures using a $Hg[Co(NCS)_4]$ standard for which the value of the gram susceptibility equals 16.44×10^{-6} $cm^3\cdot g^{-1}$ at T = 293.1 K. The magnetic susceptibility of the powdered samples was measured over the temperature range of 1.9 –300 K using a Quantum Design SQUID-based MPMSXL-5-type magnetometer. The superconducting magnet was generally operated at field strengths ranging from 0.1 to 5 T. The SQUID magnetometer was calibrated with a palladium rod sample for which the gram magnetic susceptibility was taken as 5.30×10^{-6} $cm^3\cdot g^{-1}$ at T = 293.1 K. The corrections for diamagnetism were estimated from the Pascal constants [14].

2.3 Spectroscopic measurements

FIR spectra (500–100 cm^{-1}) were measured in Nujol mull and the MIR spectra (4000–500 cm^{-1}) in KBr pellets with a Bruker IFS 113 V Spectrophotometer.

Solid state EPR spectra were recorded in the 300–77 K temperature range with a Bruker E600 spectrometer. Reflectance spectra have been recorded with a Beckmann UV 5240 spectrophotometer in the range of 350–2500 nm.

3. Results and discussion

Magnetic susceptibility measurements of investigated complexes [Ni [14]aneN_4Cl_2]Cl, [Ni 2-Me[14]aneN_4Cl_2]ClO_4 and [Ni meso-5,12-Me_2[14]ane-N_4Cl_2]Cl·CH_3OH reveal analogies in their magnetic properties. The values of magnetic moment are shown in Table 1. All complexes investigated obey the Curie–Weiss law in the 100–300 K temperature range. The values of C and Θ are shown in Table 1. The magnetic moment is constant in the temperature range of 30–300 K. There is a slight decrease of magnetic moment below 30 K. The paramagnetic dependencies of magnetic moment as a function of temperature are presented in Figs. 1, 2. Relatively lower value of μ_{eff} in [Ni meso-5,7,7,12,14,14-Me_6[14]aneN_4Cl_2]Cl can be related to the presence of impurity of Ni(II) form of the complex.

The EPR spectra show considerably greater values of $g_\perp$ than $g_\parallel$ for [Ni meso-5,12-Me_2[14]aneN_4Cl_2]Cl·CH_3OH and [Ni meso-5,7,7,12,14,14-Me_6[14]aneN_4Cl_2]Cl complexes, as expected of a low-spin, d^7 metal centre in an elongated octahedral environment. Compounds [Ni [14]aneN_4Cl_2]Cl and [Ni 2-Me[14]aneN_4Cl_2]ClO_4 give a rhombic EPR spectrum with g_1, g_2 and g_3 values presented in Table 1. If the first value is taken as $g_\parallel$ and the average of g_2 and g_3 are taken as pseudo-$g_\perp$, these two complexes belong (as well as the previous ones) to the class having $g_\perp > g_\parallel$. The form of the EPR spectra for the low-spin Ni(III) complexes with $g_\perp > g_\parallel$ suggests that the

d_z^2 orbital is favoured for the single unpaired electron. All the compounds investigated have very similar values of $g_\perp$ (as well as of $g_\parallel$) components. There is a slight increase of the $g_\perp$ values observed when the number of methyl groups in the molecule is increased.

Table 1. The magnetic parameters of the compounds investigated

Compound	μ_{eff}*	Θ** (K)	C** ($cm^3 \cdot K \cdot mol^{-1}$)	Spectroscopic splitting parameter*		
				g_1	g_2	g_3
[Ni [14]aneN$_4$Cl$_2$]Cl	1.82	1.9	0.409	2.024	2.105	2.179
[Ni 2-Me[14]aneN$_4$Cl$_2$]ClO$_4$	1.80	1.5	0.406	2.076	2.133	2.180
[Ni meso-5, 12-Me$_2$[14] -aneN$_4$Cl$_2$]Cl · CH$_3$OH	1.83	2.7	0.412	g_{II} = 2.026		$g_\perp$ = 2.182
[Ni meso-5,7,7,12,14,14 -Me$_6$[14]aneN$_4$Cl$_2$]Cl	1.54	5.9	0.293	g_{II} = 2.027		$g_\perp$ = 2.209

*At a room temperature.
**In the temperature range of 50–300 K.

The solid-state reflectance spectra of these complexes consist of two bands at about 28600 and 12300 cm^{-1}. The position of the second band shifts to a lower frequency while the number of the methyl groups in the complex is increased. The EPR data are presented in Table 1.

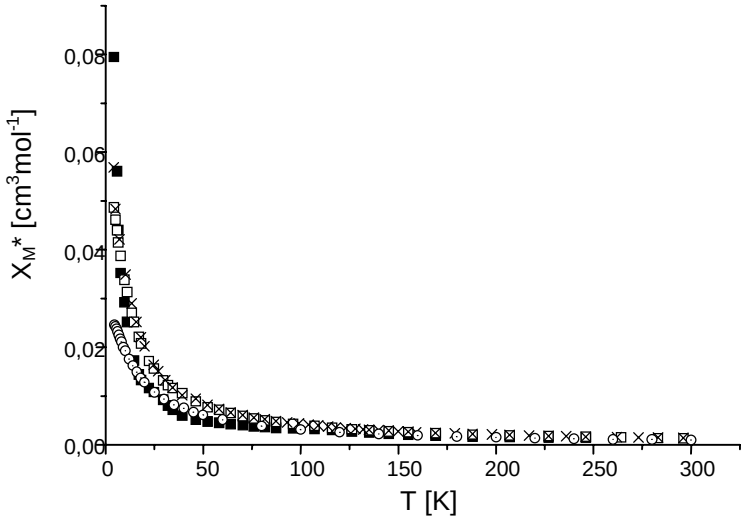

Fig. 1. Experimental magnetic data plotted as a molar magnetic susceptibility χ_M^* vs. temperature for the compound [Ni [14]aneN$_4$Cl$_2$]Cl (■), [Ni 2-Me[14]aneN$_4$Cl$_2$]ClO$_4$ (□), [Ni meso-5,12-Me$_2$[14]aneN$_4$Cl$_2$]Cl·CH$_3$OH (×) and [Ni meso-5,7,7,12,14,14-Me$_6$[14]aneN$_4$Cl$_2$]Cl (○)

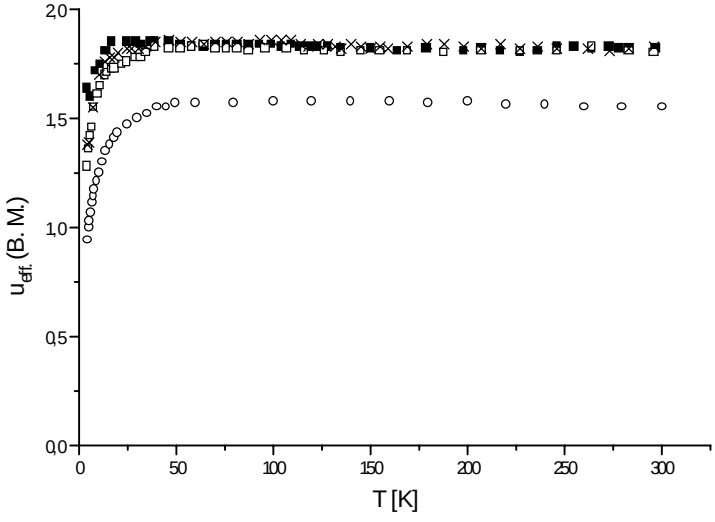

Fig. 2. Experimental magnetic data plotted as a magnetic moment $\mu_{eff.}$ vs. temperature for the compound [Ni [14]aneN_4Cl_2]Cl (■), [Ni 2-Me[14]aneN_4Cl_2]ClO_4 (□), [Ni meso-5,12-Me_2[14]aneN_4Cl_2]Cl·CH_3OH (×) and [Ni meso-5,7,7,12,14,14-Me_6[14]aneN_4Cl_2]Cl (○)

The IR spectra of all complexes show absorption of NH groups (ν_{NH}) between 3198 and 3046 cm^{-1}. One compound of the formula [Ni meso-5,12-Me_2[14]ane-N_4Cl_2]Cl exhibits a ν_{OH} band at 3541 cm^{-1} originating from coordinated methanol molecule.

The study of the magnetic susceptibility data for the complexes [CuL]X_2 (where L= 6,13-Bis(dodecylaminomethylidene)-1,4,8,11-tetrazacyclotetradeca-4,7,11,14-tetraene), Fig. 3) has been performed within the temperature range of 1.90–300 K. The experimental data, plotted as the thermal variations of the $\chi_M T$ product, are shown in Fig. 4 for [CuL]$(Cl_2)\cdot 2H_2O$, [CuL](Br_2), [CuL]$(PF_6)_2$ and [Cu(L-$2H^+$)] complexes.

In all the cases the χ_M value increases slowly with the decrease of temperature, but in the low-temperature region a rapid increase of molar susceptibility values occurs without showing a maximum. The values of $\chi_M T$ for [CuL](Br_2) and [Cu(L-$2H^+$)] complexes decrease very slowly with T in a wide range of temperature. At low temperatures (below 20 K), they decrease to 0.19 $cm^3\cdot mol^{-1}\cdot K$ and to 0.24 $cm^3\cdot mol^{-1}\cdot K$ at 1.90 K, respectively. In the case of [CuL]$(Cl_2)\cdot 2H_2O$ a rapid decrease of $\chi_M T$ values is observed, from 0.75 $cm^3\cdot mol^{-1}\cdot K$ at a room temperature to 0.29 $cm^3\cdot mol^{-1}\cdot K$ at 1.90 K.

For the [CuL]$(PF_6)_2$ complex the $\chi_M T$ values remain nearly constant in a wide range of temperatures and

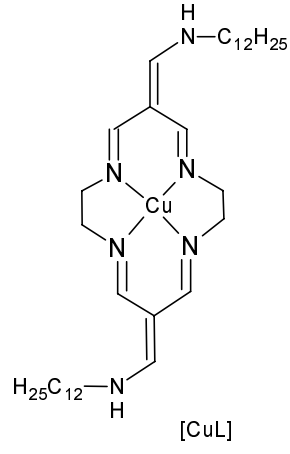

Fig. 3. Schematic view of $[CuL]^{2+}$ cation

below 10 K $\chi_M T$ increases upon cooling. This indicates that some exchange interaction between copper atoms in the crystal lattices of compounds examined can exist. In such situations the exchange parameter zJ' can be determined only by a susceptibility equation with a molecular field correction [15].

$$\chi_M = \frac{g^2 N\beta^2}{3kT} S(S+1) \qquad \chi'_M = \frac{\chi_M}{1-\left(\frac{2zJ'}{Ng^2\beta^2}\right)\chi_M} \tag{1}$$

where N is the Avogadro number, g – the spectroscopic splitting factor, β – the Bohr magneton, k – the Boltzmann constant and zJ'– intermolecular exchange parameter.

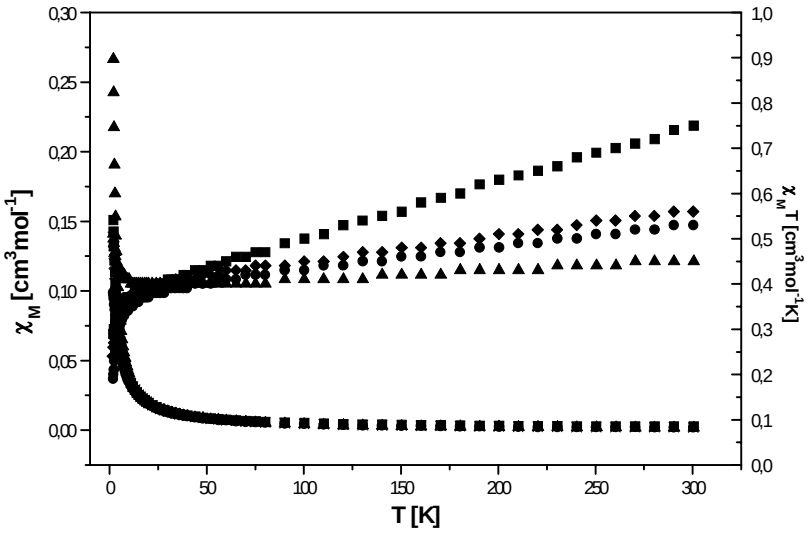

Fig. 4. Thermal dependence of χ_M and $\chi_M T$ for: ■ – $[CuL](Cl_2)\cdot 2H_2O$, • – $[CuL](Br_2)$, ▲ – $[CuL](PF_6)_2$, ◆ – $[Cu(L\text{-}2H^+)]$.

The best fit parameters are g = 2.06 and zJ' = –0.52 cm^{-1} for $[CuL](Cl_2)\cdot 2H_2O$, g = 2.16 and zJ' = –1.53 cm^{-1} for $[CuL](Br_2)$, g = 2,12 and zJ' = –0.84 cm^{-1} $[Cu(L\text{-}2H^+)]$ and g = 2.05 and zJ' = 0.29 cm^{-1} for $[CuL](PF_6)_2$, obtained with good agreement factors $R = 2.30\cdot 10^{-5}$ for $[CuL](Cl_2)\cdot 2H_2O$, $R = 4.57\cdot 10^{-5}$ for $[CuL](Br_2)$ and $R = 8.40\cdot 10^{-5}$ for $[Cu(L\text{-}2H^+)]$ and $R = 1.86\cdot 10^{-5}$ for $[CuL](PF_6)_2$.

The EPR spectra of the compound examined at a room temperature and 77 K present only single lines of $H = 3500g$ for ν = 9.771 Ghz. The spectroscopic splitting factor was typical of copper(II) centres, g amounting to 2.08 for all compounds. In principle, the observed weak antiferromagnetic interactions in $[CuL](Cl_2)\cdot 2H_2O$, $[CuL](Br_2)$ and $[Cu(L\text{-}2H^+)]$ complexes and weak ferromagnetic interactions in $[CuL](PF_6)_2$ could be attributed to intermolecular interactions between copper centres,

which may be transmitted through Cl^-, Br^-, PF_6^- anions or H^+ cations in a crystal lacttice.

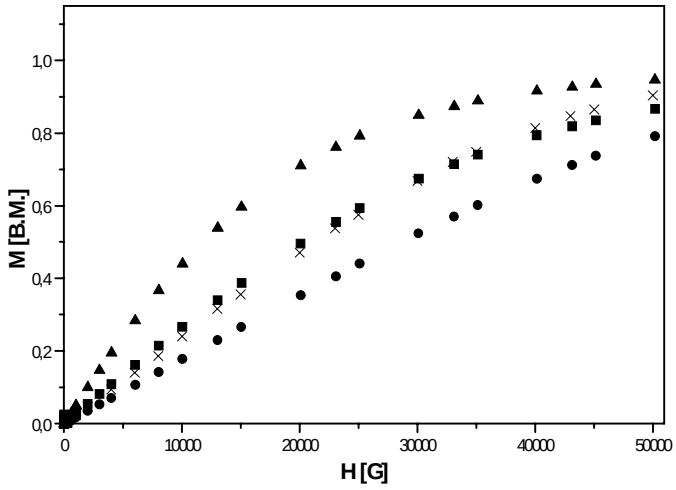

Fig. 5. Field dependence of the magnetization at 1.9 K for the complexes:
■ – $[CuL](Cl_2)\cdot 2H_2O$, • – $[CuL](Br_2)$, ▲ – $[CuL](PF_6)_2$, × – $[Cu(L\text{-}2H^+)]$

The field dependence of magnetization for all complexes at 1.9 K (Fig. 5) clearly supports the occurrence of very weak interactions in all complexes. In consequence, one can say that the communication between copper(II) centres in crystal lacttice is higher in the case of $[CuL](Br_2)$ than in $[CuL](Cl_2)\cdot 2H_2O$ and $[Cu(L\text{-}2H^+)]$ complexes and have an opposite character than that in the $[CuL](PF_6)_2$ compound.

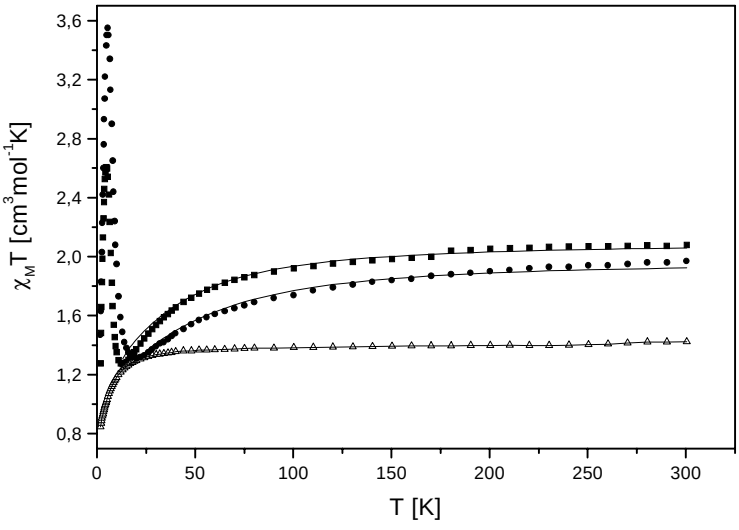

Fig. 6. Temperature dependencies of $\chi_M T$ for: ■ – $[CuL]ReCl_6\cdot H_2O$, • – $[CuL]ReBr_6$, Δ – $[Bu_4N]_2ReCl_6$; the solid lines are the calculated curves

The magnetic properties of complexes $[CuL]ReCl_6 \cdot H_2O$ and $[CuL]ReBr_6$ as the plot of $\chi_M T$ vs. T (χ_M being the molar magnetic susceptibility per $Re^{IV}Cu^{II}$ heterobinuclear unit) are shown in Fig. 6 and the $\chi_M T$ data of $(Bu_4N)_2ReCl_6$ are also included for comparison.

At a room temperature $\chi_M T$ for heterometallic compounds are equal to 2.08 $cm^3 \cdot K \cdot mol^{-1}$ and 1.97 $cm^3 \cdot K \cdot mol^{-1}$ for $[CuL]ReCl_6 \cdot H_2O$ and $[CuL]ReBr_6$, respectively. These values are close to the expected one for uncoupled Re^{IV}–Cu^{II} ions. As the temperature is lowered, the $\chi_M T$ smoothly decrease and reach rounded minima at 13.0 K with $\chi_M T$ =1.27 $cm^3 \cdot K \cdot mol^{-1}$ and at 20 K with 1.31 $cm^3 \cdot K \cdot mol^{-1}$ for $[CuL]ReCl_6 \cdot H_2O$ and $[CuL]ReBr_6$, respectively. The presence of a minimum in the $\chi_M T$ curve is indicative of antiferromagnetic coupling between Re^{IV} and Cu^{II} and is characteristic of one-dimensional ferrimagnetic chain compounds [16]. Below the temperatures: 13.0 K for $[CuL]ReCl_6 \cdot H_2O$ and 20 K for $[CuL]ReBr_6$, the values of $\chi_M T$ for both compounds increase, then reach maxima at 4.73 K with $\chi_M T$ = 2.61 $cm^3 \cdot K \cdot mol^{-1}$ for $[CuL]ReCl_6 \cdot H_2O$ and 5.49 K with $\chi_M T$ = 3.55 $cm^3 \cdot K \cdot mol^{-1}$ for $[CuL]ReBr_6$ compound and finally decrease rapidly below 4.73 for $[CuL]ReCl_6 \cdot H_2O$ and 5.49 K for $[CuL]ReBr_6$, respectively (Fig. 6).

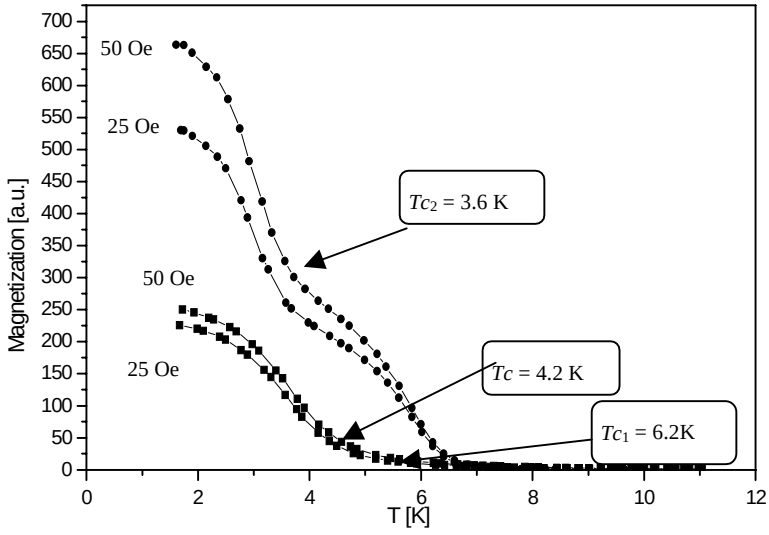

Fig. 7. *M*. versus *T* plots in the low-temperature range for two different values of the applied magnetic field for: ■ – $[CuL]ReCl_6 \cdot H_2O$, • – $[CuL]ReBr_6$

The variation of susceptibility with temperature for these compounds could be satisfactorily fitted using the spin Hamiltonian defined by Eq. (2) [17–19]:

$$H = \sum_i \left\{ \begin{array}{l} -JS^z_{2i-1}S^z_{2i} + g_{\mathrm{II}Cu}\beta S^z_{2i-1}H_z + g_{\mathrm{II}\,\mathrm{Re}}\beta S^z_{2i}H_z + \\ g_{\perp Cu}\beta\left(S^x_{2i-1}H_x + S^y_{2i-1}H_y\right) + g_{\perp \mathrm{Re}}\beta\left(S^x_{2i}H_x + S^y_{2i}H_y\right) + D\left[\left(S^z_{2i}\right)^2 - \frac{5}{4}\right] \end{array} \right\} \quad (2)$$

The least-squares fitting of the experimental data with this expression was limited to the range of 13–300 K for [CuL]$ReCl_6 \cdot H_2O$ and 20–300 K for [CuL]$ReBr_6$ yielding D = 53.4 cm^{-1}, g_{IIRe} =1.94 and $g_{\perp Re}$=1.90, g_{IICu} =2.29, $g_{\perp Cu}$=1.93 and J = –9.1 cm^{-1} for [CuL]$ReCl_6 \cdot H_2O$ and D = 63.6 cm^{-1}, g_{IIRe} =1.84 and $g_{\perp Re}$=1.82, g_{IICu} =2.29 $g_{\perp Cu}$=1.99 and J = –12.2 cm^{-1} for [CuL]$ReBr_6$. We conclude that Re^{IV} in [CuL]$ReCl_6 \cdot H_2O$ and [CuL]$ReBr_6$ exhibits a large zero-field splitting parameter together with weak antiferromagnetic interactions with Cu^{II}.

The magnetization vs. temperature curves (Fig. 7) reveal magnetic transitions at Tc = 4.2 K for [CuL]$ReCl_6 \cdot H_2O$ as well as at Tc_1 = 6.2 K and Tc_2 = 3.6 K for [CuL]$ReBr_6$. [CuL]$ReCl_6 \cdot H_2O$ and [CuL]$ReBr_6$ are ferrimagnetic chains as a result of ordering [19]. The occurrence of the second Curie temperature (Tc_2 = 3.6 K) in the [CuL]$ReBr_6$ complex does not follow the phenomenon of the compensation temperature in ferrimagnets. Probably, there are two different kinds of sublattices in [CuL]$ReBr_6$, both of ferromagnetic character.

Acknowledgements

This work was financially supported by the Polish State Committee for Scientific Research, Grant No. 4 T09A 115 23.

References

[1] OHBA M., OKAWA H., Coord. Chem. Rev., 198 (2000), 313.
[2] (a) FRANCESE G., FERLAY S., SCHMALLE H.W., DECURTINS S., New J. Chem. (1999), 267;
(b) SKORUPA A., KORYBUT-DASZKIEWICZ B., MROZIŃSKI J., Inorg. Chim. Acta, 324 (2001), 286;
(c) SKORUPA A., KORYBUT-DASZKIEWICZ B., MROZIŃSKI J., Inorg. Chim. Acta, 336 (2002), 65;
[3] (a) FERLAY S., MALLAH T., VAISSERMANN J., BARTOLOME F., VEILLET P., VERDAGUER M., Chem. Commun. (1996), 2481;
(b) ZOU J., HU X., DUAN CH., XU Z., YOU X., Transition Met. Chem., 23 (1998), 477;
(c) COLACIO E., DOMINGUEZ-VERA J.M., GHAZI M., KIVEKÄS R., KLINGA M., MORENO J.M., Chem. Commun., 10 (1998), 1071;
(d) COLACIO E., DOMINGUEZ-VERA J.M., GHAZI M., KIVEKÄS R., LLORET F., MORENO J.M., STOECKLI-EVANS H., Chem. Commun., 11 (1999), 987;
(e) KOU H.Z., GAO S., BU W.M., LIAO D.Z., MA B.Q., JIANG Z.H., YAN S.P., FAN Y.G., WANG G.L., J. Chem. Soc. Dalton Trans. (1999), 2477;
(f) KOU H.Z., GAO S., MA B.Q., LIAO D.Z., Chem. Commun. (2000), 713.
(g) COLACIO E., DOMINGUEZ-VERA J.M., GHAZI M., KIVEKÄS R., MORENO J.M., PAJUNEN A, J. Chem. Soc., Dalton Trans. (2000), 505;
[4] MELSON G.A., *Coordination Chemistry of Macrocyclic Compounds*, Plenum Press, New York, 1979.
[5] *The Bioinorganic Chemistry of Nickel*, Lancaster J.R. Jr. (Ed.), VCH Publishers, New York, 1988.
[6] MULLER J. ., CHEN X., DIAZ A. C., ROKITA S.E., BURROWS C.J., Pure Appl. Chem., 65 (1993), 545.
[7] KINEARY J.F., WAGLER T.R. BURROWS C.J., Tetrahedron Lett., 29 (1988), 877.
[8] ROSŁONEK G., TARASZEWSKA J., J. Electroanal. Chem., 325 (1992), 285.
[9] ITO T., SUGIMOTO M., TORIUMI K. ITO H., Chem. Lett. (1981), 1477.
[10] BANAŚ B., NAHORSKA M., KORYBUT-DASZKIEWICZB., MROZIŃSKI J., Polish J. Chem., 77 (2003), 21.
[11] KORYBUT-DASZKIEWICZ B., WIĘCKOWSKA A., BILEWICZ R., DOMAGAŁA S., WOŹNIAK K., J. Am. Chem. Soc., 123 (2001), 9356.

[12] TANASE S., ANDRUH M., MŰLLER A., SCHMIDTMANN M., MATHONIÈRE C., ROMBAUT G., Chem. Commun. (2001), 1084.
[13] TARASZEWSKA J., SADŁO J., MICHALIK J., KORYBUT-DASZKIEWICZ B., Polish J. Chem., 74 (2000), 813.
[14] KÖNIG, *Magnetic Properties of Coordination and Organometallic Transition Metal Compounds*, Springer-Verlag, Berlin, 1966.
[15] TOMKIEWICZ A., ZYGMUNT A., MROZIŃSKI J., J. Mol. Struct., 644 (2002), 97.
[16] CORONADO E., DRILLON M., NUGTEREN P.R., DE JONGH L.J., BELTRÁN D., J. Am. Chem. Soc., 110 (1988), 3907.
[17] TOMKIEWICZ A., VILLAIN F., MROZIŃSKI J., J. Mol. Struct., 555 (2000), 383.
[18] CHIOZZONE R., GONZÁLEZ R., KREMER C., DE MUNNO G., CANO J., LLORET F., JULVE M., FAUS J., Inorg. Chem., 38 (1999), 4745.
[19] STUMPF H.O., PEI Y., OUAHAB L., LE BERRE F., CODJOVI E., KAHN O., Inorg. Chem., 32 (1993), 5687.

Received 24 March 2003
Revised 23 May 2003

Materials Science, Vol. 21, No. 2, 2003

Thiolato-bridged copper complexes with N,N,S-tridentate ligands*

TAKANORI KOTERA[1], ATSUSHI FUJITA[1], MASAHIRO MIKURIYA[1**], MAKOTO HANDA[2]

[1]Department of Chemistry, School of Science and Technology,
Kwansei Gakuin University, 2-1 Gakuen, Sanda 669-1337, Japan

[2]Department of Material Science, Interdisciplinary Faculty of Science and Engineering,
Shimane University, 1060 Nishikawatsu, Matsue 690-8504, Japan

Thiolato-bridged complexes $[Cu^{II}_2(apaet)Cl_3]$ and $[Cu^{I}_3Cu^{II}_3(apampt)_3Cl_6]$ (Hapaet = 2-[(3-aminopropyl)amino]ethanethiol, Hapampt = 1-[(3-aminopropyl)amino]-2-methylpropane-2-thiol), have been synthesized and characterized by infrared and electronic absorption spectra and temperature dependence of magnetic susceptibilities. X-ray crystallography of the latter complex reveals a localized mixed-valence structure which is supported by the spectroscopic and electrochemical data. Magnetic susceptibility data show that a strong antiferromagnetic interaction is operating between Cu^{II} ions in both complexes.

Key words: *thiolato-bridged complexes; mixed-valence complexes; Cu; hexanuclear complexes*

1. Introduction

Study on mixed-valent complexes are of interest because of their potential application in the development of functional materials showing efficient long-distance electron transfer in the field of molecular electronics (cf. [1]) and their biological relevance involving multicopper oxidases such as spin-delocalized dinuclear mixed-valent copper cluster found in the 'Cu_A' site of cytochrome *c* oxidase and nitrous oxide reductase [2]. Especially thiolato-bridged mixed-valent copper complexes have been focused from the view of model complexes for the latter systems. So far, many attempts to synthesize thiolato-bridged dinuclear Cu^{II}_2 and $Cu^{I}Cu^{II}$ complexes have been unsuccessful, because thiols usuallly reduce copper(II) to copper(I)

---

* The paper was presented at the 13th Winter School on Coordination Chemistry, Karpacz, Poland, 9–13 December, 2002.

** Corresponding author, e-mail: junpei@ksc.kwansei.ac.jp.

$$2RS^- + 2Cu^{II} \leftrightarrow RSSR + 2Cu^{I}$$

Moreover, the electron-rich thiolato groups have a great affinity for various metal ions to form undesirable polymeric species with low solubilities hampering their precise characterization. In this regard, thiolic ligands having nitrogen donor atoms are useful, because formation of discrete thiolato-bridged complexes can be expected to be feasible by virtue of the chelating effect. In fact, dinuclear metal species were isolated for nickel(II) [3–9], cobalt(III) [10], and iron(II) [11] ions. Linear and cyclic trinuclear metal species [12], tetrahedral [13, 14] and adamantane-like [15] tetranuclear species, chain-like polynuclear species [12, 16, 17] were also obtained. For N,N,S tridentate ligands such as 2-[(3-aminopropyl)amino]ethanethiol (Hapaet), linear trinuclear metal species consisting of octahedral-tetrahedral-octahedral coordination environments seems to be most favourable structural pattern and we obtained such species in the cases of Zn^{II} [12], Cd^{II} [18], Mn^{II} [17], Fe^{II} [11], Co^{II} [19], and Ni^{II} [20] including trinuclear heterometal complexes [20] which are formed by one-pot reaction. In this study, we introduced a new thiolic ligand, 1-[(3-aminopropyl)amino]-2-methylpropane-2-thiol (Hapampt) as well as Hapaet, as chelating agents in the hope of attaining to make mixed-valence species by using the thiolic ligands. A preliminary account of this work has been published [21].

2. Experimental

Syntheses were carried out by using standard Schlenk techniques under argon. The thiolic ligand Hapaet was synthesized using a procedure described in the literature [4]. The Hapampt ligand was synthesized as follows. A toluene solution (50 cm^3) of isobutylene sulfide (8.6 g, 0.098 mol) was added dropwise to a toluene solution (200 cm^3) containing 1,3-diaminopropane (74.1 g, 1.00 mol). The solution was refluxed for 2 h. Then, the solvent was removed by distillation and the product was fractionally distilled at reduced pressure. Yield: 10.4 g (65.7%). bp. 79–81°C /5 mmHg. IR (KBr, cm^{-1}): $\nu_{as}(NH_2)$ 3350, $\nu_s(NH_2)$ 3300, $\nu(CH_3)$ 2960, $\nu(CH_2)$ 2860, $\delta(NH_2)$ 1575.

$[Cu_2(apaet)Cl_3]$ (1). To a solution of Hapaet (26 mg, 0.2 mmol) in methanol (2 cm^3) was added a solution of copper(II) chloride dihydrate (34 mg, 0.2 mmol) in methanol (3 cm^3). The reaction mixture was stirred at room temperature for 5 min and filtered. The resulting purple filtrate was allowed to stand several days at 7 °C. Dark purple precipitate deposited was collected by filtration. Yield 22 mg (30%). Found: C, 16.21; H, 3.59; N, 7.22%. Calcd for $C_5H_{13}Cl_3Cu_2N_2S$: C, 16.38; H, 3.57; N, 7.64%. IR (KBr, cm^{-1}): $\nu_{as}(NH_2)$ 3450, $\nu_s(NH_2)$ 3220, $\nu(CH_3)$ 2930, $\nu(CH_2)$ 2880, $\delta(NH_2)$ 1585.

$[Cu_6(apampt)_3Cl_6]\cdot 2H_2O$ ($2\cdot 2H_2O$). To a solution of Hapampt (32 mg, 0.2 mmol) in methanol (5 cm^3) was added a solution of copper(II) chloride dihydrate (34 mg, 0.2 mmol) in methanol (5 cm^3). The solution was stirred at room temperature for 5 min and filtered.

The resulting light brown filtrate was placed at 7 °C for several days to give dark brown crystals. Yield, 27 mg (74% based on the metal source). Found: C, 22.56; H, 4.77; N, 7.41%. Calcd for $C_{21}H_{55}Cl_6Cu_6N_6O_2S_3$ C, 22.64; H, 4.98; N, 7.54%. IR (KBr, cm^{-1}): $\nu_{as}(NH_2)$ 3420, $\nu_s(NH_2)$ 3285, $\nu(CH_3)$ 2950, $\nu(CH_2)$ 2830, $\delta(NH_2)$ 1590.

Measurements. Elemental analyses for carbon, hydrogen, and nitrogen were done using a Perkin-Elmer 2400 Series II CHNS/O Analyzer. Infrared spectra were measured with a JASCO MFT-2000 FT-IR Spectrometer in the 4000–600 cm^{-1} region. The electronic spectra were measured with a Shimadzu UV-vis-NIR Recording Spectrophotometer (Model UV-3100). The temperature dependence of the magnetic susceptibilities was measured with a Quantum Design MPMS-5S SQUID susceptometer operating at a magnetic field of 0.5 T between 4.5 and 300 K. The susceptibilities were corrected for the diamagnetism of the constituent atoms using Pascal's constants [22]. The effective magnetic moments were calculated from the equation $\mu_{eff} = 2.828\sqrt{\chi_A T}$, where χ_A is the atomic magnetic susceptibility. Cyclic voltammetric measurements were carried out on a BAS 100 BW Electrochemical Work Station. A three-electrode cell consisting of a glassy carbon electrode, a platinum-wire counter electrode, and a Ag/AgCl electrode was used.

X-ray crystal structure analysis. Crystals suitable for X-ray diffraction work were obtained as **2**·2CH_3OH from a methanol solution. A black crystal of **2**·2CH_3OH was mounted on a glass fibre with epoxy cement at a room temperature. A preliminary examination was made and data were collected on a Bruker CCD X-ray diffractometer (SMART APEX) using graphite-monochromated Mo K_α radiation. The structure was solved by direct methods and refined by full-matrix least-squares. All non-hydrogen atoms were refined with anisotropic thermal parameters. The hydrogen atoms were inserted at their calculated positions and fixed there. All calculations were carried out on a Pentium III Windows NT computer utilizing the SHELXTL software package.

Crystallographic data for **2**·2CH_3OH; $C_{23}H_{59}Cl_6Cu_6N_6O_2S_3$ *F.W.* = 1141.88, orthorhombic, space group *Pbca*, *a* = 18.706(5), *b* = 18.283(5), *c* = 23.962(6) Å, *V* = 8195(4) $Å^3$, *Z* = 8, D_c = 1.85 g·cm^{-3}, μ(Mo K_α) = 36.34 cm^{-1}, F(000) = 4568, crystal size 0.40 × 0.20 × 0.10 mm^3, 33826 reflections collected, 5936 independent reflections, $R1[I>2\sigma(I)] = 0.048$, $wR2\ [I>2\sigma(I)] = 0.110$.

3. Results and discussion

In the previous papers, we reported that reaction of Hapaet ligand with metal ions affords dinuclear nickel(II) complex $[Ni_2(apaet)_2]X_2$ ($X = ClO_4^-, BF_4^-$) [4], linear trinuclear complexes $[M\{M(apaet)_2\}_2]X_2$ (M = Mn [17], Fe [11], Co [19], Cd [18], $X = Cl^-$, ClO_4^-), $[M\{M'(apaet)_2\}_2](ClO_4)_2$ (M = Zn, Cd, Hg; M' = Mn, Fe, Co, Ni) [20], and tetrahedral tetranuclear palladium(II) complex $[Pd_4(apaet)_4]Cl_4$ [14]. In the present case, the reaction of Hapaet with copper(II) gave a different species. Elemen-

tal analysis of the isolated complex shows a stoichiometry Cu : apaet$^-$ = 2:1, which is consistent with the formulae for a copper(II) species $[Cu_2(apaet)Cl_3]$ (**1**). On the other hand, the reaction of the methylated thiol, Hapampt, with copper(II) afforded a mixed-valent species, $[Cu_6(apampt)_3Cl_6]\cdot 2H_2O$ (**2**$\cdot 2H_2O$). In the infrared spectrum of **1**, the absorption bands due to apaet$^-$ ligand appear as a set of distinctive bands in a similar wavenumber region to that of the free thiol, Hapaet, with lacking the ν(SH) band (Fig. 1). The infrared spectrum of **2**$\cdot 2H_2O$ is essentially the same as that of **1** except for the bands due to the methyl groups.

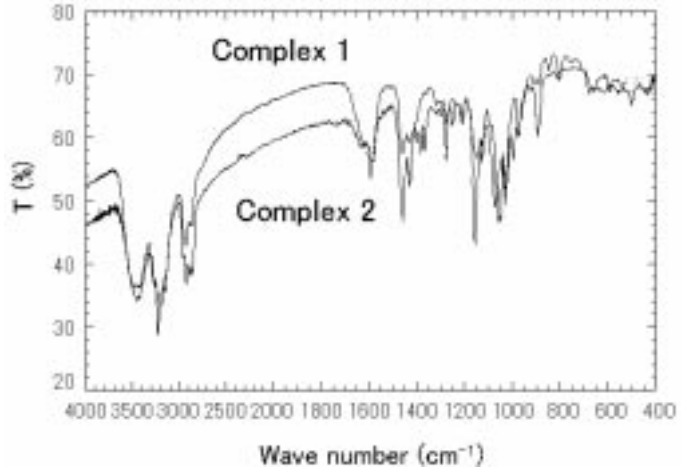

Fig. 1. Infrared spectra of $[Cu_2(apaet)Cl_3]$ (**1**) and $[Cu_6(apampt)_3Cl_6]\cdot 2H_2O$ (**2**$\cdot 2H_2O$)

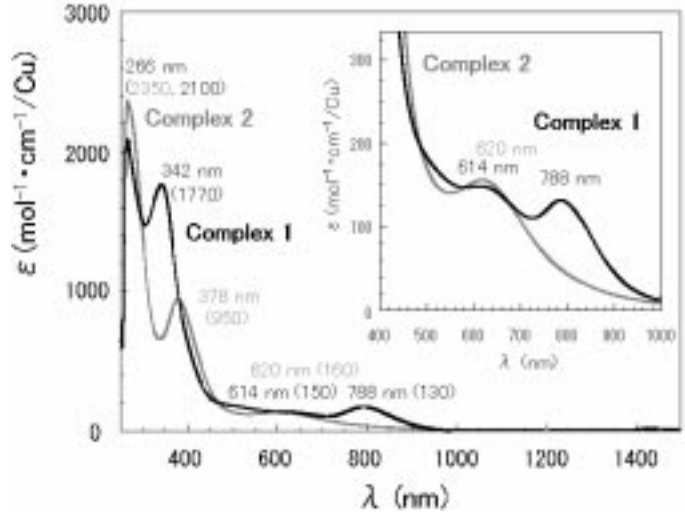

Fig. 2. Electronic absorption spectra of $[Cu_2(apaet)Cl_3]$ (**1**) and $[Cu_6(apampt)_3Cl_6]\cdot 2H_2O$ (**2**$\cdot 2H_2O$) in DMF

The electronic absorption spectra in DMF are shown in Fig. 2. The bands at the visible region (**1**: 614 and 788 nm, **2**·2H_2O: 620 nm) may be assigned to d–d transitions judging from the intensities of the absorption bands. The band at the near-ultraviolet region (**1**: 342 nm, **2**·2H_2O: 378 nm) should correspond to the σ(S)→d(Cu) LMCT [23]. The absorption at the ultraviolet region (266 nm) may be assigned to the σ(Cl)→d(Cu) LMCT band [24]. We could not observe any IT band in the present complexes and thus the mixed-valence state of **2**·2H_2O seems to be fully localized.

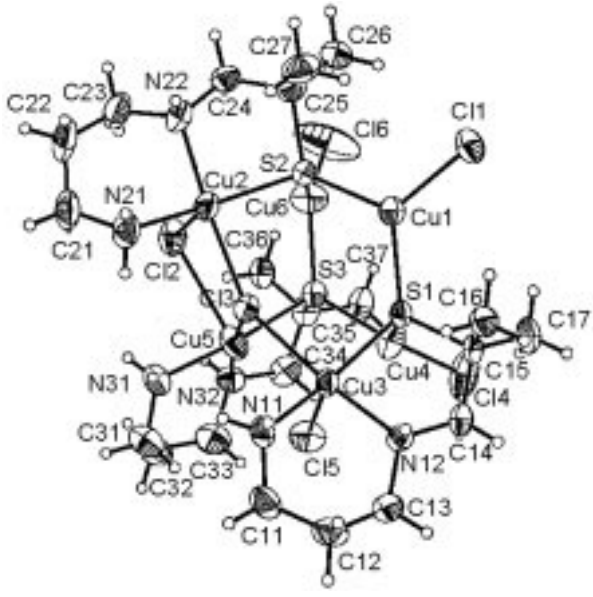

Fig. 3. ORTEP drawing of the structure of $[Cu_6(apampt)_3Cl_6]\cdot 2CH_3OH$ (**2**·2CH_3OH) showing the 50% probability thermal ellipsoids and atom labelling scheme. Methanol molecules are omitted for clarity

The X-ray crystal structural analysis of **2**·2CH_3OH reveals a unique hexanuclear structure that is distinctly different from those of any previously structurally characterized thiolato complexes with N,N,S-tridentate ligands (Fig. 3) [4–20]. Selected bonding parameters are listed in the table. The hexanuclear core is shown in Fig. 4. Based on the charge consideration and the different coordination environments around the copper atoms, we can assign the Cu1, Cu4, and Cu6 atoms to copper(I) and the Cu2, Cu3, and Cu5 atoms to copper(II), respectively. The Cu^I–Cu^I, Cu^{II}–Cu^{II}, and Cu^I–Cu^{II} distances are 3.521(2)–3.777(2), 3.850(1)–4.625(1), and 3.375(1)–5.420(2) Å, respectively. The Cu^I atoms form a chair-like six-membered [–Cu1–S1–Cu4–S3–Cu6–S2–] ring with thiolato-sulfur atoms of $apampt^-$, whereas the Cu^{II} atoms form two adjacent planar four-membered rings [–Cu2–Cl3–Cu5–Cl2–] and [–Cu3–Cl5–Cu5–Cl3–] with chloride ions. The coordination geometries of the Cu^I atoms are trigonal with two thiolato-sulfur atoms of $apampt^-$ and chloride ion. The Cu^I–S bond distances [2.225(2)–2.259(2) Å] are within the normal range found in Cu^I complexes

[25]. The Cu^{I}–Cl distances [2.216(3)–2.238(2) Å] are in the normal range of the Cu^{I}–Cl distances [25]. On the other hand, there are two kinds of coordination geometries for the Cu^{II} atoms. The Cu2 and Cu3 atoms take an elongated square-pyramidal geometry with two amino-nitrogen atoms and thiolato-sulfur atom of apampt^{-} (N21, N22, S2 for Cu2; N11, N12, S1 for Cu3) and chloride ion (Cl3) in the equatorial plane and a chloride ion (Cl2 for Cu2; Cl5 for Cu3) at the apex, while the Cu5 atom has a distorted octahedral geometry with two amino-nitrogen atoms and thiolato-sulfur atom of apampt^{-} (N31, N32, S3) and three chloride ions (Cl2, Cl3, Cl5). The Cu^{II}–S distances [2.225(2)–2.273(2) Å] are comparable to the values found in thiolato-bridged $Cu^{I}Cu^{II}$ mixed-valent complexes [26, 27], although these distances are similar to those of the Cu^{I}–S bonds. The Cu^{II}–Cl distances (2.370(2)–2.607(2) Å for the square-pyramidal Cu atoms; 2.696(2)–2.839(2) Å for the octahedral Cu atom) are in the normal range for the Cu^{II}–Cl distances [25].

Table. Selected bond distances (Å) and angles (°) with their estimated standard deviations in parentheses $\left[Cu^{I}_{3}Cu^{II}_{3}(apampt)_{3}Cl_{6}\right]\cdot 2CH_{3}OH$ (**2**$\cdot 2CH_{3}OH$)

Cul–Cu2	3.958(1)	Cu4–Cu6	3.777(2)	Cu3–C13	2.396(2)
Cul–Cu3	3.925(1)	Cu5–Cu6	3.730(2)	Cu3–C15	2.557(2)
Cul–Cu4	3.722(1)	Cul–S1	2.226(2)	Cu4–S1	2259(2)
Cul–Cu5	5.229(2)	Cul–S2	2.225(2)	Cu4–S3	2.237(2)
Cul–Cu6	3.521(2)	Cul–Cll	2226(2)	Cu4–C14	2.238(2)
Cu2–Cu3	4.625(1)	Cu2–S2	2.273(2)	Cu5–S3	2.253(2)
Cu2–Cu4	5.420(2)	Cu2–N21	2.005(6)	Cu5–N31	1.979(5)
Cu2–Cu5	3.850(1)	Cu2–N22	2.019(6)	Cu5–N32	2.051(5)
Cu2–Cu6	3.506(2)	Cu2–C12	2.607(2)	Cu5–C12	2.762(2)
Cu3–Cu4	3.375(1)	Cu2–C13	2.370(2)	Cu5–C13	2.696(2)
Cu3–Cu5	3.872(2)	Cu3–S1	2.271(2)	Cu5–C15	2.839(2)
Cu3–Cu6	5.396(2)	Cu3–N11	1.990(5)	Cu6–S2	2.230(2)
Cu4–Cu5	3.547(2)	Cu3–N12	2.022(5)	Cu6–S3	2.232(2)
				Cu6–Cl6	2.216(3)
S1–Cul–S2	114.89(7)	SI–Cu3–C13	89.77(7)	S3–Cu5–Cli	92.98(6)
S1–Cul–Cll	124.60(8)	Sl–Cu3–C15	98.77(7)	S3–Cu5–C15	89.99(7)
S2–Cul–Cll	120.14(8)	N11–Cu3–N12	90.4(2)	N31–Cu5–N32	92.4(2)
S2–Cu2–N21	163.1(2)	N11–Cu3–C13	89.5(2)	N31–Cu5–C12	86.3(2)
S2–Cu2–N22	87.6(2)	N11–Cu3–C15	97.1(2)	N31–Cu5–C13	86.5(2)
S2–Cu2–C12	99.94(7)	N12–Cu3–C13	170.5(2)	N31–Cu5–C15	94.7(2)
S2–Cu2–C13	89.58(7)	N12–Cu3–C15	99.8(2)	N32–Cu5–C12	110.6(2)
N21–Cu2–N22	90.6(2)	C13–Cu3–C15	89.68(7)	N32–Cu5–Cl3	169.9(2)
N21–Cu2–Cl2	97.0(2)	S1–Cu4–S3	109.48(7)	N32–Cu5–C15	91.9(2)
N21–Cu2–C13	90.0(2)	S1–Cu4–C14	123.83(8)	Cl2–Cu5–C13	79.38(6)
N22–Cu2–Cl2	98.8(2)	S3–Cu4–C14	122.43(8)	C12–Cu5–C15	157.49(7)
N22–Cu2–Cl3	1723(2)	S3–Cu5–N31	175.1(2)	Cli–Cu5–C15	78.24(6)1
S1–Cu3–N11	164.1(2)	S3–Cu5–N32	89.0(2)	S2–Cu6–C16	127.6(1)
S1–Cu3–N12	87.7(2)	S3–Cu5–Cl2	88.73(7)	S3–Cu6–C16	119.5(1)
				S2–Cu6–S3	111.51(7)

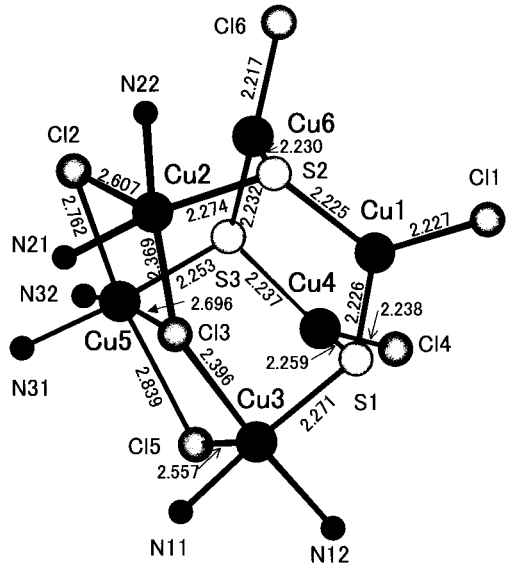

Fig. 4. Core structure of $[Cu_6(apampt)_3Cl_6]\cdot 2CH_3OH$ (**2**·$2CH_3OH$)

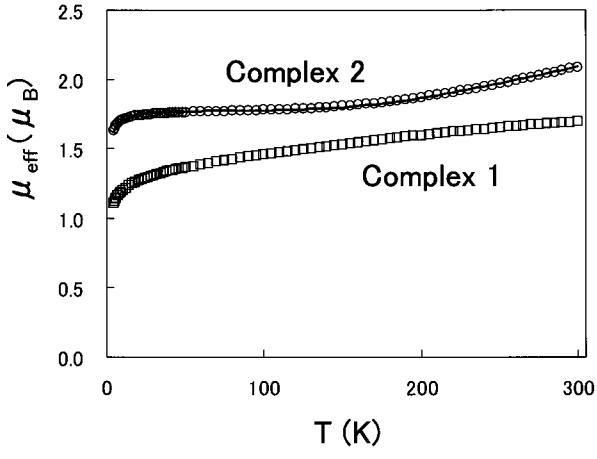

Fig. 5. Temperature dependence of the magnetic moments of $[Cu_2(apaet)Cl_3]$ (**1**) and $[Cu_6(apampt)_3Cl_6]\cdot 2H_2O$ (**2**·$2H_2O$)

The magnetic moments of **1** and **2**·$2H_2O$ are 1.70 μ_B per $[Cu_2(aaet)Cl_3]$ unit and 2.10 μ_B per $[Cu_6(apampt)_3Cl_6]\cdot 2H_2O$, which are lower than the spin-only values, 2.45 and 3.00μ_B, respectively. Temperature dependence of magnetic moments is displayed for **1** and **2**·$2H_2O$ in Fig. 5. The magnetic moments are both decreased with lowering the temperature. The temperature dependence of **1** could not be interpreted by the Bleaney–Bowers equation based on the dinuclear copper(II) structure. Therefore, the structure of **1** may be considered to be polymeric one as one of the possible structures

[28]. On the other hand, the temperature-dependent profile of **2**·2H_2O is fully explained by the van Vleck equation based on the Heisenberg model $H = -2JS_{Cu2}S_{Cu3} - 2J'(S_{Cu2}S_{Cu5}+S_{Cu3}S_{Cu5})$ (see Fig. 4). The parameters obtained by the simulation are as follows: $J = -602$ cm^{-1}, $J' = -2.5$ cm^{-1}, $g = 2.06$, $\theta = -0.91$ K. The present results suggest that a strong antiferromagnetic interaction is mainly operating between the Cu2 and Cu3 atoms. In relation to this, it is to be noted that the bond distances of Cu2–Cl3 [2.370(2) Å] and Cu3–Cl3 [2.396(2) Å] are significantly shorter that those of Cu2 –Cl2, Cu5–Cl2, Cu5–Cl3, Cu5–Cl5, and Cu3–Cl5 [2.557(2)–2.839(2) Å] and the Cu2–Cl3–Cu3 angle [152.07(9)°] is large, which is a favourable feature for the strong antiferromagnetic interaction via the bridging Cl atom [29].

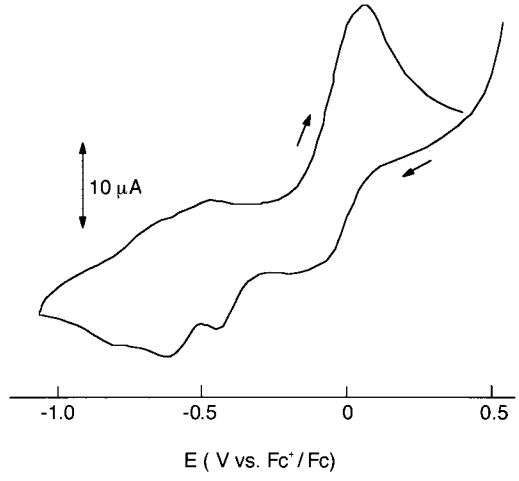

Fig. 6. Cyclic voltammogram of [Cu_6(apampt)$_3Cl_6$]·2H_2O (**2**·2H_2O) in DMF 0.5×10^{-3} M; electrolyte: 0.1 M tetra-*n*-butylammonium perchlorate

In order to examine the mixed-valence state, the cyclic voltammetric measurement was performed for **2**·2H_2O (Fig. 6). In the +0.5 to –1.0 V versus Fc^+/Fc region, three reduction waves are observed at around –0.1, –0.45, and –0.62 V. The first wave seems to be coupled with an anodic wave at +0.06 V. This redox wave may be due to Cu(II)/Cu(I) couple of the Cu^IS_2Cl moiety. The second and third reduction waves have not clear coupled-oxidation waves. These waves may correspond to reduction of $Cu^{II} \rightarrow Cu^I$ of the $Cu^{II}N_2SCl_2$ and $Cu^{II}N_2SCl_3$ moieties.

4. Conclusions

N,N,S-donor tridentate thiols, 2-[(3-aminopropyl)amino]ethanethiol (Hapaet) and 1-[(3-aminopropyl)amino]-2-methylpropane-2-thiol (Hapampt) were synthesized and proved to be useful ligands for the synthesis of thiolato-bridged copper(II) and copper(I, II) mixed-valent complexes. Spectroscopic and electrochemical data as well as

structural feature support a localized mixed-valence state of the thiolato-bridged copper complex with apampt$^-$. Steric hindrance of the methyl groups of apampt$^-$ may contribute to the stabilization of the mixed-valent state by protecting against the oxidation.

References

[1] CARTER F.L., *Molecular Electronic Devices*, Vol. II, Marcel Dekker, New York, 1987.
[2] MICHEL H., BEHR J., HARRENGA A., KANNT A., Ann. Rev. Biophys. Biomol. Struct., 27 (1998), 329.
[3] MIKURIYA M., KIDA S., MURASE I., Bull. Chem. Soc. Jpn., 60 (1987), 1180.
[4] HANDA M., MIKURIYA M., ZHONG Z.J., OKAWA H., KIDA S., Bull. Chem. Soc. Jpn., 61 (1988), 3883.
[5] MIKURIYA M., SHIGEMATSU S., HANDA M., KOHZUMA T., Transition Met. Chem., 16 (1991), 532.
[6] HANDA M., MIKURIYA M., OKAWA H., KIDA S., Chem. Lett. (1988), 1555.
[7] MIKURIYA M., HANDA M., SHIGEMATSU S., FUNAKI S., FUJII T., OKAWA H., TORIUMI K., KOSHIBA T., TERAUCHI H., Bull. Chem. Soc. Jpn., 66 (1993), 1104.
[8] HANDA M., MIKURIYA M., OKAWA H., Chem. Lett. (1989), 1663.
[9] MIKURIYA M., HANDA M., SHIGEMATSU S., FUNAKI S., ADACHI F., OKAWA H., Bull. Chem. Soc. Jpn., 65 (1992), 512.
[10] MIKURIYA M., KIDA S., UENO S., MURASE I., Bull. Chem. Soc. Jpn., 58 (1985), 1857.
[11] MIKURIYA M., KOTERA T., ADACHI F., HANDA M., KOIKAWA M., OKAWA H., Bull. Chem. Soc. Jpn., 68 (1995), 574.
[12] MIKURIYA M., JIAN X., IKEMI S., KAWAHASHI T., TSUTSUMI H., Bull. Chem. Soc. Jpn., 71 (1998), 2161.
[13] KAWAHASHI T., TSUTSUMI H., MIKURIYA M., Polyhedron, 15 (1996), 169.
[14] KAWAHASHI T., MIKURIYA M., NUKADA R., LIM J.-W., Bull. Chem. Soc. Jpn., 74 (2001), 323.
[15] MIKURIYA M., KOTERA T., Chem. Lett. (1998), 971.
[16] MIKURIYA M., ADACHI F., IWASAWA H., HANDA M., KOIKAWA M., OKAWA H., Inorg. Chim. Acta, 179 (1991), 3.
[17] MIKURIYA M., ADACHI F., IWASAWA H., HANDA M., KOIKAWA M., OKAWA H., Bull. Chem. Soc. Jpn., 67 (1994), 3263.
[18] MIKURIYA M., JIAN X., IKEMI S., KAWAHASHI T., TSUTSUMI H., NAKASONE A., LIM. J.-W., Inorg. Chim. Acta, 312 (2001), 183.
[19] KOTERA T., FUJITA A. MIKURIYA M., TSUTSUMI H., HANDA M., Inorg. Chem. Commun., 6 (2003), 322.
[20] MIKURIYA M., TSUTSUMI H., NUKADA R., HANDA M., SAYAMA Y., Bull. Chem. Soc. Jpn., 69 (1996), 3489.
[21] KOTERA T., MIKURIYA M., Chem. Lett. (2002), 654.
[22] MABBS F.E., MACHIN D.J., *Magnetism and Metal Complexes*, Chapman and Hall, London, 1973.
[23] BHARADWAJ P.K., JOHN E., XIE C.-L., ZHANG D., HENDRICKSON D.N., POTENZA J.A., SCHUGAR H.J., Inorg. Chem., 25 (1986), 4541.
[24] MISKOWSKI V.M., THICH J.A., SOLOMON R., SHUGAR H.J., J. Am. Chem. Soc., 98 (1976), 8344.
[25] DUNAJ-JURCO M., ONDREJOVIC G., MELNIK M., Coord. Chem. Rev., 83 (1988), 1.
[26] HOUSER R.P., TOLMAN W.B., Inorg. Chem., 34 (1955), 1632.
[27] HOUSER R.P., YOUNG V.G., TOLMAN W.B., J. Am. Chem. Soc., 118 (1996), 2101.
[28] MIKURIYA M., YAMAMOTO M., MORI W., Bull. Chem. Soc. Jpn., 67 (1994), 1348.
[29] HAY P.J., THIBEAULT J.C., HOFFMANN R., J. Am. Chem. Soc., 97 (1975), 4884.

Received 3 March 2003
Revised 21 March 2003

Materials Science, Vol. 21, No. 2, 2003

Spin-entropy driven charge-transfer phase transition in iron mixed-valence system*

N. KOJIMA**, M. ITOI, Y. ONO, M. OKUBO, M. ENOMOTO

Graduate School of Arts and Sciences, The University of Tokyo, Tokyo 153-8902, Japan

We have synthesized iron mixed-valence complexes, $(n\text{-}C_nH_{2n+1})_4N[Fe^{II}Fe^{III}X_3]$ (X = mto (C_2O_3S), dto ($C_2O_2S_2$), tto (C_2OS_3)) and have investigated their physical properties by means of ^{57}Fe Mössbauer spectroscopy, magnetic susceptibility and electrical resistivity measurements. From the analysis of ^{57}Fe Mössbauer spectra, magnetic susceptibility and electrical resistivity, we have discovered a new type of first order phase transition around 120 K for $(n\text{-}C_nH_{2n+1})_4N[Fe^{II}Fe^{III}(dto)_3]$ (n = 3, 4), where the charge-transfer transition between Fe^{II} and Fe^{III} occurs reversibly. In the higher temperature phase, the Fe^{III} (S = 1/2) and Fe^{II} (S = 2) sites are co-ordinated by six S atoms and six O atoms, respectively. In the lower temperature phase, on the other hand, the Fe^{III} (S = 5/2) and Fe^{II} (S = 0) sites are co-ordinated by six O atoms and six S atoms, respectively. Moreover, we have found a ferromagnetic phase transition in this system. The ferromagnetic order is induced by the charge-transfer interaction between the Fe^{III} and Fe^{II} sites. We propose various multifunctional properties for $(n\text{-}C_nH_{2n+1})_4N[Fe^{II}Fe^{III}(mto)_3]$ and $(n\text{-}C_nH_{2n+1})_4N[Fe^{II}Fe^{III}(tto)_3]$.

Key words: *spin crossover; ferromagnetism; charge-transfer; phase transition; mixed valence*

1. Introduction

Transition metal complexes with d^4-d^7 configuration have a possibility of spin transition between a low-spin state and a high spin state. The spin crossover phenomenon has recently gained renewed importance since the discovery of the photo-induced spin transition (called LIESST = Light Induced Excited Spin State Trapping) for $[Fe(ptz)_6](BF_4)_2$(ptz = 1-propyltetrazole) [1] and the thermally induced spin crossover transition with large thermal hysteresis around room temperature for a triazole bridged iron(II) complex [2, 3]. In the case of assembled hetero-metal complex system including spin-crossover complex ion, the spin transition behaves as a switching

---

* The paper was presented at the 13th Winter School on Coordination Chemistry, Karpacz, Poland, 9–13 December, 2002.

** Corresponding author, e-mail: cnori@mail.ecc.u-tokyo.ac.jp.

function to amplify the magnetic dimensionality, the magnetic interaction and to induce the magnetic ordering, which is schematically shown in Fig. 1.

In the spin-crossover system, the enthalpy term (H) dominates the Gibbs free energy ($G = H - TS$) in the low-spin state, while the entropy term ($-TS$) dominates the free energy in the high-spin state. Usual spin-crossover phenomenon occurs in on-site molecule. However, in the case of mixed-valence complexes whose spin states are situated in the spin-crossover region, it is expected that new types of conjugated phenomena coupled with spin and charge take place between different metal ions in order to minimize the free energy in the whole system.

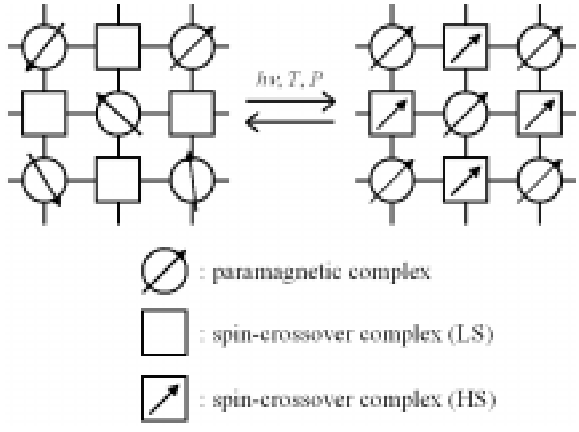

Fig. 1. Assembled hetero-metal complex system including spin-crossover complex ion. The spin crossover transition behaves as a switching function to control the magnetic interaction and the magnetic ordering in the assembled hetero-metal complex system

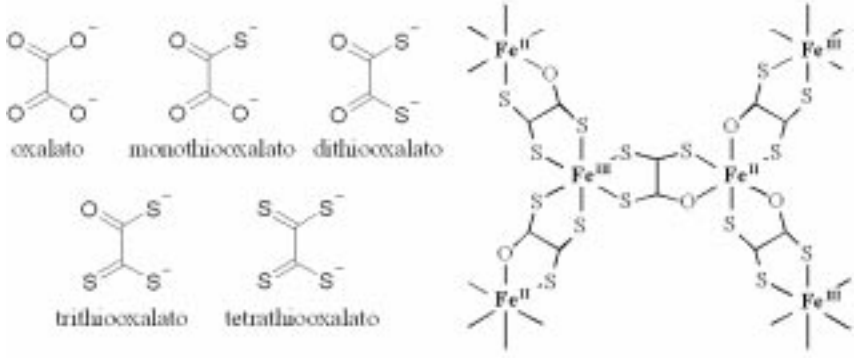

Fig. 2. Oxalato derivatives as bridging ligand, and the network structure of $[Fe^{II}Fe^{III}(tto)_3]$ complex

From these viewpoints, we have synthesized iron mixed-valence complexes whose spin states are situated in the spin-crossover region. It is well known that tris(dithiocarbamato)

iron(III) complexes show the spin-crossover transition [4]. In these complexes, Fe^{III} is co-ordinated by six S atoms. In the cases of $Fe^{III}O_6$ and $Fe^{II}O_6$ octahedra, on the other hand, there has been no report on the thermally induced spin-crossover transition at ambient pressure. Taking account of these iron complexes, we have systematically synthesized iron mixed valence complexes by using oxalato derivatives as bridging ligands, which is shown in Fig. 2. Recently, we have discovered a new type of phase transition coupled with spin and charge around 120 K for $(n\text{-}C_3H_7)_4N[Fe^{II}Fe^{III}(dto)_3]$[5,6].

In this paper, we report and discuss the spin-entropy driven charge-transfer phase transition in $(n\text{-}C_nH_{2n+1})_4N[Fe^{II}Fe^{III}(dto)_3]$(dto = dithiooxalato($C_2O_2S_2$)). Moreover, we put forward various multifunctional properties for $(n\text{-}C_nH_{2n+1})_4N[Fe^{II}Fe^{III}(mto)_3]$ (mto = monothiooxalato(C_2O_3S)) and $(n\text{-}C_nH_{2n+1})_4N[Fe^{II}Fe^{III}(tto)_3]$ (tto = trithiooxalato(C_2OS_3)).

2. Experimental

K_2(mto), K_2(dto) and K_2(tto) were synthesized in the similar way as reported in Ref. [7, 8]. $(n\text{-}C_nH_{2n+1})_4N[Fe^{II}Fe^{III}(dto)_3]$($n$ = 3–6) was synthesized in a similar way to prepare $(n\text{-}C_3H_7)_4N[M^{II}Cr^{III}(dto)_3]$(M = Fe, Co, Ni, Zn)[9]. A solution of KBa[Fe $(dto)_3]\cdot 6H_2O$[8] in a methanol–water mixture was stirred and a solution of $FeCl_2\cdot 4H_2O$ and $(n\text{-}C_nH_{2n+1})_4NBr$ in a methanol-water mixture was added. In this way, $(n\text{-}C_nH_{2n+1})_4N$ $[Fe^{II}Fe^{III}(dto)_3]$ was obtained as black coloured precipitate. In this similar way, $(n\text{-}C_nH_{2n+1})_4N[Fe^{II}Fe^{III}(mto)_3]$ and $(n\text{-}C_nH_{2n+1})_4N[Fe^{II}Fe^{III}(tto)_3]$ were synthesized.

The static magnetic susceptibility was measured by a Quantum Design MPMS5 SQUID susceptometer. Powdered sample of 10 mg was wrapped in polyethylene film and held in a plastic straw. The magnetic susceptibility obtained was corrected for the background and the core diamagnetism estimated from Pascal's constants. In the case of ^{57}Fe Mössbauer spectroscopic measurement, ^{57}Co in Rh was used at 298 K as a Mössbauer source. The spectra were calibrated by using the six lines of a body-centred cubic iron foil (α-Fe), the centre of which was taken as zero isomer shift. The hyperfine parameters were obtained by least-squares fitting to Lorentzian line shapes.

3. Results and discussion

The crystal structure of $(n\text{-}C_nH_{2n+1})_4N[Fe^{II}Fe^{III}(dto)_3]$ consists of two-dimensional honeycomb network structure, $[Fe^{II}Fe^{III}(dto)_3]_\infty$, and intercalated $(n\text{-}C_nH_{2n+1})_4N^+$ cations. Figure 3 shows the two-dimensional honeycomb network structure with alternating array of Fe^{II} and Fe^{III} atoms through dto bridges, and the alternation layer structure. At room temperature, the Fe^{III} (S = 1/2) and Fe^{II} (S = 2) sites are co-ordinated by six S atoms and six O atoms, respectively, which has been confirmed by means of ^{57}Fe Mössbauer spectroscopy. The space group is $P6_3$, consequently the conformations of the $Fe^{II}(O_2C_2S_2)_3$ and $Fe^{III}(S_2C_2O_2)_3$ octahedra in one $[Fe^{II}Fe^{III}(dto)_3]_\infty$ layer are different from those in the adja-

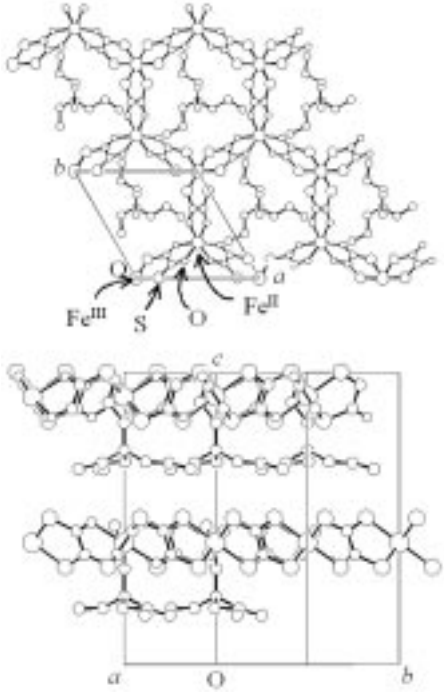

Fig. 3. Crystal structure of (n-C_3H_7)$_4$N[$Fe^{II}Fe^{III}$(dto)$_3$] at 298 K

cent one $[Fe^{II}Fe^{III}(dto)_3]_\infty$ layer. One layer consists of Λ configuration of $Fe^{II}(O_2C_2S_2)_3$ and Δ configuration of $Fe^{III}(S_2C_2O_2)_3$, while the adjacent layer consists of Δ configuration of $Fe^{II}(O_2C_2S_2)_3$ and Λ configuration of $Fe^{III}(S_2C_2O_2)_3$. In $(n\text{-}C_nH_{2n+1})_4N^+$, the axial propyl chain points into the cavity of honeycomb network.

Figure 4 shows χT as a function of temperature for (n-C_3H_7)$_4$N[$Fe^{II}Fe^{III}$(dto)$_3$]. As shown in Fig. 4, χT increases with decreasing temperature except in the temperature region between 70 K and 130 K and shows a maximum around 10 K, which implies that the magnetic interaction between Fe^{II} and Fe^{III} in (n-C_3H_7)$_4$N[$Fe^{II}Fe^{III}$(dto)$_3$] is ferromagnetic and the ferromagnetic transition takes place around 10 K. In fact, as shown in Fig. 4, the spontaneous magnetization appears at 7 K. The field cooled magnetization (FCM) under the external magnetic field of 30 G shows a rapid increase below 8 K and shows a tendency to saturate below 6 K. When the magnetic field is switched off at 1.8 K, the remnant magnetization (RM) remains, and vanishes at 7 K. The zero-field cooled magnetization (ZFCM) and FCM curves meet at 7 K where the magnetic hysteresis disappears. Consequently, the Curie temperature is estimated at 7 K.

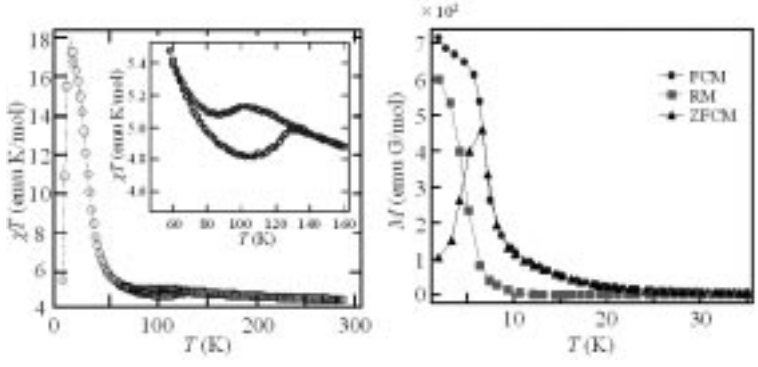

Fig. 4. Temperature dependence of χT under the external magnetic field of 5000 G and the temperature dependence of magnetization under the external magnetic field of 30 G for (n-C_3H_7)$_4$N[$Fe^{II}Fe^{III}$(dto)$_3$]. FCM, RM, and ZFCM denote the field-cooled magnetization, the remnant magnetization, and the zero-field cooled magnetization, respectively

Turning to χT vs. T curve in Fig.4, there is an anomalous drop with thermal hysteresis between 70 K and 130 K, which implies a first-order phase transition. In order to elucidate the detailed mechanism of the phase transition around 120 K, we investigated the ^{57}Fe Mössbauer spectra of $(n\text{-}C_3H_7)_4N[Fe^{II}Fe^{III}(dto)_3]$ at 105 K, 124 K and 130 K, which is shown in Fig. 5.

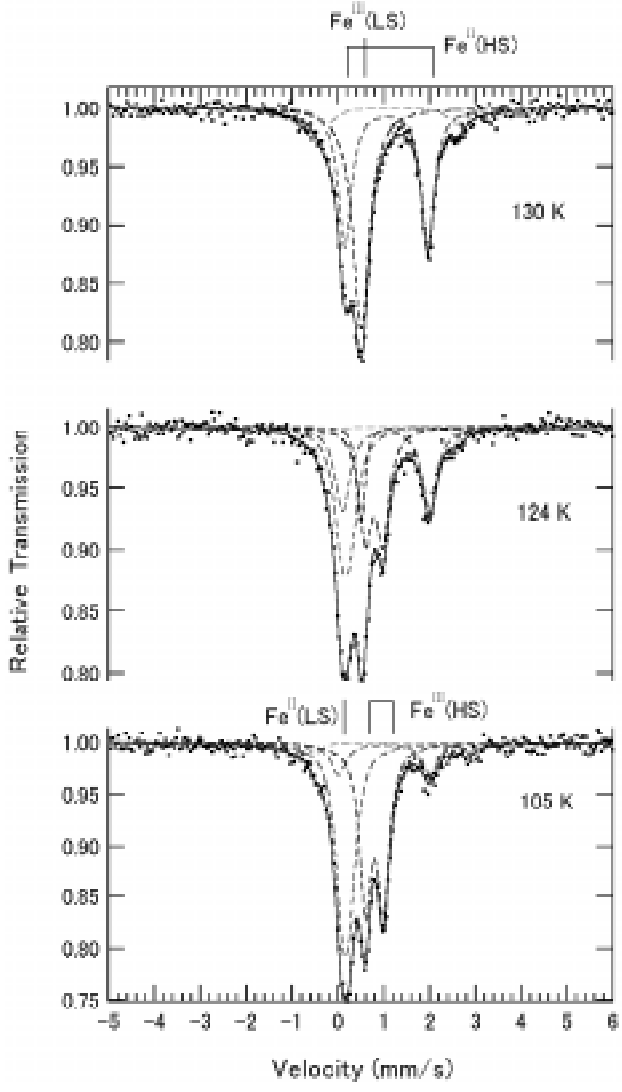

Fig. 5. ^{57}Fe Mössbauer spectra of $(n\text{-}C_3H_7)_4N[Fe^{II}Fe^{III}(dto)_3]$ at 130 K, 124 K and 105 K

At 130 K, the spectrum with two branches at 0.16 mm/s and 1.96 mm/s can be assigned to that for the high-spin state of the Fe^{II} site co-ordinated by six O atoms. The

isomer shift (*IS*) and the quadrupole splitting (*QS*) of the ^{57}Fe Mössbauer spectrum with two branches at 0.16 mm/s and 1.86 mm/s are estimated at 1.06 mm/s and 1.80 mm/s, respectively, whose values are quite similar to those (*IS* = 1.30 mm/s, *QS* = 1.79 mm/s at 78 K) of the ^{57}Fe Mössbauer spectrum for the Fe^{II}(*S* = 2) in $(n\text{-}C_4H_9)_4N[Fe^{II}Fe^{III}(ox)_3]$ [10], where the Fe^{II} site is co-ordinated by six O atoms. The spectrum with single peak at 0.46 mm/s can be assigned to that for the low-spin state of the Fe^{III} site co-ordinated by six S atoms. The *IS* and *QS* of the ^{57}Fe Mössbauer spectrum with single peak at 0.46 mm/s are quite similar to those (*IS* = 0.33 mm/s, *QS* = 0.35 mm/s at 196 K) of the ^{57}Fe Mössbauer spectrum for the Fe^{III}(*S* = 1/2) in $KBa[Fe^{III}(dto)_3]$, where the Fe^{III} is co-ordinated by six S atoms[11]. As shown in Fig. 5, with decreasing temperature, the line profile of ^{57}Fe Mössbauer spectra remarkably changes between 130 K and 105 K. At 105 K, the intensity of the spectrum corresponding to the Fe^{II} site decreases by 80% and new lines appear at about 0.2 mm/s and 1.0 mm/s, which implies a drastic change in the Fe electronic states of $(n\text{-}C_3H_7)_4N[Fe^{II}Fe^{III}(dto)_3]$ between 130 K and 105 K.

Comparing with the typical values of *IS* and *QS* of ^{57}Fe Mössbauer spectra for Fe^{II}(*S* = 0), Fe^{II}(*S* = 2), Fe^{III}(*S* = 1/2), and Fe^{III}(*S* = 5/2), the ^{57}Fe Mössbauer spectra of $(n\text{-}C_3H_7)_4N[Fe^{II}Fe^{III}(dto)_3]$ between 130 K and 105 K are assigned as shown in Fig. 5. In this way, from the analysis of ^{57}Fe Mössbauer spectra, we have discovered a new type of the first order phase transition around 120 K for $(n\text{-}C_nH_{2n+1})_4N[Fe^{II}Fe^{III}(dto)_3]$(*n* = 3, 4), where the charge-transfer transition between Fe^{II} and Fe^{III} occurs reversibly. In the higher temperature phase, the Fe^{III} (*S* = 1/2) and Fe^{II} (*S* = 2) sites are co-ordinated by six S atoms and six O atoms, respectively. In the lower temperature phase, on the other hand, the Fe^{III} (*S* = 5/2) and Fe^{II} (*S* = 0) sites are co-ordinated by six O atoms and six S atoms, respectively.

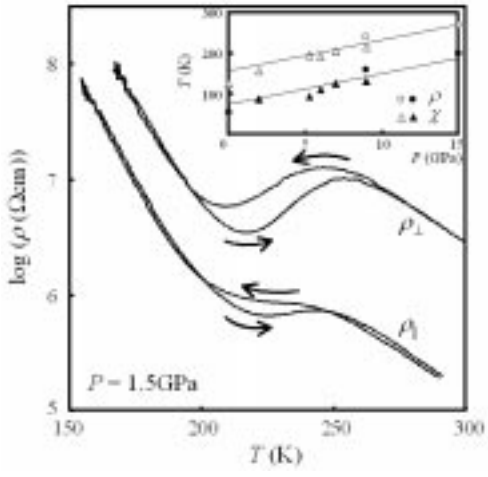

Fig. 6. Temperature dependence of the intra-layer ($\rho_{||}$) and inter-layer ($\rho_{\perp}$) resistivities of $(n\text{-}C_3H_7)_4N[Fe^{II}Fe^{III}(dto)_3]$ at 1.5 GPa. Arrows denote the direction of the thermal process. Inset shows the charge-transfer phase transition as a function of applied pressure determined by the magnetic susceptibility (χ) and the electrical resistivity (ρ) measurements. ○ Δ and ● ▲ denote the upper limit and the lower limit of the charge-transfer phase transition, respectively

In order to prove the charge-transfer phase transition in $(n\text{-}C_3H_7)_4N[Fe^{II}Fe^{III}(dto)_3]$, we have measured the electrical resistivity for the single crystal. Figure 6 shows the

temperature dependence of the intra-layer ($\rho_{||}$) and inter-layer ($\rho_{\perp}$) resistivity of (n-C_3H_7)$_4$N[$Fe^{II}Fe^{III}$ (dto)$_3$] at 1.5 GPa. The inset in Fig. 6 shows the critical temperature (T_c) of the charge-transfer phase transition as a function of applied pressure. At 1.5 GPa, the charge-transfer phase transition takes place between 200 K and 270 K. As shown in Fig. 6, both of the intra-layer and inter-layer resistivities show an anomalous drop due to the charge-transfer phase transition. The intra-layer resistivity is one order of magnitude lower than that of the inter-layer one, which is attributed to the electron hopping between Fe^{II} and Fe^{III} in the two-dimensional honeycomb network structure of [$Fe^{II}Fe^{III}$(dto)$_3$]$_\infty$.

Consequently, it is concluded that (n-C_nH_{2n+1})$_4$N[$Fe^{II}Fe^{III}$(dto)$_3$](n = 3, 4) undergoes a thermally induced charge-transfer phase transition coupled with the change of spin configuration around 120 K, where the charge-transfer transition occurs reversibly between the t_{2g} orbitals of the Fe^{II} and Fe^{III} sites, which is schematically shown in Fig. 7. The driving force responsible for the charge-transfer phase transition would be the difference in spin entropy between the higher and the lower temperature phases. It should be noted that the spin entropy in the higher temperature phase is Rln(2×5) = 19.15 J·K^{-1}·mol^{-1} and that in the lower temperature phase is Rln(1×6) = 14.90 J·K^{-1}·mol^{-1}, where R is the gas constant. Therefore, the spin-entropy gain expected from the charge transfer is estimated at 4.25 J·K^{-1}·mol^{-1}. Since the observed entropy gain at the charge-transfer phase transition in (n-C_3H_7)$_4$N[$Fe^{II}Fe^{III}$(dto)$_3$] is 9.20 J·K^{-1}·mol^{-1} [12], the entropy change originating in intra-molecular vibration is quite smaller than in normal spin-crossover transition. For example, about 35 J·K^{-1}·mol^{-1} was estimated for the vibrational contribution to the entropy change in the spin-crossover phenomenon observed in [Fe(phen)$_2$(NCS)$_2$] [13].

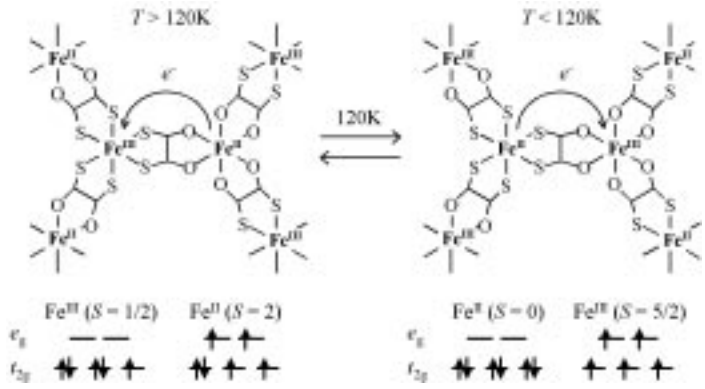

Fig. 7. Schematic representation of the charge-transfer phase transition around 120 K for (n-C_3H_7)$_4$N[$Fe^{II}Fe^{III}$(dto)$_3$]

The phase diagram of (n-C_nH_{2n+1})$_4$N[$Fe^{II}Fe^{III}$(dto)$_3$] is schematically shown in Fig. 8. The vertical axis denotes the free energy ($G = H - TS$). HTP and LTP denote the high-temperature phase with Fe^{II}(S = 2), Fe^{III}(S = 1/2) spin configuration and the

low-temperature phase with $Fe^{II}(S = 0)$, $Fe^{III}(S = 5/2)$ spin configuration, respectively. T_c is the transition temperature between HTP and LTP. The first-order phase transition around 120 K for $(n\text{-}C_nH_{2n+1})_4N[Fe^{II}Fe^{III}(dto)_3](n = 3, 4)$ is regarded as spin-entropy driven charge-transfer phase transition caused by minimizing the free energy in the whole system. As shown in Fig. 8, T_c strongly depends on the difference of enthalpy (ΔH) between HTP and LTP. With increasing ΔH, T_c presumably becomes to be higher. If the charge-transfer phase transition is of the first order without thermal hysteresis or of the second order, the hopping of Avogadro's number electrons would take place between the Fe^{II} and Fe^{III} sites, which would cause a spin-entropy driven metallization at T_c.

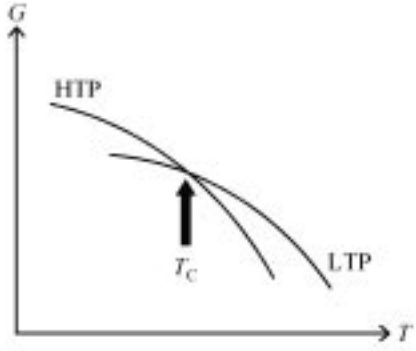

Fig. 8. Phase diagram of $(n\text{-}C_nH_{2n+1})_4N[Fe^{II}Fe^{III}(dto)_3]$. The vertical axis denotes the free enrgy ($G = H - TS$). HTP and LTP denote the high-temperature phase with $Fe^{II}(S = 2)$, $Fe^{III}(S = 1/2)$ spin configuration and the low-temperature phase with $Fe^{II}(S = 0)$, $Fe^{III}(S = 5/2)$ spin configuration, respectively. T_c denotes the transition temperature of the charge-transfer phase transition

Next, we discuss the mechanism of ferromagnetic ordering in $(n\text{-}C_nH_{2n+1})_4N[Fe^{II}Fe^{III}(dto)_3]$. As mentioned already, the spin states of the Fe^{II} and Fe^{III} sites in the lower temperature phase are the low-spin state ($S = 0$) and the high spin state ($S = 5/2$), respectively, where the super-exchange interaction through the sequence of Fe^{III}–(dto)–Fe^{II}–(dto)–Fe^{III} is considered to be negligibly small. The most plausible mechanism responsible for the ferromagnetic ordering at 7 K and 11 K for $(n\text{-}C_3H_7)_4N[Fe^{II}Fe^{III}(dto)_3]$ and $(n\text{-}C_4H_9)_4N[Fe^{II}Fe^{III}(dto)_3]$ is the charge-transfer interaction between the Fe^{II} and Fe^{III} sites. In the lower temperature phase of $(n\text{-}C_nH_{2n+1})_4N[Fe^{II}Fe^{III}(dto)_3](n = 3, 4)$, the ground state wave function perturbed by the charge-transfer interaction between the Fe^{II} and Fe^{III} sites is expressed as

$$\Psi = (1 - \alpha)^2\{\varphi_i(Fe^{II}(t_2{}^6))\varphi_j(Fe^{III}(t_2{}^3e^2))\} + \alpha\{\varphi_i(Fe^{III}(t_2{}^5))\varphi_j(Fe^{II}(t_2{}^4e^2))\}$$

where α denotes the degree of the charge-transfer interaction. Each Fe^{III} site in the lower temperature phase accepts a t_2 electron with down spin, because the t_2 and e orbitals in the Fe^{III} site are both exactly half occupied. Therefore, the spin configuration between Fe^{II} and Fe^{III} in the virtual state, $\varphi_i(Fe^{III}(t_2{}^5))\ \varphi_j(Fe^{II}(t_2{}^4e^2))$, is ferromagnetically coupled. In this way, the valence delocalization between the Fe^{II} ($S = 0$) and Fe^{III} ($S = 5/2$) sites induces the ferromagnetic ordering in the lower temperature phase of $(n\text{-}C_nH_{2n+1})_4N[Fe^{II}Fe^{III}(dto)_3]$ ($n = 3, 4$), which is the same mechanism of the ferromagnetic ordering ($T_c = 5.5$ K) in Prussian blue, $Fe^{III}{}_4[Fe^{II}(CN)_6]_3$[14, 15].

Finally, we propose the possibility of various multifunctional properties for n-$C_nH_{2n+1})_4N[Fe^{II}Fe^{III}(mto)_3]$ and $(n$-$C_nH_{2n+1})_4N[Fe^{II}Fe^{III}(tto)_3]$. These complexes have the possibility of large dielectric response and non-linear optical effect because the $Fe^{III}(SOC_2O_2)_3$ octahedra in $(n$-$C_nH_{2n+1})_4N[Fe^{II}Fe^{III}(mto)_3]$ and the $Fe^{II}(SOC_2S_2)_3$ octahedra in $(n$-$C_nH_{2n+1})_4N[Fe^{II}Fe^{III}(tto)_3]$ lose the inversion-symmetry. Consequently, the following multifunctional properties are expected for $(n$-$C_nH_{2n+1})_4N[Fe^{II}Fe^{III}X_3]$ (X = mto, dto, tto):

- spin-entropy driven insulator-to-metal transition at the charge-transfer phase transition,
- coexistence of ferromagnet and ferroelectrics,
- high T_c ferromagnets caused by charge-transfer interaction,
- non-linear optical effects induced by magnetic ordering,
- photo-induced magnetic ordering.

Acknowledgement

This work has been supported by a Grant-in-Aid for Scientific Research from the Ministry of Education, Culture, Sports, Science and Technology, Japan.

References

[1] DECURTINS S., GÜTLICH P., KÖHLER C.P., SPIERING H., HAUSER A., Chem. Phys. Lett., 105 (1984), 1.
[2] KRÖBER J., CODJOVI E., KAHN O., GROLIÈRE F., JAY C., J. Am. Chem. Soc., 115 (1993), 9810.
[3] KAHN O., MARTINEZ C.J., Science, 279 (1998), 44.
[4] CAMBI L., CAGNASSO A., Atti Accad. Naz. Lincei, 13 (1931), 809.
[5] KOJIMA N., AOKI W., SETO M., KOBAYASHI Y., MAEDA YU., Synth. Metals, 121 (2001), 1796.
[6] KOJIMA N., AOKI W., ITOI M., ONO Y., SETO M., KOBAYASHI Y., MAEDA YU, Solid State Commun., 120 (2001),165.
[7] STORK W., MATTES R., Angew. Chem. Int. Ed., 87 (1975), 452.
[8] LEITHEISER M., COUCOUVANIS D., J. Inorg. Nucl. Chem., 39 (1977), 811.
[9] ÔKAWA H., MITSUMI M., OHBA M., KODERA M., MATSUMOTO N., Bull. Chem. Soc. Jpn., 67 (1994), 2139.
[10] IIJIMA S., KATSURA T., TAMAKI H., MITSUMI M., MATSUMOTO N., ÔKAWA H., Mol. Cryst. Liq. Cryst., 233 (1993), 263.
[11] BIRCHALL T., TUN K.M., Inorg. Chem., 15 (1976), 376.
[12] NAKAMOTO T., MIYAZAKI Y., ITOI M., ONO Y., KOJIMA N., SORAI M., Angew. Chem. Int. Ed., 40 (2001), 4716.
[13] SORAI M., SEKI S., J. Phys. Chem. Solids, 35 (1974), 555.
[14] MAYOH B., DAY P., J. Chem. Soc. Dalton (1974), 846.
[15] MAYOH B., DAY P., J. Chem. Soc. Dalton. (1976), 1483.

Received 10 March 2003
Revised 26 March 2003

Materials Science, *Vol. 21*, *No. 2*, *2003*

Spin crossover in a supramolecular Fe^{II}–Fe^{III} system*

HIROMI OHTA[1], YUKINARI SUNATSUKI[1], YUICHI IKUTA[2], NAOHIDE MATSUMOTO[2], SEIICHIRO IIJIMA[3], HARUO AKASHI[4], TAKASHI KAMBE[5], MASAAKI KOJIMA[1**]

[1]Department of Chemistry, Faculty of Science, Okayama University, Tsushima, Okayama 700-8530, Japan

[2]Department of Chemistry, Faculty of Science, Kumamoto University, Kumamoto 860-8555, Japan

[3]National Institute of Advanced Industrial Science and Technology, Tsukuba 305-8566, Japan

[4]Research Institute of Natural Sciences, Okayama University of Science, Ridai-cho, Okayama 700-0005, Japan

[5]Department of Physics, Faculty of Science, Okayama University, Tsushima, Okayama 700-8530, Japan

The structure of $[Fe^{II}(H_3L)](ClO_4)_2 \cdot 3H_2O$, where H_3L is a tripodal hexadentate ligand derived from the 1:3 condensation of tris(2-aminoethyl)amine and 4-formylimidazole, has been determined by X-ray crystallography at 113 and 293 K. A spin transition was inferred from the Fe–N bond distances. The temperature dependence of the magnetic susceptibility revealed that the complex undergoes a gradual spin transition in the temperature range of 150–270 K. A mixed-valence complex, $[Fe^{II}(H_3L)][Fe^{III}(L)](BF_4)_2 \cdot 1.5H_2O$, was prepared by the controlled deprotonation of the protonated species, $[Fe^{II}(H_3L)](BF_4)_2 \cdot 1.5H_2O$, under aerobic conditions, and the X-ray structure was determined at 293 K. Two species, $[Fe^{II}(H_3L)]^{2+}$ and $[Fe^{III}(L)]$, are linked by imidazole–imidazolate (NH···N) hydrogen bonds to form a puckered sheet structure. Magnetic susceptibility measurements and Mössbauer spectra provided an evidence for spin-crossover at both the Fe^{II} and Fe^{III} sites. There are three accessible electronic states: (LS Fe^{II}–LS Fe^{III}), (HS Fe^{II}–LS Fe^{III}), and (HS Fe^{II}–HS Fe^{III}) that occur in passing from lower to higher temperatures.

Keywords: *spin crossover; hydrogen bonds; tripodal ligand*

1. Introduction

Increasing attention has been paid to the synthesis of compounds showing bistable behaviour, because they can be used as molecular switches in electronic devices [1].

---

* The paper was presented at the 13th Winter School on Coordination Chemistry, Karpacz, Poland, 9–13 December, 2002.

**Corresponding author, e-mail: kojima@cc.okayama-u.ac.jp.

The phenomenon of spin crossover represents one of the most spectacular examples of molecular bistability [2]. Cooperative spin crossover, where an interaction between spin crossover sites occurs within a crystal lattice, is the dominant factor governing bistability [3]. A polymeric strategy has been widely used to obtain a spin crossover material that has a large cooperative effect, where the spin crossover sites are linked together by chemical bridges to form a linear chain structure [1, 4]. Mononuclear spin-crossover Fe^{II} compounds exhibiting strong intermolecular interactions, such as hydrogen bonding [5, 6] and π–π stacking [3, 7, 8] interactions are rather scarce, and the requirements for sharp spin transition are difficult to control. Our strategy controlling a spin crossover behaviour is based on the formation of an extended two-dimensional (2D) sheet structure, which arises from intermolecular hydrogen bonds.

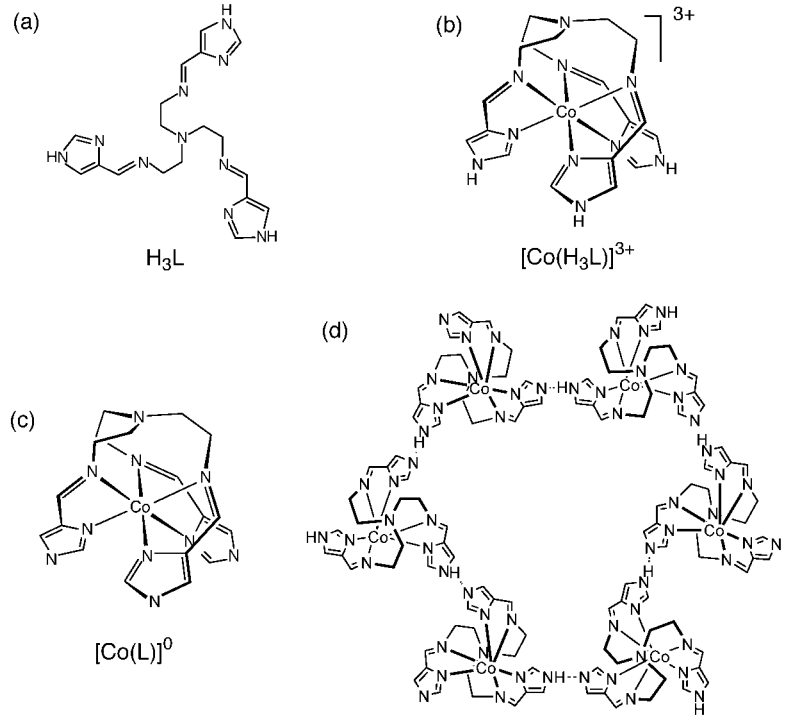

Fig. 1. The tripodal H_3L ligand (a); the structure of $[Co^{III}(H_3L)]^{3+}$ (b); the structure of $[Co^{III}(L)]^0$ (c) and the hexanuclear structure as repeating unit of the 2D sheet constructed from intermolecular imidazole–imidazolate hydrogen bonds between $[Co^{III}(H_3L)]^{3+}$ and $[Co^{III}(L)]^0$ (d)

We have focused on the homochiral 2D extended network structure of $[Co^{III}(H_3L)]$-$[Co^{III}(L)]X_3$ [9], arising from the intermolecular imidazole–imidazolate hydrogen bonds between $[Co^{III}(H_3L)]^{3+}$ and $[Co^{III}(L)]^0$, where H_3L denotes a tripodal hexadentate ligand derived from the 1:3 condensation of tris(2-aminoethyl)amine and 4-formylimidazole (Fig. 1). This formally hemi-deprotonated species, $[Co^{III}(H_{1.5}L)]X_{1.5}$ (i.e., $[Co^{III}(H_3L)]$-$[Co^{III}(L)]X_3$), was prepared by the controlled deprotonation of the protonated species,

$[Co^{III}(H_3L)]X_3$. A similar synthetic procedure for the iron(II) species gave a mixed-valence Fe^{II}–Fe^{III} spin crossover compound with the formula $[Fe^{II}(H_3L)][Fe^{III}(L)](BF_4)_2 \cdot 1.5H_2O$ (**3**). This paper reports on the preparation, structure, and magnetic properties of **3** and related complexes.

2. Experimental

2.1. Preparation of $[Fe^{II}(H_3L)](ClO_4)_2 \cdot 3H_2O$ (1), $[Fe^{II}(H_3L)](BF_4)_2 \cdot 1.5H_2O$ (2), and $[Fe^{II}(H_3L)][Fe^{III}(L)](BF_4)_2 \cdot 1.5H_2O$ (3)

The H_3L ligand was prepared by the reaction of tris(2-aminoethyl)amine and 4-formylimidazole in a 1:3 molar ratio in methanol. The solution containing the H_3L ligand was then mixed with a methanol solution of $FeCl_2 \cdot 4H_2O$ in a 1:1 molar ratio. The mixture was heated under reflux for 30 min, and after cooling, $NaClO_4$ (3 equiv) was added to yield a yellow-orange precipitate. The precipitate was filtered and re-crystallized from methanol containing a small volume of ascorbic acid. Found: C, 31.61; H, 4.30; N, 20.59%. Calc. for $C_{18}H_{30}Cl_2Fe_1N_{10}O_{11} = [Fe^{II}(H_3L)](ClO_4)_2 \cdot 3H_2O$ (**1**): C, 31.37; H, 4.39; N, 20.32. $[Fe^{II}(H_3L)](BF_4)_2 \cdot 1.5H_2O$ (**2**) was isolated by the addition of excess $NaBF_4$ to a methanol solution of $[Fe^{II}(H_3L)]Cl_2$. Found: C, 34.24; H, 4.62; N, 21.52%. Calc. for $C_{18}H_{27}B_2F_8Fe_1N_{10}O_{1.5}$: C, 33.95; H, 4.27; N, 21.99.

To a warm methanol solution of **2**, an aqueous solution of NaOH (1:1 molar ratio) was added under aerobic conditions. The colour of the solution gradually changed from yellow to dark green, and a mixed-valence complex with the chemical formula $[Fe^{II}(H_3L)][Fe^{III}(L)](BF_4)_2 \cdot 1.5H_2O$ (**3**) was produced. Found: C, 40.25; H, 4.61; N, 26.12%. Calc. for $C_{36}H_{48}B_2F_8Fe_2N_{20}O_{1.5}$: C, 40.40; H, 4.52; N, 26.18%.

2.2. Physical measurements

The samples' magnetic susceptibilities were measured using a Quantum Design MPMS5 and MPMS2 SQUID susceptometer in the temperature range of 2–350 K under an applied magnetic field of 1 T. Mössbauer spectra were recorded using a Wissel 1200 spectrometer and a proportional counter. A $^{57}Co(Rh)$ radioactive source moving in a constant acceleration mode was used. The isomer shifts were calculated relative to a metallic iron foil.

2.3. X-ray crystal structure analysis of $[Fe^{II}(H_3L)](ClO_4)_2 \cdot 3H_2O$ (1) and $[Fe^{II}(H_3L)][Fe^{III}(L)](BF_4)_2 \cdot 1.5H_2O$ (3)

X-ray measurements were taken using a Rigaku RAXIS-IV imaging plate area detector employing graphite monochromated Mo K_α radiation (λ = 0.71073 Å). The structure was

solved using direct methods, and was refined using full-matrix least-squares procedures employing the CrystalStructure crystallographic software package [10]. Crystal data at 113 K for **1**: Formula $[Fe^{II}(H_3L)](ClO_4)_2 \cdot 3H_2O = C_{18}H_{30}Cl_2FeN_{10}O_{11}$, Fw = 689.25, orange, prism, trigonal, space group *R*32(h) (No. 155), $a = b = 11.851(1)$, $c = 34.2177(2)$ Å, $V = 4161.7(5)$ Å^3, $Z = 6$, $D_{calc} = 1.650$ g·cm^{-3}, $\mu = 0.810$ mm^{-1}, No. of reflections measured = 1228, unique reflections = 1228, $R = 0.163$ [1152 $I > 2\sigma(I)$], $R_w = 0.212.(2)$. Crystal data at 293 K for **1**: Formula $[Fe^{II}(H_3L)](ClO_4)_2 \cdot 3H_2O = C_{18}H_{30}Cl_2FeN_{10}O_{11}$, Fw = 689.25, orange, prism, trigonal, space group *R*32(h) (No. 155), $a = b = 12.0774(9)$, $c = 35.8111(2)$ Å, $V = 4523.7(5)$ Å^3, $Z = 6$, $F(000) = 2136$, $D_{calc} = 1.518$ g cm^{-3}, $\mu = 0.810$ mm^{-1}, No. of reflections measured = 1322, Unique reflections = 1322, $R = 0.163$ [1152 $I > 2\sigma(I)$], $R_w = 0.168$. The systematic extinction of the X-ray diffraction data at both temperatures suggested either the space group *R*32 or *R*3*m*. The structure was well determined when *R*32 was assumed, while we could not determine the structure when *R*3*m* was assumed. Thus, the space group *R*32 was selected.

Crystal data for **3** at 293 K: Formula $[Fe^{II}(H_3L)][Fe^{III}(L)](BF_4)_2 \cdot 1.5H_2O = C_{36}H_{48}B_2F_8Fe_2N_{20}O_{1.5}$, Fw = 1070.2, dark green, block, trigonal, space group *P*3 (No. 143), $a = b = 11.9074(2)$, $c = 28.5477(4)$ Å, $V = 3505.38(8)$ Å^3, $Z = 6$, $D_{calc} = 1.521$ g·cm^{-3}, No. of reflections measured = 19023, unique reflections = 5188 ($R_{int} = 0.033$), $R = 0.080$ [7005 $I > 2\sigma(I)$], and $R_w = 0.117$.

3. Results and discussion

3.1. Preparation, structure and magnetic properties of $[Fe^{II}(H_3L)](ClO_4)_2 \cdot 3H_2O$ (1)

The tripodal H_3L ligand was prepared by the reaction of tris(2-aminoethyl)amine and 4-formylimidazole in a 1:3 molar ratio in methanol. This ligand solution was used without isolation for the synthesis of the iron(II) complexes. The $[Fe^{II}(H_3L)](ClO_4)_2 \cdot 3H_2O$ (**1**) complex was obtained as yellow-orange crystals by mixing the ligand solution, $FeCl_2 \cdot 4H_2O$, and $NaClO_4$ in a 1:1:3 molar ratio. The crude product was purified by recrystallization from methanol containing a small amount of ascorbic acid as a reducing agent.

The structure of **1** was determined by X-ray crystallography at 113 and 293 K. Figure 2 shows an ORTEP drawing for the cation of complex **1**. The iron atom is in an approximately octahedral environment composed of three facially co-ordinated imine nitrogen atoms and three imidazole nitrogen atoms. At 293 K, the average Fe–N(imine) and Fe–N(imidazole) bond distances are 2.18(2) and 2.20(2) Å, respectively. These values are typical of a high-spin (HS) iron(II) ion [3, 11, 12]. At 113 K, the Fe–N bond distances shorten by about 0.2 Å versus those at 293 K: the average

Fe–N(imine) and Fe–N(imidazole) bond distances are 2.02(2) and 1.98(1) Å, respectively, suggestive of a low-spin (LS) Fe^{II} species.

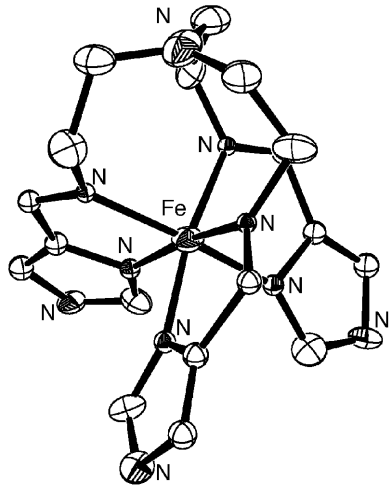

Fig. 2. An ORTEP drawing of the cation of $[Fe^{II}(H_3L)](ClO_4)_2 \cdot 3H_2O$ (**1**) showing the 50% probability ellipsoid. The hydrogen atoms have been omitted for clarity

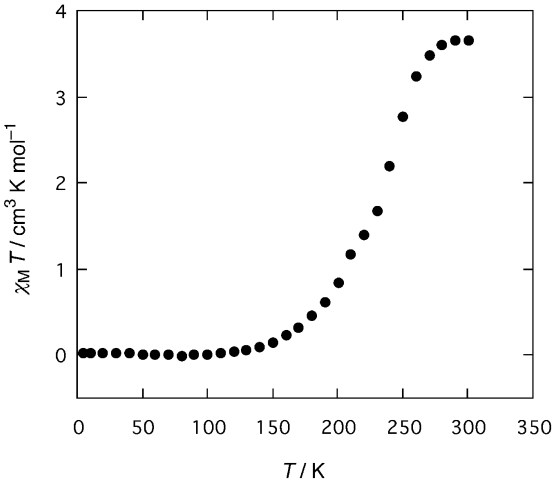

Fig. 3. A plot of $\chi_M T$ versus T for $[Fe^{II}(H_3L)](ClO_4)_2 \cdot 3H_2O$ (**1**)

The magnetic properties of **1** are shown in Fig. 3 in the form of a $\chi_M T$ versus T curve, in which χ_M is the molar magnetic susceptibility and T is the absolute temperature. Complex **1** shows a spin transition in the temperature range of 150–270 K. Above 270 K, the complex is in the HS state, while below 150 K, it is in the LS state. These results are consistent with the X-ray structure study.

3.2. Preparation, structure and properties of $[Fe^{II}(H_3L)][Fe^{III}(L)](BF_4)_2 \cdot 1.5H_2O$ (3)

The reaction of $[Fe^{II}(H_3L)](BF_4)_2 \cdot 1.5H_2O$ (**2**) with NaOH (1:1 ratio) under aerobic conditions yielded a dark green, mixed-valence complex, $[Fe^{II}(H_3L)][Fe^{III}(L)](BF_4)_2 \cdot 1.5H_2O$ (**3**). Deprotonation and oxidation of $[Fe^{II}(H_3L)]^{2+}$ took place during the course of the reaction to generate the fully-deprotonated species $[Fe^{III}(L)]$, which functions as a component of the mixed valence complex, **3**. Thus, this reaction is an example of a proton-coupled electron transfer reaction [13].

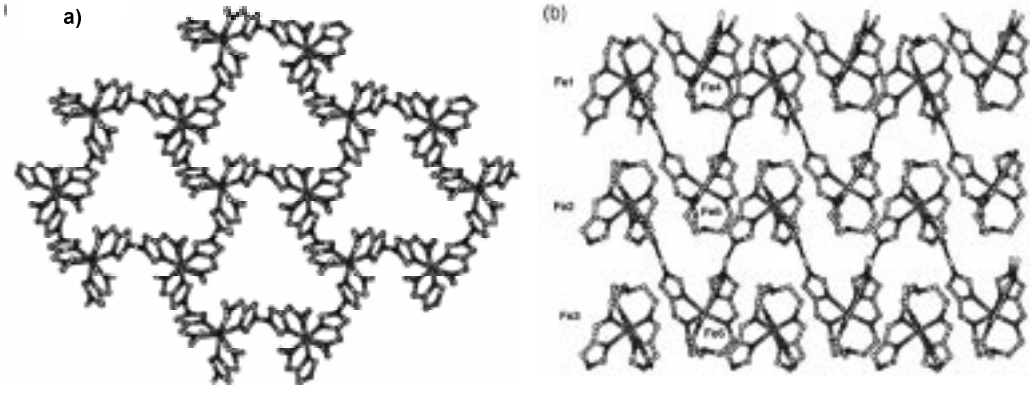

Fig. 4. The X-ray crystal structure of $[Fe^{II}(H_3L)][Fe^{III}(L)](BF_4)_2 \cdot 1.5H_2O$ (**3**) showing the homochiral 2D sheet structure formed by hydrogen bonds between $[Fe^{II}(H_3L)]^{2+}$ and $[Fe^{III}(L)]^{0}$. The counter ions and the water molecules have been omitted for clarity; a) a top view showing the sheet structure in which the same enantiomers are linked by intermolecular imidazole–imidazolate hydrogen bonds; b) a side view showing that there are three types of layers: the first layer consists of HS $Fe^{II}1$ and HS $Fe^{II}4$ complexes; the second layer consists of LS $Fe^{III}2$ and LS $Fe^{III}5$ complexes; and the third layer consists of HS $Fe^{III}3$ and HS $Fe^{II}6$ complexes. The HS $Fe^{II}1$ and LS $Fe^{III}5$, LS $Fe^{III}2$ and HS $Fe^{II}6$, and HS $Fe^{III}3$ and HS $Fe^{II}4$ complexes are connected by hydrogen bonds

The crystal structure was determined from single-crystal X-ray analysis at 293 K. The structure consists of three protonated $[Fe^{II}(H_3L)]^{2+}$ ions, three deprotonated $[Fe^{III}(L)]$ species, six BF_4^- counter anions, and four and a half water molecules of crystallization. The structures of the component complexes, $[Fe^{II}(H_3L)]^{2+}$ and $[Fe^{III}(L)]$, are similar to that of **1**. Adjacent $[Fe^{II}(H_3L)]^{2+}$ and $[Fe^{III}(L)]$ molecules are arrayed in an alternate fashion on a plane perpendicular to the molecular C_3 axis in an up-and-down arrangement to form an extended 2D puckered sheet structure with a hexanuclear unit (Fig. 4a). The two species are linked by imidazole–imidazolate hydrogen bonds. The intermolecular N···N hydrogen bond distances are in the range of 2.752(7) – 2.784(8) Å. The Fe–N distances of **3** reveal that all the iron ions of the $[Fe^{II}(H_3L)]^{2+}$ species (Fe1, Fe4, and Fe6) are HS Fe^{II}, and those of the $[Fe^{III}(L)]$ species (Fe2, Fe3, and Fe5) indicate that the iron ions at the Fe2 and Fe5 sites are LS Fe^{III}, while the iron ion at the Fe3 site is HS Fe^{III}. A side view of crystal structure of **3**

(Fig. 4b) reveals that there are three types of layers: the first layer consists of HS $Fe^{II}1$ and the HS $Fe^{II}4$ complexes, the second layer consists of LS $Fe^{III}2$ and LS $Fe^{III}5$ complexes, and the third layer consists of HS $Fe^{III}3$ and HS $Fe^{II}6$ complexes. Intermolecular hydrogen bonding connects the HS $Fe^{II}1$ and LS $Fe^{III}5$, HS $Fe^{II}6$ and LS $Fe^{III}2$, and HS $Fe^{II}4$ and HS $Fe^{III}3$ complexes. Each complex becomes chiral with either a Δ (clockwise) or Λ (anticlockwise) configuration due to the screw coordination arrangement of the achiral tripodal ligand around the Fe^{II} or Fe^{III} ion. The absolute configurations around the six iron atoms, Fe1–Fe6, are the same and **3** crystallizes in the acentric space group, *P*3. These facts indicate that spontaneous resolution takes place during the course of crystallization.

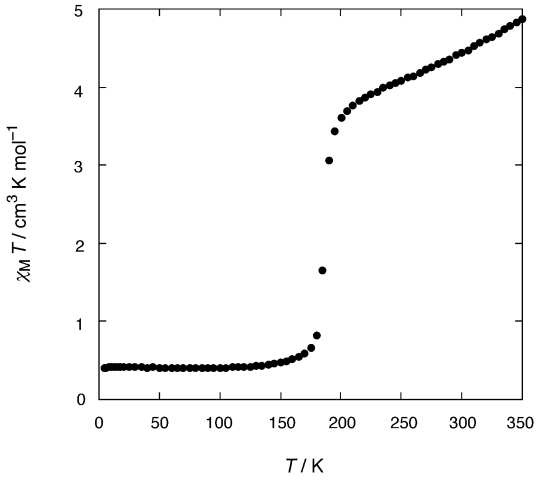

Fig. 5. A plot of $\chi_M T$ versus *T* for $[Fe^{II}(H_3L)][Fe^{III}(L)](BF_4)_2 \cdot 1.5H_2O$ (**3**)

The magnetic properties of **3** are represented in Fig. 5 in the form of a $\chi_M T$ versus *T* curve. In the temperature region of 2–150 K, $\chi_M T$ = 0.4 cm^3·K·mol^{-1}, and thus, in the range expected for LS states at both the Fe^{II} (*S* = 0) and Fe^{III} (*S* = 1/2) sites. The $\chi_M T$ value changes rather abruptly in the region of 170–200 K, indicating a spin transition at the Fe^{II} site. The value of $\chi_M T$ = 3.6 cm^3·K·mol^{-1} at 200 K, and is close to the calculated value for HS Fe^{II} (*S* = 2) and LS Fe^{III} states ($\chi_M T$ = 3.38 cm^3·K·mol^{-1}). Above 200 K, the value of $\chi_M T$ increases gradually due to the spin transition from LS to HS Fe^{III}. The value of $\chi_M T$ = 4.46 cm^3·K·mol^{-1} at 293 K is close to the calculated value ($\chi_M T$ = 4.71 cm^3·K·mol^{-1}) for HS Fe^{II} and a 2:1 mixture of LS and HS Fe^{III}, as determined by X-ray crystallography.

Mössbauer spectra were measured in the temperature range of 78–309 K. At 78 K, the Mössbauer spectrum consisted of two quadrupole-split doublets (LS Fe^{III}: δ = 0.19, ΔE_Q = 1.84, and LS Fe^{II}: δ = 0.42, ΔE_Q = 0.32 (mm·s^{-1})), demonstrating that both the Fe^{II} and the Fe^{III} sites were in the LS state. In the temperature range of 140–170 K, three doublets coexisted, because of the existence of LS and HS Fe^{II} sites

and LS Fe^{III} sites. The doublet arising from the LS Fe^{II} disappeared over 200 K. At 298 K, the absorption due to HS Fe^{III} was observed in addition to the absorptions of the HS Fe^{II} and LS Fe^{III}. Thus, the Mössbauer spectral results agree with the magnetic susceptibility results.

4. Conclusions

We have prepared $[Fe^{II}(H_3L)][Fe^{III}(L)](BF_4)_2 \cdot 1.5H_2O$ (**3**) with a supramolecular structure by a controlled deprotonation of $[Fe^{II}(H_3L)](BF_4)_2 \cdot 1.5H_2O$ (**2**) under aerobic conditions. In the supramolecular assembly of **3**, three independent properties are united: mixed-valence iron species, spin-crossover at the Fe^{II} and Fe^{III} sites, and the homochirality of the Fe^{II} and Fe^{III} building components. The magnetic properties of $[Fe^{II}(H_3L)](ClO_4)_2 \cdot 3H_2O$ (**1**) are quite different from those of the Fe^{II} species in **3**, demonstrating that the supramolecular association of the components into a mixed-valence material modifies their magnetic properties due to their co-operativity.

Acknowledgements

This work was supported by a Grant-in-Aid for Science Research (No. 14340209) from the Japanese Ministry of Education, Science, Sports, and Culture, from the Fund for Project Research from the Venture Business Laboratory of the Graduate School of Okayama University, and a JSPS Research Fellowship for Young Scientists (Y. S.).

References

[1] KAHN O., MARTINEZ C. J., Science, 279 (1998), 44.
[2] GÜTLICH P., HAUSER A., SPIERING H., Angew. Chem. Int. Ed. Engl., 33 (1994), 2024.
[3] HAYAMI S., GU Z.-Z., SHIRO M., EINAGA Y., SATO, O., J. Am. Chem. Soc., 122 (2000), 7126.
[4] VAN KONNINGSBRUGGEN P. J., GARCIA Y., KAHN O., FOURNES L., KOOIJMAN H., SPEK A. L., HAASNOOT J. G., MOSCOVICI J., PROVOST K., MICHALOWICZ A., RENZ F., GÜTLICH P., Inorg. Chem., 39 (2000), 1891.
[5] SORAI M., ENSLING J., HASSELBACH K. M., GÜTLICH, P., Chem. Phys., 20 (1977), 197.
[6] SUGIYARTO K. H., WEITZNER K., CRAIG D. C., GOODWIN H., Aust. J. Chem., 50 (1997), 869.
[7] ZHONG Z. J., TAO J.-Q., YU Z., DUN C.-Y., LIU Y.-J., YOU X.-Z., J. Chem. Soc., Dalton Trans, (1998), 327.
[8] LÉTARD J.-F. GUIONNEAU P., RABARDEL L., HOWARD J. A. K., GOETA A. E., CHASSEAU D., KAHN O., Inorg. Chem., 37 (1998), 4432.
[9] KATSUKI I., MOTODA Y., SUNATSUKI Y., MATSUMOTO N., NAKASHIMA T., KOJIMA M., J. Am. Chem. Soc., 124 (2002), 629.
[10] *Crystal Structure Analysis Package*, Rigaku and MSC (2001).
[11] BEATTIE, J. K., Adv. Inorg. Chem., 32 (1988), 1.
[12] BREUNING E., RUBEN M., LEHN J.-M., RENZ F., GARCIA Y., KSENOFONTOV V., GÜTLICH P., WEGELIUS E., RISSANEN K., Angew. Chem. Int. Ed. Engl., 39 (2000), 2504.
[13] SLATTERY S. J., BLAHO J. K., LEHNES J., GOLDSBY K. A., Coord. Chem. Rev., 174 (1998), 391.

Received 11 March 2003
Revised 26 March 2003

Materials Science, *Vol. 21*, *No. 2*, *2003*

Structural effects on magnetism of pyridyl nitroxide complexes of ruthenium(II, III) pivalate dimers*

M. HANDA[1*], Y. SAYAMA[2], M. MIKURIYA[2], I. HIROMITSU[1], AND K. KASUGA[1]

[1]Department of Material Science, Interdisciplinary Faculty of Science and Engineering, Shimane University, 1060 Nishikawatsu, Matsue 690-8504

[2]Department of Chemistry, School of Science and Technology, Kwansei Gakuin University, 2-1 Gakuen, Sanda 669-1337

The 1:1 reactions in molar ratio of ruthenium(II, III) pivalate dimer and pyridyl nitronyl nitroxide gave chain complexes, $[Ru_2(O_2CCMe_3)_4(L)]_n(BF_4)_n$, L = 2-(4-pyridyl)-4,4,5,5-tetramethyl-4,5-dihydro-1*H*-imidazolyl-1-oxyl-3-*N*–oxide and 2-(3-pyridyl)-4,4,5,5-tetramethyl-4,5-dihydro-1*H*-imidazolyl-1-oxyl-3-*N*-oxide. For the complex with the former radical, the chain structure made up by an alternated dimer-radical arrangement due to the axial co-ordination of pyridyl nitrogen and one of two nitroxide oxygens of the radical was confirmed by the X-ray diffraction method. Magnetic properties of the compounds were analyzed by considering magnetic interactions between Ru(II, III) dimer and radical through pyridyl and N–O groups, respectively.

Key words*: Ru(II, III) dimer; pyridyl niroxide radical; chain complexes*

1. Introduction

There has been much interest devoted to the metal complexes with nitroxide radicals because of their interesting magnetic properties based on the interaction between the paramagnetic metal centers and radicals [1–3]. We have been engaged in the magnetic study on ruthenium(II, III) pivalate dimers ($[Ru_2(O_2CCMe_3)_4]^+$) co-ordinated by the radicals; the Ru(II, III) dimeric cation has three unpaired electrons residing in its degenerated π^* and δ^* orbitals and has a large zero-field splitting ($D \sim 60$ cm^{-1}) [4, 5]. We have shown that the axial bond angle $\angle$Ru–O_{ax}–N (nitroxide) is the most important structural factor to affect their magnetic behaviours, the observed axial bond angles

* The paper was presented at the 13th Winter School on Coordination Chemistry, Karpacz, Poland, 9–13 December, 2002.

*Corresponding author, e-mail: handam@riko.shimane-u.ac.jp.

being in the range of 120–180° for the nitroxide Ru(II, III) complexes. The ferromagnetic interaction is operative between Ru(II, III) dimer and radical when the angle is decreased to be close to ∠Ru–O_{ax}–N = 120°. On the other hand, the antiferromagnetic interaction is operative when the angle ∠Ru–O_{ax}–N is close to 180° [6]. This result indicates that ferri- or ferromagnetic behaviour would be observed if the alternated chain structure of the Ru(II, III) dimer and the radical could be achieved in this combination [3]. However, the chain complex $[Ru_2(O_2CCMe_3)_4(nitph)]_n(BF_4)_n$ (**1**) (nitph = 2-phenyl-4,4,5,5-tetramethyl-4,5-dihydro-1*H*-imidazolyl-1-oxyl-3-*N*-oxide) revealed only a constant decrease of the magnetic moment until 3 K; neither ferri- nor ferromagnetic behaviour was observed. The temperature-dependent profile was concluded to be due to the fact that one of the two axial bond angles happened to be located at the angle giving no magnetic interaction through the axial bond [7, 8]. In spite of our efforts to obtain the alternated chain complex with various nitroxide radicals, the chain complex with niroxide oxygens at the both axial positions of Ru(II, III) dimers has not been obtained so far other than the complex **11**[6-10]. As an alternative way to produce such chain complexes, we selected the nitroxide radicals with a pyridyl group (2-(4-pyridyl)-4,4,5,5-tetramethyl-4,5-dihydro-1*H*-imidazolyl-1-oxyl-3-*N*-oxide (*p*-nitpy) and 2-(3-pyridyl)-4,4,5,5-tetramethyl-4,5-dihydro-1*H*-imidazolyl-1-oxyl-3-*N*-oxide (*m*-nitpy)), which may take part in the axial co-ordination to the Ru(II, III) dimer together with the N–O group. Here, we report the Ru(II, III) chain complexes obtained by the use of the nitroxide radicals with the pyridyl group. A preliminary report has been published for a complex with *p*-nitpy [11].

2. Experimental

Preparation. The tetrafluoroborate salt $[Ru_2(O_2CCMe_3)_4(H_2O)_2]BF_4$ was prepared according to the method described in the literature [12]. The nitronyl nitroxide radicals *p*-nitpy and *m*-nitpy were obtained according to the method described in the elsewhere [13, 14].

$[Ru_2(O_2CCMe_3)_4(p\text{-nitpy})]_n(BF_4)_n$ (2). 20 mg (0.027 mmol) of $[Ru_2(O_2CCMe_3)_4(H_2O)_2]BF_4$ was put into a Schlenk tube and heated at 80 °C under vacuum (0.005 mm Hg) for 30 min in order to remove the axial water molecules. During the treatment the tetrafluoroborate salt turned yellowish brown from orange. The CH_2Cl_2 solution (3 cm^3) of *p*-nitpy (6.4 mg (0.027 mmol)) was subsequently added into the tube and stirred with the water-removed tetrafluoroborate salt under argon. Hexane (14 cm^3) was slowly added into the reacted solution; the resulting solution was allowed to stand for several days at room temperature to deposit dark-green crystals, which were collected by filtration and washed with hexane. The yield was 18 mg (72%). Anal. found C, 41.50; H, 5.64; N, 4.56. Calcd. for $C_{32}H_{52}BF_4N_3O_{10}Ru_2$: C, 41.43; H, 5.65; N, 4.53. IR (in KBr) ν(NO) 1361, ν(COO) 1484, 1452, 1418, ν(BF_4^-) 1057 cm^{-1}. Diffuse reflectance spectrum: λ_{max} 290 (sh), 380, 607, 1027 (br) nm.

$[Ru_2(O_2CCMe_3)_4(m\text{-nitpy})]_n(BF_4)_n \cdot nH_2O$ (3). This compound was obtained as dark-green crystals by the reaction of $[Ru_2(O_2CCMe_3)_4(H_2O)_2]BF_4$ (20 mg, 0.027 mmol) with *m*-nitpy (6.7 mg, 0.029 mmol) in CH_2Cl_2/hexane using the same method as that of **2**. The yield was 20 mg (78% based on $[Ru_2(O_2CCMe_3)_4(H_2O)_2]BF_4$). Anal. found C, 40.79; H, 5.49; N, 4.37. Calcd. for $C_{32}H_{54}BF_4N_3O_{11}Ru_2$: C, 40.64; H, 5.76; N, 4.44. IR (in KBr) ν(NO) 1363, ν(COO) 1483, 1452, 1418, ν(BF_4^-) 1056 cm^{-1}. Diffuse reflectance spectrum: λ_{max} 266, 367, 577, 621, 673, 1016 (br) nm.

Measurements. Elemental analyses for carbon, hydrogen, and nitrogen were carried out using Perkin-Elmer Series II, CHN/O Analyzer. Infrared spectra (KBr pellets) and electronic spectra were measured with JASCO IR-700 and Shimadzu UV-3100 spectrometers, respectively. Temperature dependences of the magnetic susceptibilities were measured on a Quantum Design MPMS-5S SQUID susceptometer operating at a magnetic field of 0.5 T between 2 and 300 K. The susceptibilities were corrected for diamagnetism of constituent atoms using Pascal′s constant [3]. The effective magnetic moments were calculated from the equation $\mu_{eff} = 2.828(\chi T)^{1/2}$, where χ is the magnetic susceptibility per Ru(II, III)-radical unit. The X-Ray Diffraction data for $\mathbf{2}\cdot 1.5n CH_2Cl_2$ were collected on an Enraf-Nonius CAD4 diffractometer using graphite-monochromated Mo K_α radiation at (25±1) °C. The crystal structure was solved by direct methods and refined by full-matrix least-squares. Non-hydrogen atoms were refined with anisotropic thermal parameters. The hydrogen atoms were inserted at their calculated positions and fixed there. The calculations were carried out on a VAX station 4000 90A computer using a MolEN program package [15]. Crystallographic data for $\mathbf{2}\cdot 1.5n CH_2Cl_2$: $C_{33.5}H_{55}Cl_3BF_4N_3O_{10}Ru_2$, F.W. = 1055.32, monoclinic, space group $P2_1/c$, a = 11.421(3), b = 17.424(3), c = 26.358(8) Å, β = 98.75(1)°, V = 5184(2) $Å^3$, Z = 4, D_m =1.40, D_c = 1.35 g cm^{-3}, μ(Mo K_α) = 7.85 cm^{-1}, $F(000)$ = 2148, crystal dimensions 0.40×0.39×0.32 mm, 8932 reflections collected ($2\theta_{max}$ = 49°), 4973 independent reflections, R [$I \geq 3\sigma(I)$] = $\Sigma||F_o| - |F_c||/\Sigma|F_o|$ = 0.061, R_w [$I \geq 3\sigma(I)$] = $[\Sigma w(|F_o| - |F_c|)^2/\Sigma|F_o|^2]^{1/2}$ = 0.079 ($w = 1/[\sigma^2(|F_o|)+(0.02|F_o|)^2 + 1.0]$).

3. Results and discussion

The crystal structure of $\mathbf{2}\cdot 1.5n CH_2Cl_2$ is shown in Fig. 1. Selected bond distances and angles are listed in Table 1. The zigzag chain with alternated arrangement of the Ru(II, III) dimer and the radical is extended along the *b* axis. The Ru1–Ru2 bond distance is 2.272(1) Å, which is in the range of those of the other $[Ru_2(O_2CR)_4]^+$ compounds (2.24–2.30 Å) [4, 5]. One of the axial sites of the Ru(II, III) dimer is occupied by the pyridyl nitrogen of *p*-nitpy with a separation of Ru2–N3" = 2.260(9) Å, which is comparable to those of bis-adduct Ru(II, III) dimers with *m*- and *p*-nitpy (2.269(3) Å for $[Ru_2(O_2CCMe_3)_4(m\text{-nitpy})_2]BF_4$ and 2.282(6) Å for $[Ru_2(O_2CCMe_3)_4(p\text{-nitpy})_2]BPh_4$) [16]. One of the two N–O groups is co-ordinated with a distance of

Ru1–O9 = 2.286(7) Å. The nitroxide oxygen O10 stays free from any co-ordination. The N–O bond distances 1.30(1) (for N1–O9) and 1.27(1) Å (for N2–O10) imply that the *p*-nitpy ligand exists as a genuine radical [1]. The axial bond angle Ru1–O9–N1 = 125.3(6)° is in the range for giving ferromagnetic interaction between the Ru(II, III) dimer core and the radical (*vide infra*).

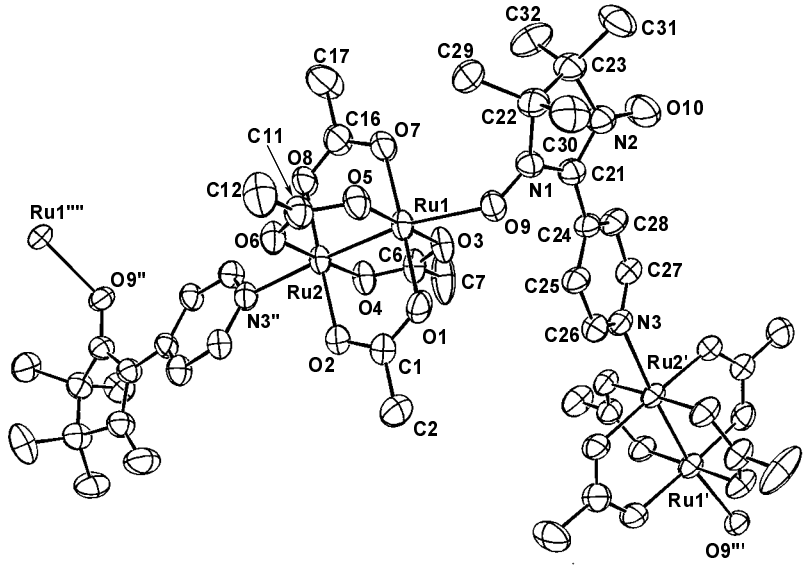

Fig. 1. View of the structure of $[Ru_2(O_2CCMe_3)_4(p\text{-nitpy})]_n(BF_4)_n \cdot 1.5nCH_2Cl_2$ (**2**·$1.5nCH_2Cl_2$), showing the atom-labelling scheme. Thermal ellipsoids are at the 35% probability level. Methyl groups of pivalic acid moieties, BF_4 ions, and CH_2Cl_2 molecules are omitted for clarity. Primes and double primes refer to the equivalent positions (x, ½ – y, ½ + z) and (x, ½ – y, –1/2+z), respectively

Table 1. Selected bond distances (Å) and angles (°) of **2**·$1.5nCH_2Cl_2$ with their estimated standard deviations (in parentheses)

Bond	Value	Bond	Value
Ru1–Ru2	2.272(1)	Ru2–O6	2.008(7)
Ru1–O1	2.004(7)	Ru2–O8	2.020(7)
Ru1–O3	2.005(7)	Ru2–N3"[1]	2.260(9)
Ru1–O5	2.006(7)	N1–O9	1.30(1)
Ru1–O7	2.015(7)	N2–O10	1.27(1)
Ru1–O9	2.286(7)	Ru2–Ru1–O9	169.5(2)
Ru2–O2	2.015(7)	Ru1–Ru2–N3"[1]	175.7(2)
Ru2–O4	2.020(7)	Ru1–O9–N1	125.3(6)

[1]Double prime refers to the equivalent position (x, ½ – y, –1/2 + z).

Temperature dependences of magnetic moments for **2** and **3** are displayed in Figs. 2 and 3, respectively. Although the magnetic moments at a room temperature (300 K) are similar (4.89μ_B for **2** and 4.75μ_B for **3**), their temperature-dependent profiles are quite different. The moment of **2** increases upon lowering the temperature down to 8 K and then rapidly decreases from the maximum value of 5.70μ_B (at 8 K) to reach the value of 3.89μ_B (at 2 K). On the other hand, the moment of **3** is nearly constant down to 100 K, and then falls to the value of 2.83μ_B (at 2 K).

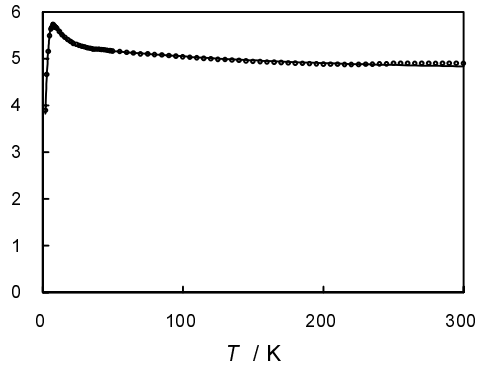

Fig. 2. Temperature dependence of effective magnetic moment (μ_{eff}/μ_B) of **2**. The solid line was calculated with the parameters listed in Table 2

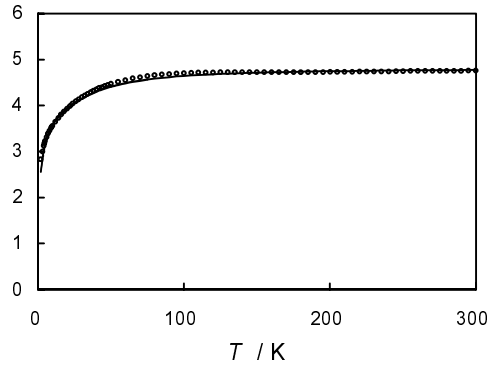

Fig. 3. Temperature dependence of effective magnetic moment (μ_{eff}/μ_B) of **3**. The solid line was calculated with the parameters listed in Table 2

Their magnetic behaviours were analyzed by taking two magnetic interactions between the Ru(II, III) dimer and the radical (Scheme 1) into account; one is through the axial N–O group and the other through the pyridyl group. The magnetic simulations of the behaviours were made using the parameters J and J' (in Scheme 1) together with the parameters g_M (g factor for Ru(II, III) dimer), g_R (g factor for radical), and D (zero-field splitting for Ru(II, III) dimer), where J' was considered to be substantially smaller in its absolute value than J and was evaluated based on the molecular–field approximation [3].

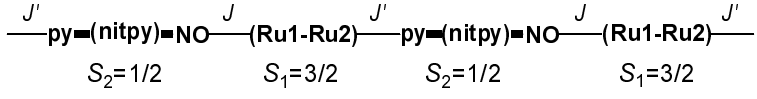

Scheme 1

The results are summarized in Table 2. The ferromagnetic interaction through the co-ordinated N–O group (J = 20 cm^{-1}) in **2** is reasonably explained by considering the axial bond angle (∠Ru1–O9–N1 = 125.3(6)°), which is located at the smaller end for those of the nitroxide Ru(II, III) complexes prepared by our research groups [6–11, 16, 17]; the interaction is ferromagnetic when the axial bond angle is decreased to be

close to 120°, though the interaction is antiferromagnetic when the angle is increased to be close to 180°. The complex **3** might have a larger axial bond angle compared with that of **2** because its ferromagnetic interaction (J = 0.3 cm^{-1}) is much weaker than that for **2**. The interactions through the pyridyl group are weak for both the present complexes like the cases of bis-addcut complexes $[Ru_2(O_2CCMe_3)_4(m\text{-nitpy})_2]X$ and $[Ru_2(O_2CCMe_3)_4(p\text{-nitpy})_2]X$ (X = BF_4 and BPh_4) [16], in which the interactions of Ru(II, III) dimer with *p*-nitpy are weakly ferromagnetic (J' = 0.8 and 1.4 cm^{-1}) and those with *m*-nitpy are weakly antiferromagnetic (J' = –1.0 cm^{-1}). The complex **2** has a ferromagnetic interaction through the pyridyl group of *p*-nitpy (J' = 0.45 cm^{-1}) as well as that through the N–O group (J = 20 cm^{-1}), which may be related to the relatively steep increase in the moment when the temperature goes down near its maximum temperature (8 K) (Fig. 2).

Table 2. Fitting parameters for the magnetic data

Parameter	Compound	
	2	**3**
g_M	2.23	2.32
g_R	2.00	2.00
D/cm^{-1}	50	40
J/cm^{-1}	20	0.3
J'^{*}/cm^{-1}	0.45	–0.4
$R/10^{-3}$**	0.66	10.8

*Estimated by molecular field approximation.

**$R = \Sigma(\chi_{obsd} - \chi_{calcd})^2/\Sigma(\chi_{obsd})^2$, where χ is the magnetic susceptibility per Ru(II, III)-radical unit.

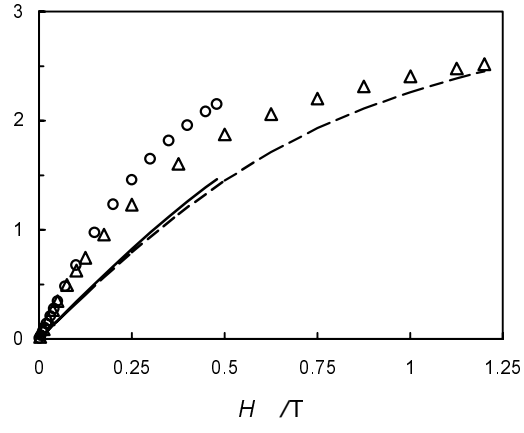

Fig. 4. Field (H/T) dependence of the magnetization ($M/N\mu_B$) for $[Ru_2(O_2CCMe_3)_4(p\text{-nitpy})]_n(BF_4)_n$ (**2**) at 4.0 K (Δ) and 10 K(O). Theoretical curves at 4.0 K (----) and 10 K (–) (g_M = 2.23, g_R = 2.00, and D = 50 cm^{-1})

The ferromagnetic behaviour of **2** was confirmed by measuring the magnetization of **2** versus the applied field (Fig. 4). The magnetization curve of **2** lies above the curve of the Brillouin function for the system of $S_1 = 3/2$ (for Ru(II, III) dimer) and $S_2 = 1/2$ (for *p*-nitpy) under the consideration of zero-field splitting. The rapid decrease in the moment below 8 K is considered to come from the zero-field splitting ($D = 40$ cm^{-1}) within the Ru(II, III) dimer (Fig. 2). The complex **3** has an antiferromagnetic interaction through the pyridyl group of *m*-nitpy ($J' = -0.4$ cm^{-1}). Both the interactions estimated with $J = 0.3$ cm^{-1} and $J' = -0.4$ cm^{-1} are weak, hence it may not be appropriate to estimate the J' value using the molecular-field approximation. However, it is certain that **3** has the ferro- and antiferromagnetic interactions although the antiferromagnetic interaction is slightly predominant because **3** does not show any ferrimagnetic behaviour, which should occur if both the interactions are antiferromagnetic in a similar magnitude [3]. The assignment of the antiferromagnetic interaction $J' = -0.4$ cm^{-1} is in accordance with the previous results for $[Ru_2(O_2CCMe_3)_4(m\text{-nitpy})_2]X$ (X = BF_4 and BPh_4), which have a weak magnetic interaction through the pyridyl group ($J' = -1.0$ cm^{-1}) [16].

4. Conclusions

The magnetic investigation on chain complexes with an alternated arrangement of ruthenium(II, III) pivalate dimers and pyridyl nitroxide radicals, 2-(4-pyridyl)-4,4,5,5-tetramethyl-4,5-dihydro-1*H*-imidazolyl-1-oxyl-3-*N*–oxide (*p*-nitpy) and 2-(3-pyridyl)-4,4,5,5-tetramethyl-4,5-dihydro-1*H*-imidazolyl-1-oxyl-3-*N*-oxide (*m*-nitpy), was performed. It was found that the pyridyl group on the radical weakly mediates a ferro- or antiferromagnetic interaction with Ru(II, III) dimer depending on the employed radicals; *p*-nitpy gives the ferromagnetic interaction, but *m*-nitpy gives the antiferomagnetic interaction. The observed ferromagnetic interaction through the axially co-ordinated N–O group for the chain complex with *p*-nitpy (complex **2**) is concluded to be associated with the fact that the axial bond angle is located at ca. 120°.

Acknowledgement

The present work was partially supported by Grants-in-Aid for Scientific Research No. 14540516 from the Ministry of Education, Culture, Sports, Science and Technology.

References

[1] CANESCHI A., GATTESCHI D., REY P., Prog. Inorg. Chem., 39 (1991), 331.
[2] BENELLI C., GATTESCHI D., Chem. Rev., 102 (2002), 2369.
[3] KAHN O., *Molecular Magnetism*, VCH Publishers, New York, 1993.
[4] COTTON F.A. WALTON R.A., *Multiple Bonds between Metal Atoms*, 2nd Ed., Oxford University Press, New York, 1993, pp. 399–430.
[5] AQUINO M.A.S., Coord. Chem. Rev., 170 (1998), 141.

[6] SAYAMA Y., HANDA M., MIKURIYA M., HIROMITSU I., KASUGA K., Bull. Chem. Soc. Jpn., 76 (2003), 769.
[7] HANDA M., SAYAMA Y., MIKURIYA M., NUKADA R., HIROMITSU I., KASUGA K., Chem. Lett. (1996), 201.
[8] HANDA M., SAYAMA Y., MIKURIYA M., NUKADA R., HIROMITSU I., KASUGA K., Bull. Chem. Soc. Jpn., 71 (1998), 119.
[9] SAYAMA Y., HANDA M., MIKURIYA M., HIROMITSU I., KASUGA K., Chem. Lett. (1999), 453.
[10] SAYAMA Y., HANDA M., MIKURIYA M., HIROMITSU I., KASUGA K., Bull. Chem. Soc. Jpn., 74 (2001), 2129.
[11] SAYAMA Y., HANDA M., MIKURIYA M., HIROMITSU I., KASUGA K., Chem. Lett. (1998), 777.
[12] BARRAL M.C., JIMÉNEZ-APARICIO R., PRIEGO J.L., ROYER E.C., GUTIÉNEZ-PUEBLA E., RUIZ-VALERO C., Polyhedron, 11 (1992), 2209.
[13] ULLMAN E. F., GALL L., OSIECKI J. H., J. Org. Chem., 35 (1970), 3623.
[14] DAVIS M. S., MOROKUMA K., KREILICK R.W., J. Am. Chem. Soc., 94 (1972), 5588.
[15] FAIR C. K., *Mol EN Structure Determination System*, Delft Instrument, Delft, 1990.
[16] SAYAMA Y., HANDA M., MIKURIYA M., HIROMITSU I., KASUGA K., Bull. Chem. Soc. Jpn., 73 (2000), 2499.
[17] HANDA M., SAYAMA Y., MIKURIYA M., NUKADA R., HIROMITSU I., KASUGA K., Bull. Chem. Soc. Jpn., 68 (1995), 1647.

Received 24 March 2003
Revised 4 April 2003

Materials Science, *Vol. 21*, *No. 2*, *2003*

Intramolecular electron transfer on the vibrational timescale in mixed valence ruthenium clusters*

NAOYUKI IMAI, TOMOHIKO HAMAGUCHI, TADASHI YAMAGUCHI, AND TASUKU ITO**

Department of Chemistry, Graduate School of Science, Tohoku University, Sendai 980-8578, Japan

The thermodynamic stability of the mixed valence (one electron reduced) state between linked Ru_3 units was studied by means of electrochemical methods for the series of the ligand-bridged triruthenium cluster dimer, $[Ru_3(\mu_3\text{-}O)(\mu\text{-}CH_3CO_2)_6(CO)(L)(\mu\text{-}BL)Ru_3(\mu_3\text{-}O)(\mu\text{-}CH_3CO_2)_6(CO)(L)]$ (BL = 1,4-pyrazine: L = 4-dimethylaminopyridine (dmap) (**1a**), pyridine (py) (**1b**), 4-cyanopyridine (cpy) (**1c**), 1-azabicyclo[2.2.2]octane (**1d**); BL = 4,4′-bipyridine: L = dmap (**2a**), py (**2b**), cpy (**2c**); BL = 2,7-diazapyrene: L = dmap (**3a**); BL = 1,4-diazabicyclo[2.2.2]octane: L = dmap (**4a**), py (**4b**), cpy (**4c**)). The mixed valence states undergoing rapid intramolecular electron transfers were observed by IR spectro-electrochemistry. By simulating dynamical effects on the observed ν(CO) absorption bandshapes, the rate constants k_e for electron transfer in the mixed valence states of **1a**, **1b**, **1c** and **1d** were estimated to be 9×10^{11} s^{-1} (at room temperature (rt)), 5×10^{11} s^{-1} (at rt), *c.a.* 1×10^{11} s^{-1} (at rt), and 1×10^{12} s^{-1} (at –18 °C), respectively. Possible applications of this approach to asymmetric mixed valence systems were discusssed.

1. Introduction

Spectroscopic techniques for determination of molecular structure have their own timescales. As is well known, spectral coalescence in nuclear magnetic resonance (NMR) is on the order of milliseconds. In infrared (IR) spectroscopy, the timescale is on the order of picoseconds. Intramolecular processes such as electron and energy transfer can occur on the picosecond timescale. We recently reported our observations of coalescence of the C–O stretching bands of carbon monoxide (ν(CO)) ligands in the most rapidly exchanging mixed valence complexes of hexanuclear ruthenium clusters [1–3]. The mixed valence complexes are one-electron reduced species of ligand bridged dimers of triruthenium clusters of the $[Ru_3(\mu_3\text{-}O)(\mu\text{-}CH_3CO_2)_6(CO)(L)(\mu\text{-}BL)Ru_3(\mu_3\text{-}O)(\mu\text{-}CH_3CO_2)_6(CO)(L)]$ type, shown in Fig. 1, where BL denotes

* The paper was presented at the 13th Winter School on Coordination Chemistry, Karpacz, Poland, 9–13 December, 2002.

** Corresponding author, e-mail: ito@agnus.chem.tohoku.ac.jp.

bridging ligand. In the neutral isolated states of all the compounds, each trinuclear Ru_3 unit formally contains one Ru(II) and two Ru(III) centres and the carbonyl ligand is co-ordinated to the formally divalent centre. We describe the characteristics of the IR spectra of **1a–1d** and **2a–2b** along with electrochemical data of all the compounds shown in Fig. 1 [4]. Possible applications of infrared spectroelectrochemistry for the estimation of the rate constants of intramolecular electron transfer in asymmetric mixed valence system will also be discussed.

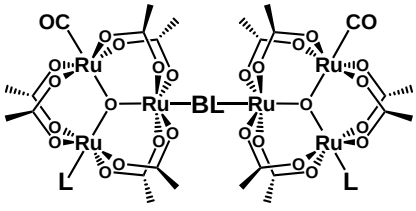

BL \ L	(dmap)	(py)	(cpy)	(abco)
(pz)	**1a**	**1b**	**1c**	**1d**
(bpy)	**2a**	**2b**	**2c**	—
(dap)	**3a**	—	—	—
(dabco)	**4a**	**4b**	**4c**	—

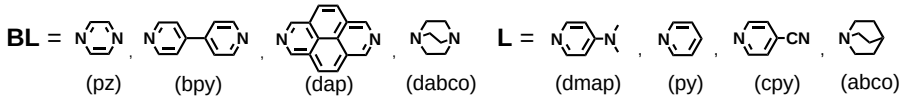

Fig. 1. Structure of $[Ru_3(\mu_3\text{-}O)(\mu\text{-}CH_3CO_2)_6(CO)(L)(\mu\text{-}BL)Ru_3(\mu_3\text{-}O)(\mu\text{-}CH_3CO_2)_6(CO)(L)]$ and numbering of the compounds: pz – 1,4-pyrazine, bpy – 4,4′-bipyridine, dap – 2,7-diazapyrene, dabco – 1,4-diazabicyclo[2.2.2]octane, abco – 1-azabicyclo-[2.2.2]octane

2. Electrochemically generated mixed valence states and their thermodynamic stabilities

Figure 2 shows cyclic voltammograms (CV) of a series of Ru_3 dimers where the bridging ligand is fixed to pyrazine and the terminal ligands are varied. Figure 3 shows CV's of a series of Ru_3 dimers where the bridging ligand is varied and the terminal ligand is fixed to dmap. In all the CV's in Figs. 2 and 3, two-electron oxidation waves are observed at approximately $E_{1/2}(2/0) = 0.50$ and $E_{1/2}(4/2) = 1.3$ V vs. SSCE. Here, the overall charges of the complexes are expressed in parentheses. On the other hand, each compound generally displays two single electron reduction waves that correspond formally to $Ru_3^{III,III,II}$-BL-$Ru_3^{III,III,II}$/$Ru_3^{III,III,II}$-BL-$Ru_3^{III,II,II}$ (0/–1) and then $Ru_3^{III,III,II}$-BL-$Ru_3^{III,II,II}$/$Ru_3^{III,II,II}$-BL-$Ru_3^{III,II,II}$ (–1/–2). In the case of **4a**, the splitting between the (0/–1) and (–1/–2) states is too small ($\Delta E \approx 0$ mV) to resolve by cyclic voltammetry. One important contribution to the magnitude of the splitting between the single electron (0/–1) and (–1/–2) reduction waves, ΔE, is the stabilization energy imparted to the –1 state by electron delocalization. Comproportionation constants, $K_c = \exp(\Delta EF/RT)$, estimated from ΔE are also given in Figs. 2 and 3. The mixed valence species, i.e., the –1 state exists in the region of ΔE between the (0/–1) and (–1/–2) waves and the magnitude of ΔE, and thereby K_c, reflects stability of the mixed valence state. Redox potential data for the (0/–1) and (–1/–2) processes are summarized in Table 1.

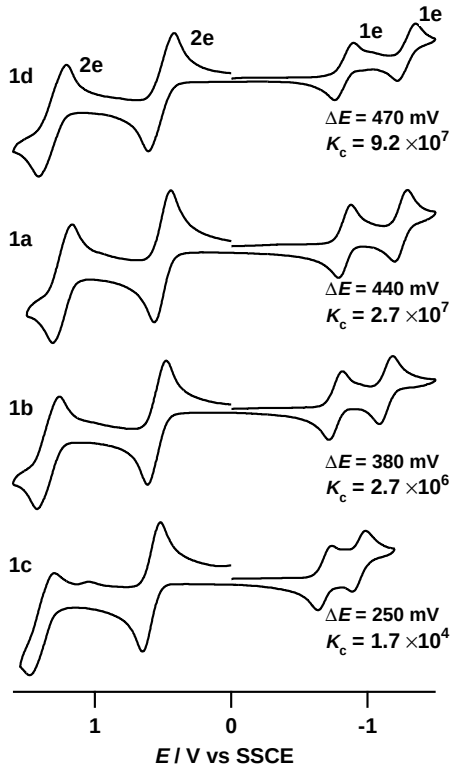

Fig. 2. Cyclic voltammograms, ΔE, and K_c of $[\{Ru_3(\mu_3\text{-}O)(\mu\text{-}CH_3CO_2)_6(CO)(L)\}_2(\mu\text{-}pz)]$ (L = abco (**1d**), dmap (**1a**), py (**1b**), cpy (**1c**))

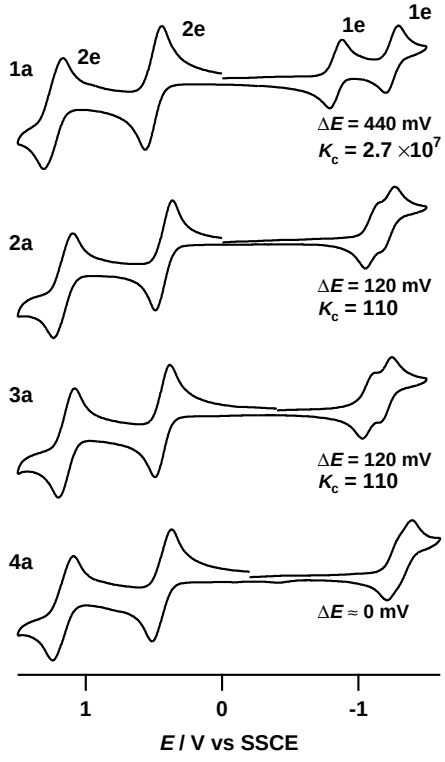

Fig. 3. Cyclic voltammograms, ΔE, and K_c of $[\{Ru_3(\mu_3\text{-}O)(\mu\text{-}CH_3CO_2)_6(CO)(dmap)\}_2(\mu\text{-}BL)]$ (BL = pz (**1a**), bpy (**2a**), dap (**3a**), dabco (**4a**))

Table 1. Electrochemical data for $[\{Ru_3(\mu_3\text{-}O)(\mu\text{-}CH_3CO_2)_6(CO)(L)\}_2(\mu\text{-}BL)]$

Compound	BL	L	$E_{1/2}(0/-1)$[a], V	$E_{1/2}(-1/-2)$[a], V	ΔE (mV)	K_C
1a	pz	dmap	–0.89	–1.33	440	2.7×10^7
1b	pz	py	–0.81	–1.19	380	2.7×10^6
1c	pz	cpy	–0.68	–0.93	250	1.7×10^4
1d	pz	abco	–0.84	–1.31	470	9.2×10^7
2a	bpy	dmap	–1.11	–1.23	120	1.1×10^2
2b	bpy	py	–1.03	–1.11	80	2.3×10^1
2c	bpy	cpy		–0.91(2e)	≈0	<10
3a	dap	dmap	–1.08	–1.20	120	1.1×10^2
4a	dabco	dmap	–1.25	–1.31	60	3×10^1
4b	dabco	py	–1.12	–1.17	50	7×10^0
4c	dabco	cpy		–0.94(2e)	≈0	<10

[a]Cyclic voltammograms recorded in 0.1 M tetra-*n*-butylammonium hexafluorophosphate in dichloromethane, V versus saturated sodium chloride calomel electrode (SSCE).

An interesting aspect of these complexes is that the splitting ΔE depends strongly on the ancillary ligands (dmap, py, cpy, abco) and on the bridging ligands (pz, bpy, dap, dabco). Thus, as the adjustable pyridyl ligand in the series **1a–1c** and **2a–2c** is changed from dmap in **1a** and **2a** to an unsubstituted pyridine for **1b** and **2b** to an electron withdrawing cpy for **1c** and **2c**, the values of ΔE and K_c decrease considerably (Table 1). Compound **1d** with abco, which has the largest pK_a of 11.1 among the present series of terminal ligands, possesses the largest ΔE and K_c [4]. The bridging ligand π-electron systems mediate electronic coupling between the two Ru_3 centres, and the overlap between the Ru_3 cluster dπ-electron system and the bridging ligand π^* system appears to be very favourable. In fact, the dabco bridged compound **4a**, which has no π-electron system in the bridging ligand, shows essentially no electronic coupling ($\Delta E \approx 0$). The relevant Ru d level is closer to the pz π^* level in **1a** than it is in **1c**, and closer to the bpy π^* level in **2a** than it is in **2c**. This description of the electronic structure is supported by experimental evidence [2]. In general, electronic coupling falls off exponentially with increasing distance between electronically interacting centres. The centre-to-centre separation between Ru_3O units in the crystal structure of **1a** is 10.9 Å [5], and it is estimated at ca. 15.3 Å in bpy bridged complexes. The longer separation between Ru_3 centres in **2a–2c** and **3a** decreases the intercluster electronic coupling, thereby decreasing ΔE values.

3. IR Spectra of the mixed-valence species in the ν(CO) region

The vibrational spectra of complexes **1a–1d** and **2a–2c** were obtained by using reflectance IR spectroelectrochemistry (SEC). Controlled potentials were applied to prepare the singly (–1) and doubly (–2) reduced states of cluster for IR spectroscopic observation. Measurements were carried out at room temperature unless otherwise stated. Experiments on **1d** were carried out at –18 °C, because reduced species (the –1 and –2 states) of this compound were unstable at room temperature. Figures 4a and b show the IR spectra in the ν(CO) region of pyrazine (**1a–1d**) and 4,4′-bipyridine (**2a–2b**) bridged complexes. Let us discuss first the pyrazine bridged systems. In the isolated (0) state, **1d** exhibits a single ν(CO) band at 1937 cm^{-1} (Fig. 4a top), indicating that two Ru_3 units in **1d** are pairwise equivalent. The doubly reduced species also gives rise to a single ν(CO) band, but at 1890 cm^{-1}, reflecting identical redox states at each $Ru_3^{III,II,II}$ cluster. Complexes **1a–1c** similarly exhibit single ν(CO) bands in the neutral state and –2 state, respectively. Interestingly, however, the single-electron reduced state of **1d** shows a broad absorption band at the average energy of the bands observed for the neutral (0) and doubly reduced (–2) states of **1d** (Fig. 4a top). The degree of 'coalescence' of the IR spectra depends on the degree of electronic coupling between the pyrazine-linked Ru_3 clusters (Fig. 4a). As ΔE (or K_c) decreases from 470 mV (9.2×10^7) for **1d** to 250 mV (1.7×10^4) for **1c**, two distinct ν(CO) bands at 1931 cm^{-1} and 1904 cm^{-1} become resolved for **1c**. Cluster **1b** with an intermediate

value of ΔE (K_c) of 380 mV (2.7×10^6) shows an intermediate degree of spectral 'coalescence' in the singly reduced state.

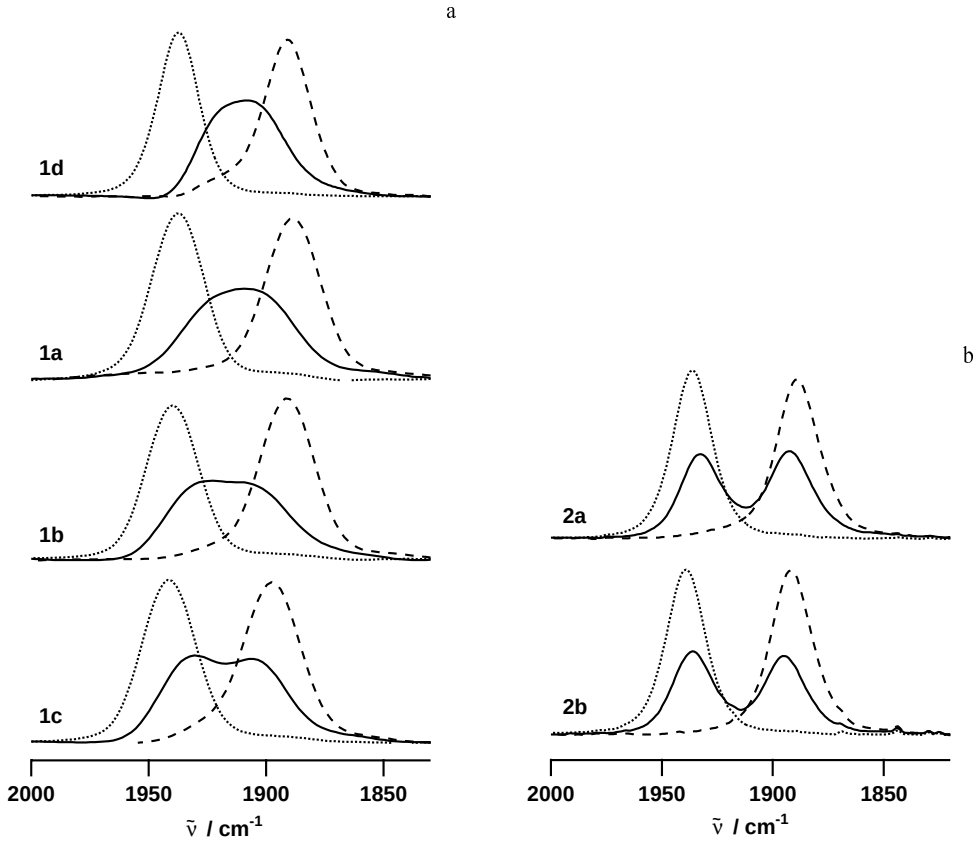

Fig. 4. IR spectra in the ν(CO) region for: a) $[\{Ru_3(\mu_3\text{-}O)(\mu\text{-}CH_3CO_2)_6(CO)(L)\}_2(\mu\text{-}pz)]^{n+}$ (n = 0 (···), -1 (—), –2 (- - -)) for L = abco (**1d**), dmap (**1a**), py (**1b**), cpy (**1c**); b) $[\{Ru_3(\mu_3\text{-}O)(\mu\text{-}CH_3CO_2)_6(CO)(L)\}_2(\mu\text{-}bpy)]^{n+}$ (n = 0 (···), –1 (—), –2 (- - -)) for L = dmap (**2a**), py (**2b**)

Similarly, both the neutral and –2 states of the bpy bridged complexes **2a–2c** exhibit one sharp ν(CO) band in the IR (Fig. 4b). The spectra of the –1 states of **2a** and **2b** consist of two well-resolved and well-separated ν(CO) bands, perturbed only slightly relative to the spectra of the neutral and –2 states. For **2c**, a reliable spectrum of the –1 state could not be obtained due to < 50 mV separation between the (0/–1) and (–1/–2) CV waves. In clusters **2a–2c**, the electronic coupling is small as evidenced by cyclic voltammetry. Overall, the singly reduced states of **2a–2c** can be viewed as valence trapped or localized compounds.

The IR spectral feature in the ν(CO) region of the –1 mixed valence state is very different between pyrazine bridged complexes **1a–1d** and 4,4′-bipyridine complexes

2a–2c. The vast difference in spectral characteristics arises from the electronic interactions between two Ru_3 units through the bridging ligand, as is seen in their electrochemical behaviour. The use of longer bpy bridges in **2a–2c** attenuates the electronic coupling to the point that in **2c** the –1 charge transfer state is no longer defined. Preliminary experiments show essentially no temperature dependence of the IR spectra in the range from room temperature down to –40 °C.

4. Estimation of rate constants of intramolecular electron transfer in the mixed valence state

At the present time, we have no evidence of a process other than intramolecular electron transfer to account for the changes observed in the IR spectral line shapes of our systems. We carried out the Bloch equation type analysis for the IR line broadening which is developed by McClung [6].

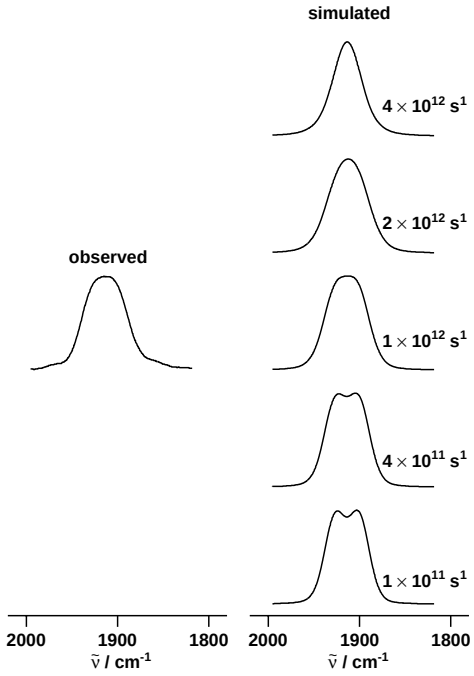

Fig. 5. Comparison of observed to simulated infrared spectra in the ν(CO) region for $\mathbf{1a}^-$ as a function of the intramolecular electron transfer rate constant k_e

Figure 5 shows an example of the simulated spectral line shapes as a function of the rate constant k_e and a comparison to the observed spectrum of $\mathbf{1a}^-$. Similar analyses were carried out for $\mathbf{1a}^-$–$\mathbf{1c}^-$ and $\mathbf{2a}^-$ [2]. The rate constants k_e of electron transfer

estimated by this type of simulation for **1d**$^-$, **1a**$^-$, **1b**$^-$, and **1c**$^-$ are $(10\pm2)\times10^{11}$ at −18 °C, $(9\pm3)\times10^{11}$, $(5\pm3)\times10^{11}$, ca. 1×10^{11} s^{-1}, respectively. Simulated spectra as a function of k_e for **1c**$^-$ show that k_e for **1c**$^-$ is close to the lower limit that can be determined reliably by this approach [2].

5. Possible applications of IR SEC for the estimation of the rate constants of intramolecular electron transfer in asymmetric mixed valence state

Using different terminal ligands at the L^1 and L^2 sites, we can prepare a series of asymmettric Ru_3 dimers **1e–1g** (Fig. 6). They show CV similar to the symmetric Ru_3 dimers **1a–1d**, giving redox wave splitting ΔE (410, 310, and 350 mV for **1e**, **1f**, and **1g**, respectively). The mixed valent −1 states of **1e–1g** also show similar intervalence transition band (at 11,500; 10,500; and 10400 cm^{-1}, for **1e**, **1f**, and **1g**, respectively). These observations strongly suggest a possible application of the above-mentioned technique to asymmetric mixed valence systems.

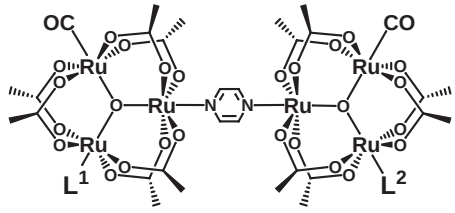

	L^1	L^2
1e	dmap	py
1f	py	cpy
1g	dmap	cpy

Fig. 6. Structure of asymmetric dimer[$Ru_3(\mu_3\text{-}O)(\mu\text{-}CH_3CO_2)_6(CO)(L^1)(\mu\text{-}pz)Ru_3(\mu_3\text{-}O)(\mu\text{-}CH_3CO_2)_6(CO)(L^2)$] and numbering of the compounds.

In contrast to the symmetric system, however, intramolecular electron transfer in the asymmetric system is somewhat complicated. A comparison of potential energy surface for symmetric and asymmetric mixed valence system is shown in Fig. 7.

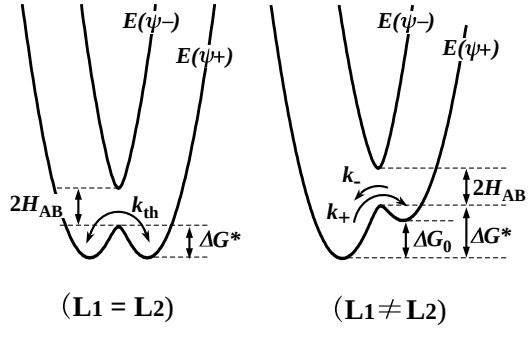

Fig. 7. Potential surfaces for symmetric and asymmetric systems

The question of whether such an asymmetric mixed valence state undergoes intramolecular electron transfer (localized or delocalized) depends on two factors: (1) the potential difference, ΔG_0, and (2) the electronic coupling, H_{AB}. Larger contributions of H_{AB} tend to delocalize the system, whereas a larger ΔG_0 tends to localize the system. When H_{AB} and ΔG_0 are of appropriate magnitude, two mixed valence isomers should exist where one is a major isomer and the other a minor one, and intramolecular electron transfer occurs within each isomer. The intramolecular electron transfer in the major isomer results in the formation of the minor isomer and *vice versa*. Thus far, this behaviour in an asymmetric mixed valence state has not been reported to our best knowledge. We found preliminarily that one electron reduced forms of the asymmetrically substituted dimers of ruthenium trimers, **1e–1g**, exhibit the above-mentioned asymmetric mixed valence behaviour: major and minor species in a single mixed valence state exist, and intramolecular electron transfer causes infrared line coalescence in the ν(CO) region. A detailed study is now in progress.

6. Conclusions

There are uncertainties in the rates of electron transfer estimated by Bloch equation simulation of the IR band shape. The precise relationship between IR line shape and electron-transfer dynamics still needs to be refined. But IR band coalescence phenomena observed in this study suggest that intramolecular electron transfer does occur on the IR timescale and offers great advantages for comparing theory and experiment.

Acknowledgment

This work was supported by Grants-in-Aid for Scientific Research (Priority Areas No. 10149102 'Metal-assembled Complexes') and for International Scientific Research (Joint Research No. 11694051) from the Ministry of Education, Science, and Culture, Japan. We also thank collaborators given in the references.

References

[1] ITO T., HAMAGUCHI T., NAGINO H., YAMAGUCHI T., WASHINGTON J., KUBIAK C.P., Science, 277 (1997), 660.
[2] ITO T., HAMAGUCHI T., NAGINO H., YAMAGUCHI T., KIDO H., ZAVARINE I .S., RICHMOND T., WASHINGTON J., KUBIAK C. P., J. Am. Chem. Soc., 121 (1999), 4625.
[3] Ito T., YAMAGUCHI T., KUBIAK C.P., Macromol. Symp., 156 (2000), 269.
[4] YAMAGUCHI T., IMAI N., ITO T., KUBIAK C.P., Bull. Chem. Soc. Jpn., 73 (2000), 1205.
[5] unpublised result.
[6] GREVELS F.-W, KERPEN K., KLOTZBUCHER W.E., MCCLUNG R.E.D., RUSSEL G., VIOTTE M., SCHAFFNER K., J. Am. Chem. Soc., 120 (1998), 10423.

Received 10 April 2003
Revised 17 April 2003

Materials Science, *Vol. 21*, *No. 2*, *2003*

The study of the spin transition process in Na[Fe(Th-Sa)$_2$] by electron paramagnetic resonance*

YU.V. YABLOKOV[1**], V.V. ZELENTSOV[2],
M. AUGUSTYNIAK-JABŁOKOW[1], A. KRUPSKA[1], J. MROZIŃSKI[3]

[1] Institute of Molecular Physics, Polish Academy of Sciences, Smoluchowskiego 17, 60-179 Poznań, Poland

[2]Moscow Physical Technical Institute, 141 700 Dolgoprudnii, Russia

[3]Faculty of Chemistry University of Wrocław, 14 F. Joliot-Curie, 50-383 Wrocław, Poland

The crossover phenomenon in Na[Fe(Th-Sa)$_2$], a representative of a large class of the Fe(III) thiosemicarbazonates, was examined by X-band EPR in temperature range of 80–300 K and magnetisation of a polycrystalline sample was collected in the temperature range of 1.8–300 K. The main results are as follows: The appearance of low-spin (LS) complexes requires the thermal population of the ^{2}A term but the transition process is ruled by other factors. The LS complexes formed are not statistically distributed among the high-spin (HS) ones but tend to assemble in restricted spaces of the crystal lattice (domains) in which both short-range and long-range interactions of the complexes occur. The increase of co-operative interactions between the LS complexes and the enlargement of domains occur gradually with two abrupt changes. Each of the jumps has a different character; the first one is related to a redistribution of the complexes in the domains and the other to a rapid increase of the LS phase volume.

1. Introduction

Spin transitions in compounds containing $3d^4$–$3d^7$ ions are conditioned by the closeness of electronic terms of different multiplicity, which is determined by the ligand field strength and symmetry. The conditions allowing the appearance of low-spin (LS) complexes can be achieved by inducing the thermal population of the relevant term, light induction of the metastable state of LS or by other means such of LS stabilisation, like e.g. external hydrostatic pressure.

---

* The paper was presented at the 13th Winter School on Coordination Chemistry, Karpacz, Poland, 9–13 December, 2002.

** Corresponding author, e-mail: yablokov@ifmpan.poznan.pl.

An essential first requirement for the spin transition is to populate LS multiplet states. Two phenomena are discussed in the literature as the important features of the process of the spin transition: the correlations between the states of a definite multiplicity being the first stage of cooperative interaction [1, 2] and the appearance of domains of the LS complexes [3] as an element of the origin of a new phase. The research into the spin transitions has a long history and mechanisms of the spin transitions have been the subject of many experimental and theoretical studies [2, 4]. However, the mechanisms have not been fully recognised yet [2] and domains have not been observed directly, their presence being inferred from a qualitative conformity of the observed inner hysteresis loops to the common theory of the hysteresis phenomena [4].

Measurements of the magnetic susceptibility, X-ray analysis, Mössbauer spectroscopy are traditionally applied for the study of the spin transitions. EPR has also been applied but up to now its role has been limited to the detection of the crossover phenomenon. As the possibilities of this very sensitive and selective method are essentially larger we have used the EPR method for the study of the spin transitions in the vast class of the thiosemicarbazonates of aromatic aldehydes of $M^+[Fe(Th\text{-}R\text{-}Sa)_2]$ type [5]. The distorted $Fe[O_2N_2S_2]$ octahedron represents the coordination polyhedron in these compounds. The changes of M^+ and R lead to diverse types of the spin transition. In this paper, we present the results of the magnetic susceptibility and EPR study of the continuous spin transition in $Na[Fe(Th\text{-}Sa)_2]$.

2. Description of experimental results

Synthesis of the $Na[Fe(Th\text{-}Sa)_2]$. A stoichiometric amount of a hot aqueous solution of $Fe(NO_3)_3.9H_2O$) was added to a boiling aqueous solution of Na-thiosemicarbazonate. The solution was rapidly filtered and the mother solution was left for cooling. The filtered off crystalline precipitate was washed with water, alcohol and ether.

Magnetic susceptibility. The magnetic susceptibility of the powdered sample of $Na[Fe(Th\text{-}Sa)_2]$ was measured over the temperature range of 1.8–300 K using a Quantum Design SQUID-based MPMSXL-5-type magnetometer. The superconducting magnet was generally operated at a field strength ranging from 0.1 to 5 T. The SQUID magnetometer was calibrated with a palladium rod sample for which the gram magnetic susceptibility was taken as 5.30×10^{-6} cm^3g^{-1} at $T = 293.1$ K. The corrections for diamagnetism were estimated from the Pascal constants [6]. The temperature dependence of magnetic moment of $Na[Fe(Th\text{-}Sa)_2]$ presented in Fig. 1 shows that the decrease of the magnetic moment starts at about 300 K and its value gradually and very slowly diminishes down to about 50 K, then sharply decreases. The HS–LS spin transition occurs in a very wide temperature interval and can be subdivided into two intervals: 300–50 K and 50–1.8 K but even at the lowest temperatures it is not com-

pleted. In this paper, we present the results of our EPR studies of the initial processes taking place in the high-temperature interval.

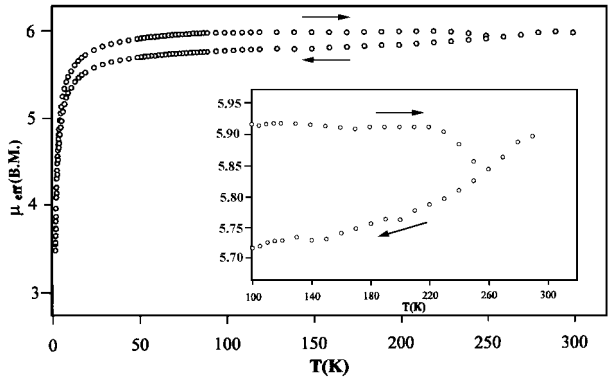

Fig. 1. The temperature dependence of the magnetic moment of Na[Fe(Th-Sa)$_2$]. Arrows indicate directions of the temperature changes. In the insert, the results in the magnetic scale are shown for the temperature range studied by EPR

Electron paramagnetic resonance. EPR measurements of Na[Fe(Th-Sa)$_2$] powder sample were performed with an X-band RADIOPAN SE/X-2547 spectrometer with 100 kHz magnetic field modulation and a home-made nitrogen cryostat in the temperature range of 80–300 K. A weak broad signal with ΔB ~ 120 mT was observed at a room temperature. When the temperature is lowered, a narrower signal appears. This signal is definitely due to LS Fe(III) complexes. We begin to detect it from T = 254 K when its width becomes ΔB = 56 mT (see Fig. 2).

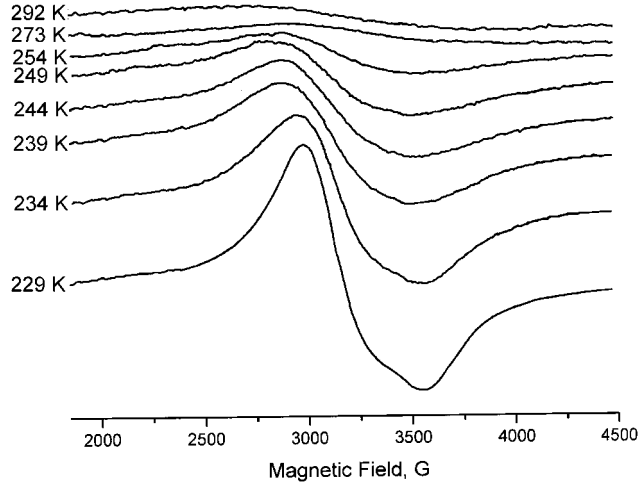

Fig. 2. Transformation of the EPR spectrum of the Na[Fe(Th-Sa)$_2$] complexes at the HS–LS transition with decreasing temperature

With decreasing temperature, the intensity of this signal increases and its linewidth decreases. Hereafter we refer to the width of an individual EPR line obtained in the procedure of fitting of the observed experimental anisotropic spectrum. The parameters of the fit are the *g*-factor components, the line shape and the width of individual components as well as the control parameter – a full width at a half maximum measured for the low field side of the signal. A line width ΔB_{pp} measured between the maximum and minimum of the first derivative of EPR signal has been chosen to characterise wide symmetrical EPR signals at high temperatures. To assess the abundance of the LS complexes, we have estimated the relative values of integral intensities of the signals. Therefore, the nature of the spin transition process can be inferred from examination of the temperature dependencies of ΔB, the signal integral intensity I and the *g*-tensor.

Table 1. Parameters of the EPR signal at selected temperatures[1]

T	ΔB_{pp}, mT	$\Delta B_{individ}$, mT	$g_{\perp}$	$g_{\|\|}$
254	68	56.0	<g> = 2.17	
249	63	54.0		
244	61	48.3	2.248	1.948
239	59	48.0		
234		42.0	2.248	1.948
229		32.7	2.240	1.945
224		30.0		
190		26.9	2.239	1.945
185		22.2	2.236	1.936
163		21.2	2.242	1.937

[1]A linewidth ΔB_{pp} is measured between the maximum and minimum of the first derivative the wide symmetrical EPR signals at high temperature, the $\Delta B_{individ}$ corresponds to the width of an individual EPR line obtained in the procedure of fitting of the observed experimental anisotropic spectrum.

Selected data are shown in Table 1 and in Figs. 2–4. In the temperature range of 254–244 K a nearly symmetrical signal is observed with its width constantly decreasing on decreasing temperature. Starting from $T \sim 244$–239 K the signal becomes asymmetric. Sharp decreases of $\Delta B(T)$ are observed in the T-interval 234–229 K (we shall call it the first critical temperature interval and characterise it by the mean T-value, $T_c^{(1)} = 232$ K) and at T near 187 K (the second critical T-interval, characterised by $T_c^{(2)}$). Moreover, the changes of $\Delta B(T)$ are accompanied by changes in *g*-tensor components: in the vicinity of $T_c^{(1)}$ the $g_{\perp}$ changes from 2.248±0.002 to 2.240±0.002 and $g_{||}$ changes from 1.948±0.002 to 1.945±0.002. At 185 K $g_{\perp} = 2.236$ and $g_{||} = 1.936$ and transforms correspondingly to 2.245 and 1.938 below $T_c^{(2)}$. In the temperature intervals of 229–190 K and 185–82 K the line width ΔB (T) continues to decrease. These intervals differ in the slopes of the $\partial(\Delta B)/\partial T$ dependency (cf. Fig. 3).

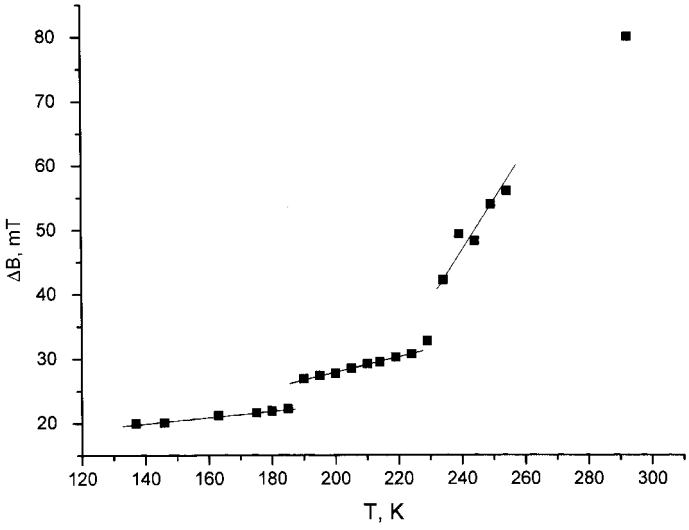

Fig. 3. The temperature dependence of the EPR line width in LS complexes

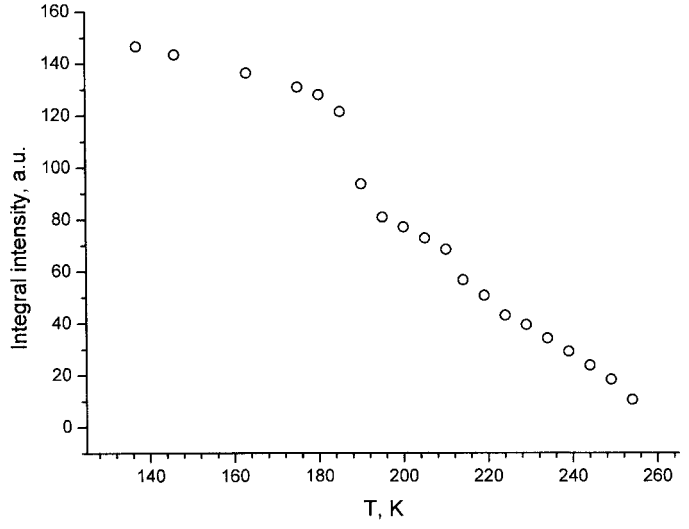

Fig. 4. The temperature dependence of the integral intensity of the EPR signal in LS complexes

The intensity of the EPR signal of the LS complexes, which, as a whole, increases with decreasing temperature, should also be sensitive to the above-mentioned changes and peculiarities in the $\Delta B(T)$ dependence. Fig. 4 shows a distinct discontinuity in $I(T)$ at T = 187 K. However, we were not able to detect any peculiarities in this dependence near 232 K.

3. Discussion

The main source of the information in our study is the linewidth ΔB of the EPR signal. As the LS complex has the electron spin $S = 1/2$, the line width is determined, in general, by three factors: time of paramagnetic relaxation, dipole-dipole interactions with magnetic neighbours and exchange interactions with the LS and HS partners. Our preliminary experiments under the hydrostatic pressure [7] showed that ΔB increases when the pressure is applied to the sample just at low temperatures. For example at $T = 180$ K, ΔB increases from ~ 20 mT at atmospheric pressure to 45 mT at $P = 500$ MPa. This shows directly that we do not need to analyse here a possibility of a relaxation broadening of the EPR line.

Low-spin Fe(III) complexes appear among the high-spin ones. The distance between the iron ions is of 0.63–0.64 nm. Magnetic moment of HS Fe(III) is 5.92 μ_B. Supposing a sixfold environment of LS complex and regarding that the value of its high temperature $\Delta B \sim 56$ mT, the LS complexes are considered as subject to strong enough dipole-dipole interactions with the HS complexes and to relatively weak exchange interactions. These two types of interactions are temperature independent. However, Table 1 and Figs. 2 and 3 show that ΔB essentially decreases with temperature. For example, $\Delta B = 42$ mT at 234 K, i.e. the line width decreases by 14 mT with the T decreasing by 20 K. The only reason for this ΔB narrowing can be a strengthening of the exchange interactions between the LS complexes.

An estimation of the EPR signal intensity shows that at $T = 254$ K the concentration of the LS complexes does not exceed 0.0005–0.001 mol % and, as follows from Fig. 4, the content of the LS complexes increases no more than five times after the temperature lowering down to 234 K. Such a small increase of the LS complexes concentration cannot lead to the observed increase in the exchange interactions if the LS complexes are distributed evenly. This allows us to draw an important conclusion that the appearing LS complexes are not distributed statistically in the crystal lattice of the compound but have a tendency to aggregate in limited areas (domains). This process of aggregation starts simultaneously with the onset of the HS to LS transition. Neglecting possible defects in the crystal lattice, we can consider the appearing LS complexes as not attached to any fixed positions in the structure. More than that, we can suppose that in the conditions of a definite balance between the thermal energy and stabilising factors and due to the translational symmetry of the crystal lattice, the LS state can migrate between the iron complexes. As was shown by the experiment, the aggregation of the LS complexes in domains is energetically efficient, and their amount in some limited areas of the structure increases with decreasing temperature. The enhancement of the exchange interactions allows a conclusion that the LS complexes do not occupy the neighbouring positions in the structure. We can only say that the mean distance between the LS Fe(III) complexes decreases. An availability of the structural bridges – hydrogen bonds – between complexes promotes the strengthening of exchange interactions.

A sharp increase in the LS complexes density in domains takes place at $T_c^{(1)}$. It is accompanied not only by a sharp increase in the exchange interactions, but also by a change in parameters of isolated LS complexes, already different from those of the HS complexes, and in the vicinity of T_c undergoing further changes due to the cooperative interactions between the complexes in domains. Unfortunately, no structural data are available for Na[Fe(Th-Sa)$_2$] but we can use some parameters known for related compounds. For example, the length of the Fe-S and Fe-N bonds in K[Fe(Th-3,5-Cl-Sa)$_2$] changes at the transition from HS compound to LS, from 0.238 nm and 0.227 nm to 0,205 nm and 0.190 nm, respectively [4]. The structural parameters of the iron complexes change at their transformation from HS into LS state. We can suppose that the structural parameters of the LS complexes in domains can differ from those in the bulk crystal being in LS state. As a result at $T_c^{(1)}$ the ligand field on the Fe(III) ion is changed. The supposition is confirmed by the above-mentioned changes in the g_i-values. It should be emphasised that this transformation occurs as a result of redistribution of the LS complex without changing their quantity, which is indicated by the fact that no anomaly is observed in the signal intensity near $T_c^{(1)}$ (see Fig. 4).

The changes of the properties of the compound studied at $T = T_c^{(2)}$ are of a completely different character. At this temperature, a new sharp increase in the exchange is accompanied by a strong increase in the number of LS complexes, confirmed by an increase in the signal intensity shown in Fig. 4. The process in question can be treated as related to an enlargement or aggregation of domains leading to the extension of the phenomena responsible for the arrangement of LS and HS complexes in domains and the electron structure of domains in large volumes of the crystal. The relative concentration of the LS complexes remains not too high and we can state, in the accordance to the magnetic susceptibility data that only a small part of the complexes are in the LS state. In the temperatures above $T_c^{(1)}$, between $T_c^{(1)}$ and $T_c^{(2)}$, and below $T_c^{(2)}$ the increase in the LS complexes number and exchange interactions in domains, has a continuous character but its rate is different.

The evolution of the EPR spectra of the LS complexes observed in the process of the spin transition allows a conclusion that the exchange interactions between LS complexes become apparent already at their smallest concentrations. On the other hand, the exchange interactions are possible only after the appearance of some LS aggregates in the crystal lattice, i.e. the exchange only allows a detection of conglomeration of LS complexes in domains. The existence of domains has not been proved earlier [3], however, an evolution of the LS state in the crossover process was certainly analysed both experimentally and theoretically [2]. We shall mention some of the works. In [1, 8] the model of the static intermolecular interactions taking into account the molecular vibrations was developed. Spiering, Willenbacher et al. [9, 10] discussed the elastic interaction between the LS ions via the image pressure. The starting point of all considerations was the observed volume change and deformations of the lattice accompanying the transition of the ions from the HS to the LS state. We assume that these approaches can be used for analysis of the phenomena in domains to show an important role of the short-range correlations between LS complexes. At

present we cannot infer about the character of these correlations. The Lorentz line shape observed for EPR of the LS complexes confirms that a large number of LS complexes are involved into exchange interactions in domains. The existence of the intermolecular contacts in the structure of $Na[Fe(th\text{-}Sa)_2]$ explains both possibility of the mutual influence between the iron complexes being in a definite spin state and the exchange interactions between all complexes (LS–LS, HS–HS and LS–HS). At the same time, long-range interactions have also been proved to be significant, as demonstrated by the anomalies at $T_c^{(1)}$ and $T_c^{(2)}$.

4. Conclusions

The study of the diffuse HS−LS transition in $Na[Fe(Th\text{-}Sa)_2]$ by EPR allowed a direct observation of some important features of the transition, which have hitherto been questionable.

The process of transition of Fe(III) complexes to the low spin state is shown to involve the formation of domains comprising a finite number of the LS complexes. The complexes do not necessarily occupy the nearest-neighbour positions in the crystal lattice. Just opposite, it is shown that the mean density of the LS complexes in a domain increases with their total concentration.

We consider the process of the growth of domains (i.e., inclusion of new LS complexes into a domain) as being ruled by short-range interactions. These interactions, at the beginning of the HS–LS transition, have a character of pair correlations and can show some the features inherent to the co-operative system. (In the same way the pair Jahn–Teller correlations in the doped pair of JT complexes are shown to model the co-operative interactions in the concentrated JT crystal [11, 12]). And indeed, the merging of domains, or their growth and reorganisation are cooperative process and stimulated by long- range interactions. Additional weak changes in the LS complexes parameters accompany the transformation of the domain structure of the HS–LS system.

All the above-mentioned observations should be a subject of further investigation.

References

[1] ZELENTSOV V.V., MOKSHIN V.M., SOBOLEV S.S., SHIPILOV V.I., Khim. Fizika, 7 (1988), 51.

[2] SPIERING H., KOHLHAAS T., ROMSTED H. HAUSER A., BRUNS-YIMLAZ C., GÜTLICH P., Coord. Chem. Rev., 190–192 (1999), 629.

[3] MOLNAR G., BOUSSEKSOU A., ZWICK A., MCGARVEY J., Chem. Phys. Lett., 367 (2003), 593.

[4] KOGAN V.A., ZELENTSOV V.V., LARIN G.M., LUKOV V.V., *Transition Metal Complexes with Hydrazones* (in Russian), Moscow, Science, 1990.

[5] ZELENTSOV V.V., Russian Chem. J., 49 (1996), 86.

[6] KÖNIG E., *Magnetic Properties of Coordination and Organometallic Transition Metal Compounds*, Springer-Verlag, Berlin, 1966.

[7] ZELENTSOV V.V., YABLOKOV YU.V., AUGUSTYNIAK-YABLOKOV M., KRUPSKA A., MROZINSKI J. (to be published).

[8] SHIPILOV V.I., FIDIRKO V.A., ZELENTSOV V.V., MOKSHIN V.M., Solid State Phys. Russ., 21 (1979), 3553.
[9] SPIERING H., MEISSNER E., KÖPPEN H., MÜLLER E.W., GÜTLICH P., Chem. Phys., 68 (1982), 65.
[10] WILLENBACHER N., SPIERING H.J., Phys. C: Solid State Phys., 21 (1988), 1423.
[11] EREMIN M.V., IVANOVA T.A., YABLOKOV YU.V., GUMEROV R.M., Zhur. Exper. Theor. Fiz., 87 (1984), 220.
[12] AUGUSTYNIAK-YABLOKOV M., YABLOKOV YU.V., Solid St. Comm., 115 (2000), 439.

Received 28 March 2003
Revised 9 April 2003

Materials Science, *Vol. 21*, *No. 2*, *2003*

Tin selenide thin films prepared through combination of chemical precipitation and vacuum evaporation technique

ZULKARNAIN ZAINAL[1*], SARAVANAN NAGALINGAM[1], ANUAR KASSIM[1], MOHD. ZOBIR HUSSEIN[1], WAN MAHMOOD MAT YUNUS[2]

[1]Department of Chemistry, Universiti Putra Malaysia, 43400 Serdang, Selangor, Malaysia

[2]Department of Physics, Universiti Putra Malaysia, 43400 Serdang, Selangor, Malaysia

Tin selenide thin films were prepared through combination of chemical precipitation and vacuum evaporation technique. The vacuum deposition was carried out using different quantities of the starting material. The differences in the structural and compositional properties of the films deposited were studied. The films were characterised using various techniques such as X-ray diffractometry, scanning electron microscope and energy dispersive analysis of X-ray. Photoactivity of the samples was studied using the linear sweep voltammetry. The films were found to be p-type semiconductors. The optical bandgap energy was found to be indirect and equal to E_g = 1.25 eV.

Key words: *tin selenide; photoelectrochemical cell; thin film; evaporation*

1. Introduction

The search for thin-film materials for solar energy conversion and other related applications has been recently identified. It is not surprising now that a lot of effort has been geared towards metal chalcogenides as this class of materials had shown somewhat superior performance when compared to others [1, 2]. The synthesis and characterisation of metal chalcogenides via different techniques have attracted considerable attention due to their application prospects. These compounds are also reported to be used as sensor and laser materials, thin films polarizers and thermoelectric cooling materials [1, 2]. They are usually prepared through electrochemical and chemical deposition method and are quite attractive for designing systems for

[*]Corresponding author, e-mail: zulkar@fsas.upm.edu.my.

electro-optics and photoelectrochemical (PEC) solar cells. Improvements in process reproducibility laid the groundwork for introducing a new product, which is composed of several innovative materials and methods. These metal chalcogenides have been prepared in the form of thin films by various researchers.

A considerable attention has also been given by various researchers to the preparation techniques of tin selenide (SnSe) thin films. Among the methods used are chemical bath deposition [3], vacuum evaporation, chemical vapour deposition [4–12] and electrodeposition [13, 14]. SnSe is a narrow band gap binary IV–VI semiconductor displaying a variety of applications such as an essential material in photoelectrochemical solar cells to suppress the photocorrosion and to enhance the fill factor in electrical switches and in junction devices [12]. Because of their anisotropic character, tin chalcogenides are attractive layered compounds, and can be used as cathode materials in lithium intercalation batteries [15]. The indirect character of the bandgap of SnSe is a common property of IV–VI compounds and has been confirmed by band structure calculations for SnSe [16]. It has orthorhombic crystal structure with layers stacked along the c axis and $a = 4.30$ Å, $b = 4.05$ Å and $c = 11.62$ Å [17]. Motivated by the potential applications of tin chalcogenides, investigations of these compounds are becoming particularly active in the field of materials chemistry. The studies comprise spectroscopy, sensing properties and electronic structure of SnSe compounds [18]. In the present work, we have prepared SnSe thin films through vacuum evaporation. The SnSe source for the evaporation was obtained through chemical precipitation technique.

2. Experimental

SnSe powder was obtained by the chemical synthesis. The desired amount of elemental selenium was dissolved in 5.6 M NaOH solution and stirred rapidly for 20 min. Upon complete dissolution of elemental Se, the Sn solution complexed with EDTA was added and the stirring process was maintained for almost 15 min. Black precipitate (SnSe) obtained was filtered and washed with distilled water and dried in oven for 6 h. The required amount of the SnSe powder was used as the source for the vacuum evaporation system to obtain two samples of SnSe films with different thicknesses.

Thin films of SnSe were deposited using the synthesised powder in an Edwards Auto 306 Vacuum Coating Unit. Indium-doped tin oxide (ITO) glass was used as the substrate. The substrates were cleaned ultrasonically in ethanol and distilled water before the deposition process. The vacuum was kept at 8×10^{-5} mbar. SnSe powder was evaporated from a tungsten filament onto the ITO glass substrate to form the semiconductor layer. The source-to-substrate distance was maintained at 15 cm. The films were found to be uniform, free of pinholes and adhered well to the ITO glass substrate, their thicknesses amounted to 10 and 22 μm.

X-ray diffraction (XRD) analysis was carried out using a Siemens D-5000 Diffractometer for the 2θ ranging from 2° to 60° with CuK_α line used as a beam (λ =

1.5418 Å). Scanning electron microscopy (SEM) and energy dispersive analysis of X-ray (EDX) was performed on a JEOL JSM 6400 Scanning Microscope. Optical absorption study was carried out using the Perkin Elmer UV/Vis Lambda 20 Spectrophotometer. The film-coated ITO glass was placed across the sample radiation pathway while an uncoated ITO glass was put across the reference path. From the analyses of the absorption spectra the band gap energy E_g was determined. The ellipsometry technique was used to determine the thickness of the films using an ELX-02C Ellipsometer.

Photoelectrochemical (PEC) experiments were performed in the $[Fe(CN)_6]^{3-}$ /$[Fe(CN)_6]^{4-}$ redox system, by running linear sweep voltammetry (LSV) between –0.4 V and –1.0 V. The electrolytes were prepared using analytical grade reagents and deionised distilled water. An EG&G Princeton Applied Research potentiostat driven by a software model 270 Electrochemical Analysis System was used to control the LSV process and to monitor the current and voltage profiles in a conventional three-electrode cell. Ag/AgCl was used as the reference electrode. The working and counter electrodes were made of SnSe coated ITO glass substrate and platinum, respectively. The counter electrode was polished prior to the insertion into the electrolyte cell. A tungsten-halogen lamp (100 W) was used for illuminating the electrode.

3. Results and discussion

The XRD of the SnSe powder obtained from the chemical precipitation technique is shown in Fig. 1. The peaks in the pattern indicate the formation of the orthorhombic phase of SnSe. The results are well matched with the standard JCPDS values (File No. 32-1382) for SnSe (Table 1). No peaks corresponding to Se in the XRD pattern are seen. This indicates that the sample powder contains no elemental Se.

Table 1. XRD data of SnSe powder

2θ (deg)	d (Å)	
	Values obtained	JCPDS values (File No. 32-1382)
25.2	3.53	3.52
29.3	3.04	3.05
30.2	2.94	2.94
31.0	2.90	2.90
37.5	2.39	2.38
43.0	2.09	2.09
49.3	1.84	1.83
53.9	1.69	1.68

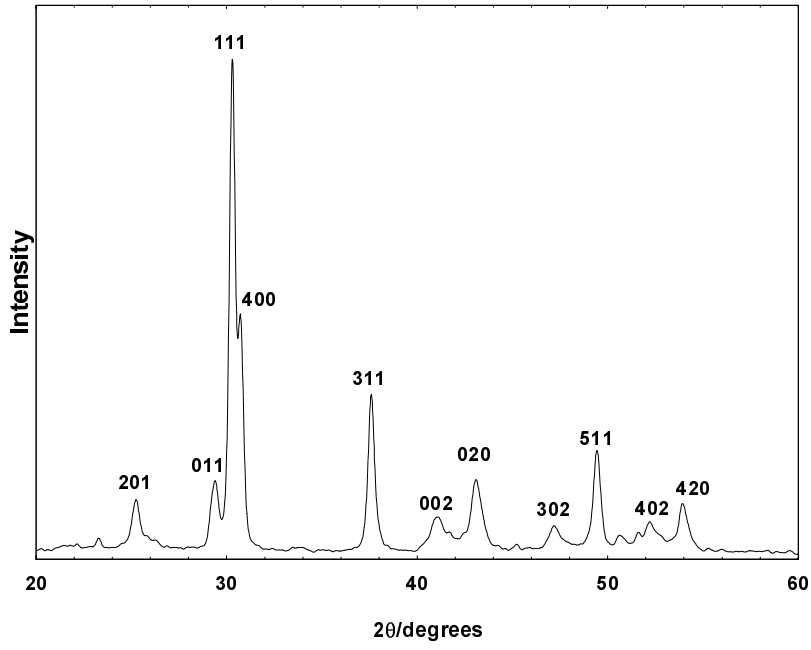

Fig. 1 X-ray diffraction spectrum of SnSe powder

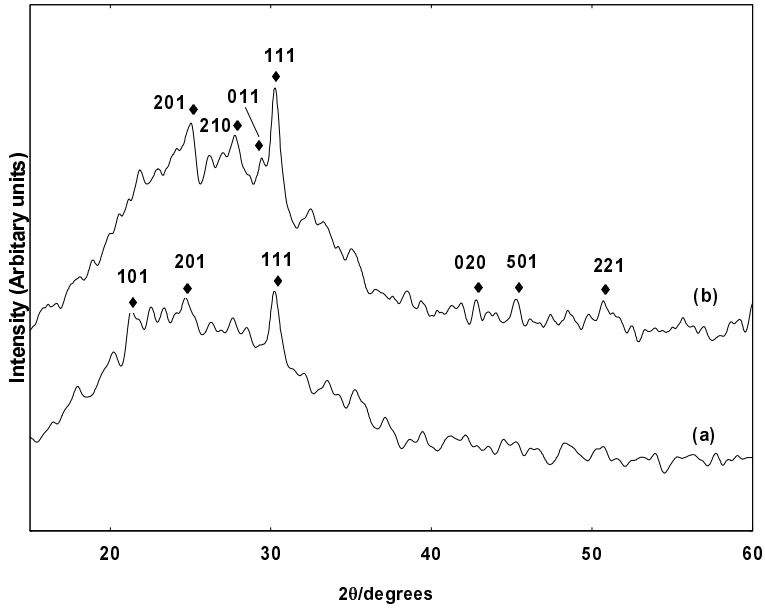

Fig. 2 X-ray diffraction spectrum of SnSe thin films with different thicknesses: a) 0.10 μm, b) 0.22 μm

The XRD patterns of vacuum-deposited SnSe thin films having thickness 0.10 μm and 0.22 μm are shown in Fig. 2a, b, respectively. The broad peak appearing at low angle is due to the glass substrate itself. The observation of X-ray peaks in both SnSe thin films indicates that the vacuum-deposited films are polycrystalline. The intensities of the signals are rather weak due to the thin film nature of the samples. Table 2 lists the observed *d*-values for SnSe thin films in comparison with the JCPDS standard data (File No. 32-1382). The observed *d*-values are in a good agreement with the standard values for the orthorhombic structure of SnSe. The strongest peak for both films occurred at $2\theta = 30.3°$ with $d = 2.95$ Å (corresponding to the (111) reflection). It indicates that the preferred orientation lies along the (111) direction for vacuum deposited SnSe thin films.

Table 2. XRD data of SnSe films

Thickness (μm)	2θ (deg)	d (Å) measured	d (Å) standard (File No. 32-1382)	*hkl*
0.10	21.3	4.16	4.15	101
	24.7	3.60	3.52	201
	30.2	2.95	2.95	111
0.22	25.1	3.54	3.52	201
	27.7	3.31	3.37	210
	29.3	3.04	3.05	011
	30.3	2.95	2.95	111
	42.8	2.11	2.10	020
	45.2	2.00	2.03	501
	50.6	1.80	1.80	221

The dominant orientation in the (111) plane has also been reported by other researchers for the SnSe thin films deposited by vacuum deposition [12, 17, 19, 20] and electrochemical deposition [4, 13, 21]. As expected, the crystallinity of the thicker film is better and more X-ray peaks are observed. The intensity of the (111) peak shows a significant increase as the thickness of the SnSe film increases. The crystallite sizes (grain diameter) D of the deposits were determined using the Scherrer's formula [17]:

$$D = \frac{K\lambda}{\omega \cos\theta}$$

where λ is the wavelength of X-rays, θ the Bragg angle and ω the full width at a half maximum (in radians). K varies with (*hkl*) and crystallite shape but usually is nearly equal to 1. The grain size increased from 14.3 nm to 15.0 nm when the thickness of the film was increased (see Table 3).

Table 3. Grain size in SnSe thin films

Thickness (μm)	Peak	Grain size (nm)
0.10	111	14.3
0.22	111	15.0

Figure 3 shows the SEM micrographs of SnSe films. The thinner films exhibit growth of small grains distributed across the surface of the substrate. To have a visual reference on the two films and to be able to compare them, a small portion of the substrate surface containing the thicker film was cleaned with HNO_3. This portion of the surface is marked with 'X' in Fig. 3b. This reveals the thicker surface coverage of the SnSe onto the substrate in the latter film. The micrographs of these films indicate uniform surface coverage and smooth SnSe texture. The EDX analysis indicates the Sn to Se ratio to be 0.9, which is almost at the stoichiometry level.

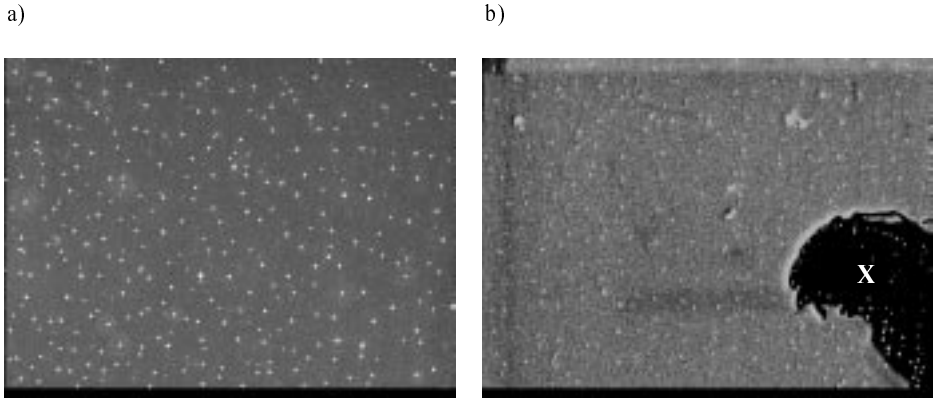

Fig. 3. SEM micrographs of SnSe prepared at different thickness: (a) 0.10 μm (b) 0.22 μm

The band-gap energy and transition type was derived from mathematical treatment of the data obtained from the optical absorbance vs. wavelength with the following relationship for near-edge absorption:

$$A = \frac{k\left(h\nu - E_g\right)^{n/2}}{h\nu}$$

where ν is the frequency, h is the Planck's constant, k equals a constant while n carries the value of either 1 or 4. Figure 4 shows the absorbance spectra of the films of different thicknesses. It is clear that the thicker film has a higher absorption. This could be due to more SnSe material deposited onto the surface of the substrate. The band gap E_g could be obtained from a straight line plot of $(Ah\nu)^{2/n}$ as a function of $h\nu$: an extrapolation of the value of $(Ah\nu)^{2/n}$ to zero, will give E_g. If a straight line graph is

obtained for $n = 1$, it indicates a direct electron transition between the states of the semiconductor, whereas the transition is indirect if a straight line graph is obtained for $n = 4$.

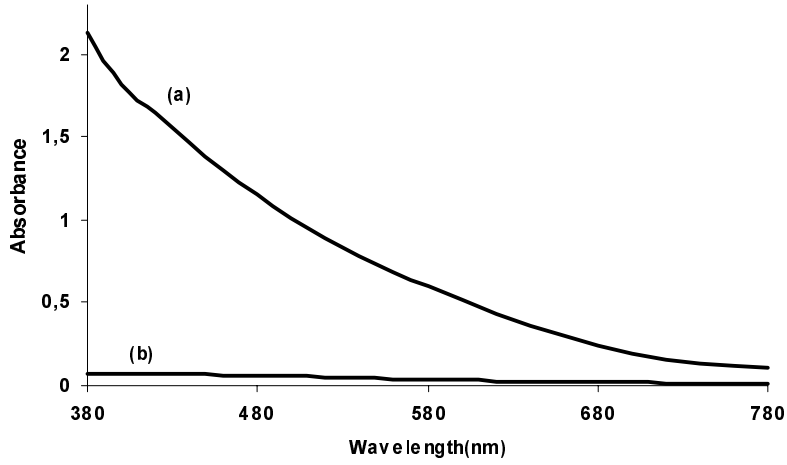

Fig. 4. Optical absorbance vs. wavelength spectrum for SnSe films. Thickness: a) 0.22 μm, b) 0.10 μm

A linear trend is apparent where n in the relationship (1) equals 4. The straight-line behaviour in Fig. 5 testifies an indirect transition of the band structure. The line segments required to by pass the energy of the gap lies at about 1.25 eV for the SnSe film. A similar band-gap value has also been reported by other researchers for vacuum evaporated SnSe films [6, 17, 19, 20].

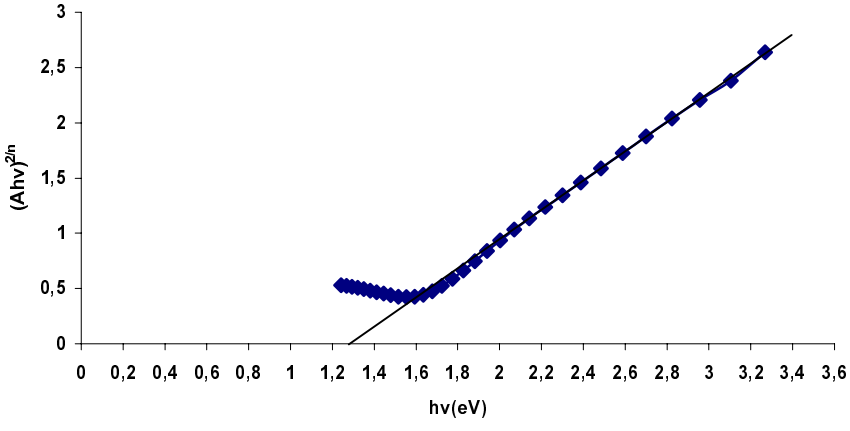

Fig. 5. Plot of $(Ah\nu)^{2/n}$ vs. $h\nu$ in an SnSe film with $n = 4$

Figure 6 shows the difference between the photocurrent I_p and the dark current I_d for the two films when illuminated with a tungsten-halogen lamp (100 W). An in-

crease in the current could be observed for the both samples, which was employed as a cathode in the electrochemical cell as the potential is swept to more negative region. A comparison between the two samples indicates an increase in the photoresponse for the thicker film. The reason for the increase in the photoresponse could be explained in term of the grain size. As the grain size increases from 14.3 to 15.0 nm, the grain boundaries are reduced. The boundaries are known to act as recombination centres for minority carriers and trapping centres for majority carriers.

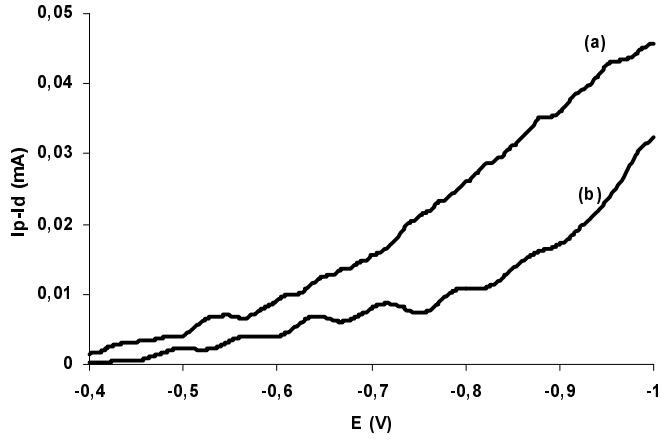

Fig. 6. Comparison of photosensitivity of the samples. Thickness (a) 0.22 μm (b) 0.10 μm

The dependence shown in Fig. 6 confirms that the films possess semiconducting behaviour. The fact that the photocurrent occur on the negative (cathode) potential indicates that the films prepared are of the *p*-type and they can be deployed as photo cathode in the photoelectrochemical cell application to facilitate a reduction reaction of the electro active species in the solution.

4. Conclusion

Clear, transparent SnSe films with different thickness could conveniently be prepared by combination of chemical precipitation and vacuum evaporation technique. The SnSe powder preparation method is less tedious than the previously used solid-state method [6, 17, 19, 20]. The preferred orientation of the crystallites lies along the (111) direction. The thicker SnSe film exhibits a higher photoactivity. The band gap was found to be indirect and equal to 1.25 eV.

Acknowledgements

We are grateful to the Malaysian Government for providing the grant under IRPA No. 09-02-04-0369-EA001. We would like to thank the Department of Physics, Universiti Putra Malaysia for providing

the laboratory facilities. One of us (S.N.) would like to thank the Ministry of Science, Technology and the Environment for the National Science Fellowship (NSF).

References

[1] LINDGREN T., LARSSON M., LINDQUIST S., Sol. Energy Mater. Sol. Cells, 73 (2002), 377.
[2] ZWEIBEL K., Sol. Energy Mat. Sol. Cells, 63 (2000), 375.
[3] PRAMANIK P., BHATTACHARYA S., J. Mater. Sci. Lett., 7 (1988), 1305.
[4] JOHN J., PRADEEP B., MATHAI E., J. Mater. Sci., 29 (1994), 1581.
[5] BENNOUNA A., TESSIER P., PRIOL M., DANG TRAN Q., ROBIN S., phys. stat. sol. (b), 117 (1983), 51.
[6] DANG TRAN Q., phys. stat. sol. (a), 86 (1984), 421.
[7] RAO T.S., CHAUDHURI A.K., J. Phys. D: Appl. Phys., 18 (1985), L35.
[8] RAO T.S., SAMANTHARY B.K., CHAUDHURI A.K., J. Mater. Sci. Lett., 4 (1985), 743.
[9] DANG TRAN Q., Thin Solid Films, 149 (1987), 197.
[10] SHARON M., BASAVASWARAN K., Solar Cells, 20 (1987), 323.
[11] SINGH J.P., BEDI R.K., Jap. J. Appl. Phys., 29, 6 (1990), L869.
[12] SUGUNA P., MANGALARAJ D., NARAYANDASS S.A.K., MEENA P., phys. stat. sol. (a), 155 (1996), 405.
[13] SUBRAMANIAN B., MAHALINGAM T., SANJEEVIRAJA C., JAYACHANDRAN M., CHOCKALINGAM M.J., Thin Solid Films, 357 (1999), 119.
[14] ENGELKEN R.D., BERRY A.K., VAN DOREN T.P., BOONE J.L., SHAHNAZARY A., J. Electrochem. Soc., 133 (1986), 581.
[15] YAMAKI J., YAMAJI A., Physica, B 150 (1981), 466.
[16] SINGH J.P., BEDI R.K., Thin Solid Films 199 (1991), 9.
[17] PADIYAN D.P., MARIKANI A., MURALI K.R., Cryst. Res. Technol. 35 (2000), 949.
[18] AGARWAL A., J. Cryst. Growth, 183 (1998), 347.
[19] SOLIMAN H.S., Abdel HADY D.A., ABDEL RAHMAN K.F., YOUSSEF S.B., EL-SHAZLY A.A., Physica A, 216 (1995), 77.
[20] SINGH J.P., BEDI R.K., J. Appl. Phys., 68, 6 (1990), 2776.
[21] ZAINAL Z., SARAVANAN N., ANUAR K., HUSSEIN M.Z., YUNUS W.M.M., Greenwich J. Sci. Tech. (in press).

Received 21 January 2003
Revised 14 March 2003

Materials Science, *Vol. 21*, *No. 2*, *2003*

Metal complexes immobilised in/on porous matrices – possible enzyme mimics*

I. LABÁDI[1**], I. SZILÁGYI[1], N.I. JAKAB[2], K. HERNÁDI[3], I. PÁLINKÓ[2]

[1]Department of Inorganic and Analytical Chemistry, University of Szeged, Dóm tér 7, Szeged, H-6720 Hungary

[2]Department of Organic Chemistry, University of Szeged, Dóm tér 8, Szeged, H-6720 Hungary

[3]Department of Applied and Environmental Chemistry, University of Szeged, Rerrich B. tér 1, Szeged, H-6720 Hungary

Cu(II) histidine or Cu(II)-diethylene-triamino-μ-imidazolato-Zn(II)-*tris*-aminoethylamine triperchlorato complexes were prepared and immobilised in/on porous matrices (montmorillonite and silica gel) *via* (i) adsorption/hydrogen bonding, (ii) electrostatic forces or (iii) grafting with covalent bond. It was found that immobilisation increased catalytic activity and catalyst lifetime in the decomposition reaction of hydrogen peroxide relative to the matrix-free complexes. The immobilised materials were characterised by experimental and computational methods.

Key words: *Cu(histidine) complexes; Na-montmorillonite; silica gel; host-guest substances; FT-IR spectroscopy; immobilisation; anchoring*

1. Introduction

Homogeneous catalysts are generally more selective and occasionally more active than their heterogeneous counterparts. Nevertheless, they also have several disadvantages. Just two of them are their tedious and often unsuccessful separation from the reaction mixture and their shorter lifetime. Both of these unfavorable features may be eliminated if the homogeneous complexes are heterogenized. Complexes immobilised in solid or semi-solid matrices may mimic enzymes [1, 2], which may mean high ac-

---

* The paper was presented at the 13th Winter School on Coordination Chemistry, Karpacz, Poland, 9–13 December, 2002.

** Corresponding author, e-mail: dome@chem.u-szeged.hu.

tivity at low temperature and very high selectivity: typical features of environmentally friendly procedures.

If one intends to model enzymes or wants to exploit their high activity and (or) selectivity, a viable way is trying to anchor the prosthetic group(s) found or assumed to be responsible for these parameters onto rigid or semi-rigid supports. When Cu-amino acid or Cu-Zn–N-containing multidentate ligand complexes are immobilised on supports, enzyme mimics may be obtained, which might be efficient and selective catalysts in a large variety of enzyme-catalysed reactions [3]. Immobilisation can be done in several ways, for a detailed description of various possibilities [4]. In this work, we show some feasible methods for the preparation. The synthetic methods and the resulting hybrid materials are described in the present paper. The immobilised complexes were characterised by various experimental and computational methods and some of them were used as catalysts in the decomposition reaction of H_2O_2.

2. Experimental

2.1. Synthesis of the complexes and methods for immobilisation

Materials. For the synthetic work $CuCl_2$ or $Cu(NO)_3$ (products of REANAL), L-histidine (Aldrich), montmorillonite (Bentolit-H, Laporte, ion-exchange capacity: 80 meq/100 g, BET surface area: 90 m^2/g (as-synthesised) or silica gel (Aldrich, TLC high-purity grade, average particle size: 5–25 μm, BET surface area: ~500 m^2/g, Fe^{3+}: 0.001 %, Cl^- 0.003 %, pH [10% aqueous suspension] ~ 6.8, average pore diameter: 6 nm) were used. For the preparation of the Cu(II)-diethylene-triamino-μ-imidazolato-Zn(II)-trisaminoethylamine triperchlorato complex (denoted as **C** in the present paper) zinc and copper perchlorate (products of REANAL), imidazole, diethylene triamine and tris(2-aminoethyl)amine (products of Aldrich) were applied.

Immobilisation *via* adsorption/hydrogen bonds. During this form of immobilisation a calculated amount of L-histidine was adsorbed in montmorillonite or on silica gel at neutral pH. Then, the metal ions were introduced from solution, and finally, the empty coordination sites of the central ions were filled in by added L-histidine. During and after applying the method, the host material was washed free of excess amino acid. Anchoring the amino acid was by adsorption first, and then by using the electrostatic field of the Cu^{2+} ions.

Immobilisation *via* electrostatic forces. The Cu–L-histidine complex was prepared *ex situ* and then it was introduced into the pore system of montmorillonite. In this procedure the copper salt was dissolved in water, and then the ligand was added under continuous stirring. During the formation of the complex changes in pH were registered. The starting solution was acidic (pH = 3.2 for the copper solution) becoming close to neutral by the end of the reaction. Then, the complex was crystallised

by cooling and evaporating the excess of solvent. The preformed complexes were introduced into montmorillonite using isopropanol as a solvent. The procedure applied was ion exchange of the bulky complex ion in the pre-swollen montmorillonite (0.6 mmol complex ion/g montmorillonite).

In the second case, Cu(II) ions were introduced by ion exchange into (onto) montmorillonite or silica gel and they served as starting materials. Ion exchange was performed twice at 343 K for 12 h each time. The concentration of the exchanged ions was the same as when the procedure was performed by the preformed complexes. The complexes were synthesised *in situ* inside the pores by adding ligand molecules, enough for the presumed fourfold coordination. The synthesis was performed using isopropanol solution of the ligands under reflux for 24 hours.

Before immobilisation the Cu(II)-diethylene-triamino-μ-imidazolato-Zn(II)-tris-aminoethylamine triperchlorato complex was prepared *ex situ* following the general recipe published in ref. [5]. In this procedure the zinc or the copper perchlorate was dissolved in water and then the ligands (imidazole and diethylene triamine for the copper salt solution and tris(2-aminoethyl)amine for the zinc salt solution) were added under continuous stirring. For preparing the bridged binuclear complex, the two complex solutions were added in 1:1 molar ratio to a quarter of that amount of free Zn(II) in ethanol under vigorous stirring. The stirring was maintained for 24 h and then, the bridged binuclear complex was allowed to crystallise. The immobilised complex catalyst was prepared using isopropanol. The preformed complex was dissolved in isopropanol and this solution was introduced into montmorillonite suspended in isopropanol. Immobilisation occurred with cation exchange.

Immobilisation using *via* covalent bonding. For covalent grafting 3-chloropropyl-functionalised silica gel (Aldrich) was used. Approximately 8% of the OH groups carried the chloropropyl functionality. To enforce bonding at the N-terminal, L-histidine methylester hydrochloride (Aldrich) was the amino acid derivative. The coupling was achieved under base conditions after reflux for 2 hours. Then, the product was divided into two parts. One part was treated with $Cu(NO_3)_2$ solution and the amino acid ester, resulting in Cu–L-histidine methylester complex covalently anchored to silica. The other part was subject to acid hydrolysis and then to subsequent treatment with $Cu(NO_3)_2$ solution and L-histidine, resulting in covalently anchored Cu–L-histidine complex. Before any further use, the immobilised materials were washed free of excess Cu(II) ions as well as ligands and were air-dried.

2.2. Methods of characterisation

The host-free complexes were examined by derivatography, UV and IR spectroscopies. The host materials and the immobilised materials were characterised by powder X-ray diffraction and IR spectroscopy, thermal analysis and BET measurements. The thermal behaviour of the substances was investigated with the use of a Derivatograph Q instrument. The samples were studied under the following condi-

tions: mass sample 100 mg, heating rate 10 deg/min, temperature range 300–1273 K in air. X-ray diffractograms were registered on a DRON 3 diffractometer. BET measurements were performed in a conventional volumetric adsorption apparatus cooled to the liquid nitrogen temperature (77.4 K). Prior to measurements the host samples were pretreated in vacuum at 573 K for 1 h. Neither BET surface area nor basal distance was significantly altered compared to those of the host material (montmorillonite: 90 m^2/g, 1.46 nm (as synthesized)).

Substances obtained by covalent grafting were studied by FT-IR spectroscopy, either by means of the KBr technique or the self-supported wafer method. The KBr pellets (1.2 mg of the substances in 200 mg KBr) or the self-supported wafers (10 mg/cm^2) were pressed from the materials and these were applied for monitoring changes in the IR spectra of the samples. The FT-IR spectra of the host and guest materials and the host–guest complexes prepared by both the two-step and three-step methods were taken and compared. The 3800–480 cm^{-1} range was investigated. The spectra were recorded by a Mattson Genesis I spectrophotometer with 2 cm^{-1} resolution. For a spectrum 126 scans were collected. Spectra of the KBr pellets were taken at 298 K (every host–guest complex was studied) in air. Self-supported wafers (not all but only few host–guest complexes were investigated due to experimental difficulties encountered when making the wafers) were degassed at 348 K, 373 K, 423 K, 573 K, and 673 K for 1 h at each temperature and the IR spectra were recorded after each pretreatment temperature. The spectra were evaluated by the Win-IR package.

The covalently grafted complexes were modelled by the PM3 semi-empirical quantum chemical code [6] included in the HyperChem package [7].

Many of the immobilised samples as well as the effects of host-free complexes were tested in the decomposition of hydrogen peroxide. The reaction was performed in the liquid phase at 298, 313 or 333 K with the Cu–L-histidine containing and at 333 K with the Cu–**C** containing composite. The transformations were followed by UV-VIS spectroscopy (Perkin Elmer). The well-stirred reaction mixture contained 100 mg of the catalysts and 20 cm^3 of 30% hydrogen peroxide aqueous solution.

3. Results and discussion

3.1. Host-free complexes

UV-VIS spectroscopic results revealed that the copper ions were complexed (absorptions relevant to the free ions disappeared form the spectra of the complexes). The structure of the binuclear complex is shown below [5]:

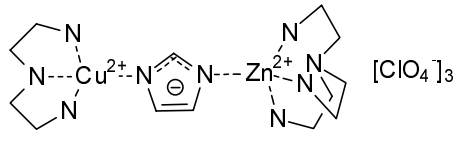

The thermal behaviour of this complex was relatively simple (Fig. 1a). Up to 473 K water was removed in an endothermic process (probably it is the physisorbed and the crystal water). Between 473 K and 573 K the complex decomposed vigorously. This process was exothermic. Above 573 K the organic ligands were removed gradually and continuously.

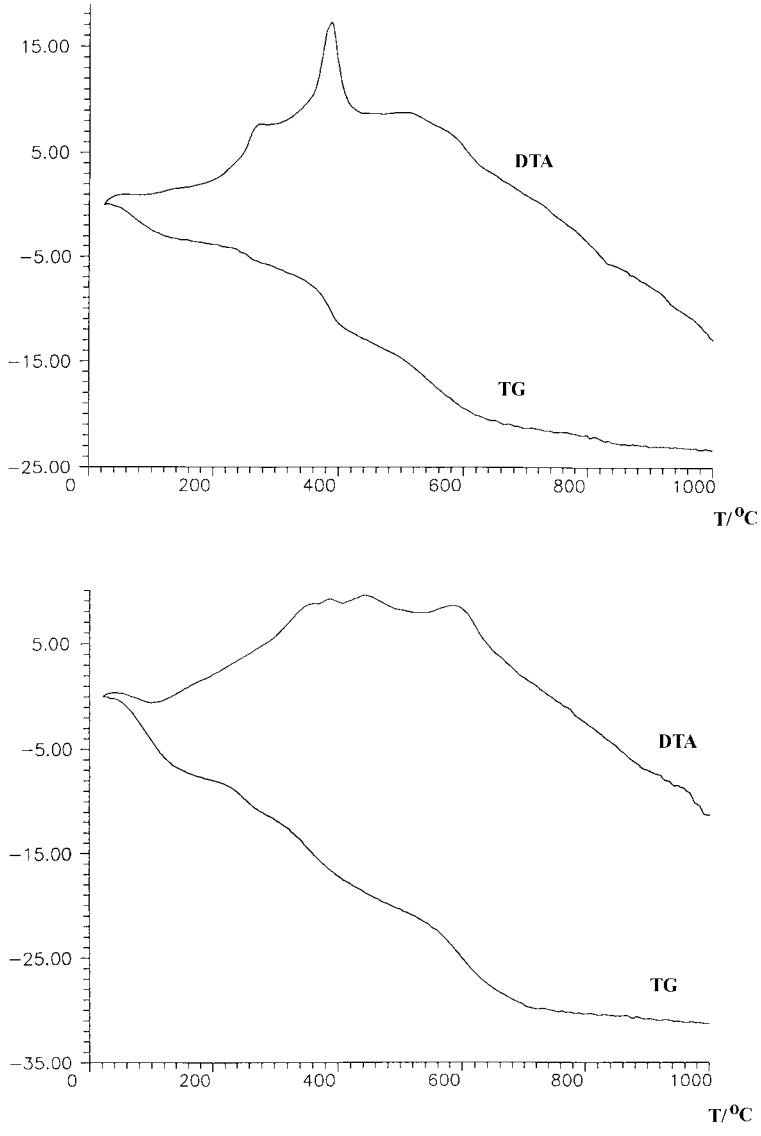

Fig. 1. Thermogravimetric (TG) and differential thermal analytic (DTA) curves of (a) the bare Cu(II)-diethylene-triamino-μ-imidazolato-Zn(II)-*tris*-aminoethylamine triperchlorato complex (**C**) and (b) the **C** complex immobilised in montmorillonite

3.2. Host materials

A great deal of information is available concerning the structural characteristics of the host materials [8]. Let us summarize in a couple sentences the main features relevant to this work.

Montmorillonite is a layered material of the cation exchange ability. It is capable of swelling in a large variety of solvents, such as water, various alcohols, etc. Therefore, it can accommodate the complexes in various positions. If intercalation is too dense, free traffic of the reacting species may be hindered, thus, optimisation of pillaring is of great importance.

Silica gel is a material containing surface OH groups capable of ion exchange. Although it has pore structure, as a first approximation we can consider it as a planar material, at least relative to montmorillonite. The surface OH groups may be functionalised, thus, extended structures may be built if the spacer groups contain reactive groups.

3.3. Intercalated substances

Substances immobilised *via* electrostatic forces. When the complexes investigated were incorporated into any of the porous matrices studied, they became more stable, loosing all ligands at higher temperature (around 1100 K) than the free complexes (around 900 K). Between 373 K and 473 K the dehydration could be observed for the host materials.

As far as the Cu–C complex immobilised in montmorillonite is concerned, ligands are removed in steps (they are combusted since measurements were performed in air). No abrupt changes were observed, indicating that immobilization occurred mainly with ion exchange (Fig. 1b).

In the case of the immobilised Cu–L-histidine complexes, it became clear on the basis of weight losses measured by derivatography that two histidine molecules were bonded to the central ion. Nevertheless, fourfold coordination may be assumed, since histidine generally acts as a bidentate ligand [9, 10]. On heating the composite materials, a multiple weight loss occured, indicating gradual loss of the ligands. By 773 K the immobilised complexes were completely decomposed.

Substances immobilised *via* adsorption/hydrogen bonding. In the Cu–L-histidine-montmorillonite composite (Fig. 2) the loading was low, and the band structure of the host in the low wave number region (1350–400 cm^{-1}) was clearly seen in the spectra of the hybrid materials. Probably due to a low loading, the bands of the carboxylic OH were hardly seen, and the bands of the OH groups in montmorillonite were also not completely used. It seems as if the carboxylic group of histidine, after deprotonation, took part in complex formation and only few Cu^{2+} ions interacted with the OH groups of montmorillonite. Possibly, the complex was immobilised between the layers of montmorillonite by adsorption and (or) hydrogen bonding.

Only a small amount of Cu–L-histidine complex could be anchored to silica gel with this method (Fig. 3).

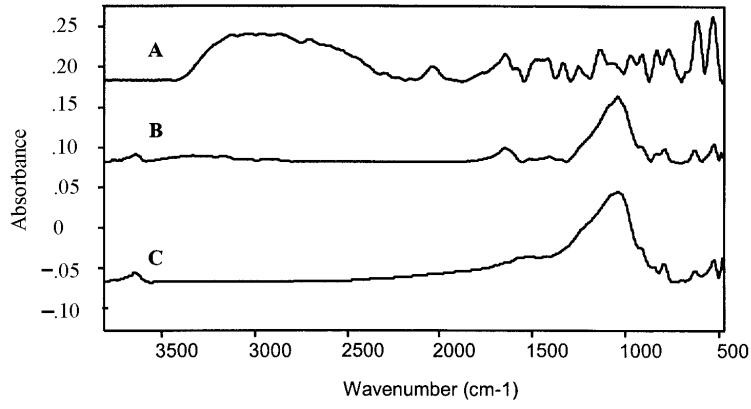

Fig. 2. FT-IR spectra of A) L-histidine, B) the Cu–L-histidine complex immobilised in montmorillonite by the adsorption/hydrogen bonding method, C) the air-dried montmorillonite

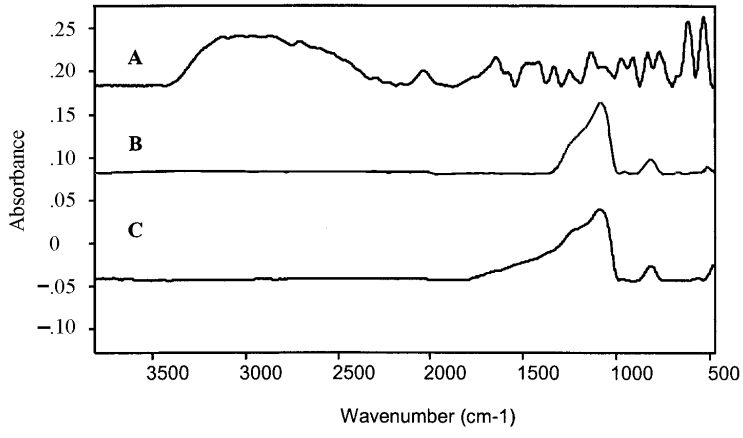

Fig. 3. FT-IR spectra of A) L-histidine, B) the Cu–L-histidine complex immobilised on silica gel by the adsorption/hydrogen bonding method, C) the air-dried silica gel

Substance immobilised *via* covalent bonding. In our view, the most promising anchoring method is covalent grafting. The complex is immobilised indeed, leaching is minimal if occurs at all, and the synthesis method provides some control over the structure of the anchored complex. Moreover, the linker group allows some flexibility for the complex, which is surely advantageous for use as a catalyst. At the beginning of an extended research project silica gel was chosen to be the first host. It contains large amount of OH groups suitable for functionalisation. The chloropropyl-modified version (also available commercially) undergoes easy reaction with either the N-terminal or the C-terminal of an amino acid. The reaction can be controlled by

choosing a suitably protected amino acid. We used C-protected L-histidine, thus an amide was synthesized first. Then, the ester group was hydrolysed and the complex was allowed to form by adding Cu(II) ion-containing solution and unprotected L-histidine to the slurry. The obtained materials were studied by FT-IR spectroscopy. The relevant spectra are shown in Fig. 4.

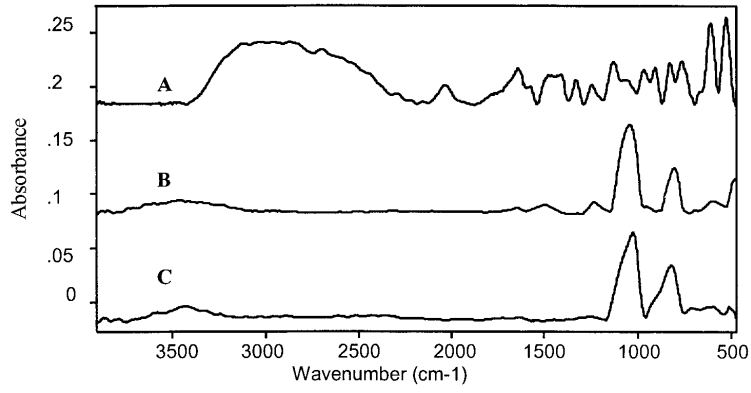

Fig. 4. FT-IR spectra of (A) L-histidine, (B) the Cu–L-histidine complex covalently grafted onto 3-chloropropyl silica gel, (C) the air-dried 3-chloropropyl silica gel

Unfortunately, FT-IR spectra are rarely enough for giving accurate structure for the anchored complex. Some information may be obtained, however. The band in the OH stretching range indicates the presence of uncomplexed OH groups. The large red shift of the C=O band may be taken as the sign of co-ordinative (carbonyl) O–Cu bond. The other two co-ordination sites are probably filled in by the nitrogens of the amino groups, since the relevant bands also moved towards lower wave numbers.

Fig. 5. Molecular model of Cu–L-histidine complex covalently anchored to silica gel *via* the reaction of amino group of one amino acid and t he 3-chloropropyl funcionality of the silica gel

Molecular modelling facilitates visualisation of the possible structure (Fig. 5). In order to obtain a more realistic picture, relatively large silica cluster was chosen. Energetic data may also be obtained by e.g., DFT calculations, however, at present the computational exercise is not tractable by our means.

3.4. Decomposition of hydrogen peroxide

The catalytic activities of complexes (Cu–L-histidine prepared by the in situ as well as the ex situ methods and the Cu–**C** complex) immobilised in montmorillonite were investigated. First, blank reactions were made using the metal salts, the host-free complexes, and the complex-free host and, then, the variously prepared host-guest materials were studied.

While the Cu(II) solution was inactive in the decomposition reaction of hydrogen peroxide ($H_2O_2 = H_2O + 1/2\ O_2$) at any of the temperatures used, in the presence of the complexes the reactions started, although after long induction periods (20 min for Cu –L-histidine and 30 min for the Cu–**C** complex). The montmorillonite was completely inactive, only the Cu(II)-montmorillonite showed a slight decomposition activity at the highest temperature used (333 K).

Measurements revealed that the immobilised Cu–L-histidine complex was able to decompose the peroxide compounds without induction period and, thus, more rapidly than the aqueous complex could do. The activity of the immobilised complex was found to depend on the method of sample preparation, too (Table 1). The *in situ* prepared immobilised complex was found to be more active than the preformed and then introduced one.

Table 1. Rate of hydrogen peroxide decomposition on Cu(II) complexes immobilized in montmorillonite

T/K	Decomposition rate (molecules/central ion/h)		
	Cu–L-histidine		Cu–**C**
	ex situ	*in situ*	*ex situ*
298	0	0	–
313	0.24	0.42	
333	1.46	2.50	97.6 (71.6[a])

[a]Rate of decomposition in the presence of the host-free complex.

The Cu–**C** complex immobilised in montmorillonite was also found to be active in the decomposition reaction, the induction period, however, was 70 min. Nevertheless, the turnover rate for the immobilised material was higher than that of the host-free complex (Table 1, last column). Moreover, the immobilised substance could be reused at least three times without any appreciable loss of activity, while the bare complex decomposed and lost its activity by the end of the first run.

4. Conclusions

Cu complexes were prepared and immobilised in montmorillonite or on silica gel by various methods using primary bonding (ionic or covalent) or secondary forces

(adsorption/hydrogen bonding) for anchoring the complexes through either their ligands or their central ions. The immobilised complexes are promising catalysts, and after some optimisation and some further structural studies they can be used as enzyme mimics and may allow better understanding how certain enzymes work.

Acknowledgement

This work was supported by the National Science Fund of Hungary through the grant OTKA T034793. The financial help is highly appreciated.

References

[1] MITCHEL P.C.H., Chemistry and Industry (1991), 308.
[2] KIRBY A.J., Angew. Chem. Int. Ed. Engl. 35 (1996), 707.
[3] GRÖGER H., WILKEN J., Angew. Chem., Intl. Ed. Eng., 40 (2001), 529.
[4] BALKUS K.J. Jr, GABRIELOV A.G., J. Incl. Phenom. & Mol. Recog., 21 (1995), 159.
[5] SATO M., NAGAE S., UEHARA M., NAKAYA J., J. Chem. Soc., Chem. Commun. (1984), 1661.
[6] STEWART J.J.P., J. Comput. Chem., 10 (1989), 209; ibid. 10 (1989) 221.
[7] *HyperChem 7.0*, Hypercube, Inc., Gainesville, FL, 2001.
[8] NEMECZ E., [in:] *Clay Minerals*, Akadémiai Kiadó, Budapest, 1981, Chapter I.
[9] SUNDBERG R.J., MARTIN R.B., Chem. Rev., 74 (1974), 471.
[10] MARTELL A.E., SMITH R.M. *Critical Stability Constants, Amino Acids*, Vol. 1, Plenum Press, New York, 1974.

Received 1 February 2003
Revised 18 March 2003

Materials Science, *Vol. 21*, *No. 2*, *2003*

Copper(I) complexes as potential CVD precursors – studies in the liquid state and gas phase*

I. SZYMAŃSKA**, R. KUCHAREK, E. SZŁYK

Department of Chemistry, Nicolaus Copernicus University, Gagarina 7, 87-100 Toruń, Poland

Cu(I) complexes with trimethyl phosphite and aliphatic perfluorinated carboxylates of the type $[Cu_2\{P(OMe)_3\}_2(\mu\text{-}RCOO)_2]$ where R = CF_3, C_2F_5, C_3F_7, C_6F_{13}, C_7F_{15}, C_8F_{17}, C_9F_{19} have been prepared as viscous liquids. The spectroscopic results suggest the dimeric structures for complexes in the liquid state, where the metal ions are linked by the bridging carboxylates. This type of bonding was revealed in the gas phase as well. In mass spectra the most intensive signals were observed for the $[Cu_2(RCOO)]^+$ and $[Cu_2(RCOO)_2]^+$ fragments. Thermal decomposition of complexes proceeds as a multistage process, yielding a Cu_2O in the most of cases.

Key words: *Cu(I) complexes, CVD precursors, trimethyl phosphite, perfluorinated carboxylates, TGA*

1. Introduction

Previous studies revealed that gold(I) and silver(I) complexes with perfluorinated carboxylates and tertiary phosphines presented a sufficient volatility for chemical vapour deposition (CVD) [1–5], hence the purpose of this work was to prepare volatile precursors for CVD of copper metal or copper oxide thin films. The EI mass spectrometry, temperature-variable IR spectroscopy and thermal studies were undertaken to determine the kind of species occurring in the gas phase and the mechanism of the reaction of thermal decomposition. The knowledge about the structural and thermal properties should ascertain the suitability of complexes as precursors for CVD, which ought to be competitive to organometallics used at present.

---

* The paper was presented at the 13th Winter School on Coordination Chemistry, Karpacz, Poland, 9–13 December, 2002.

** Corresponding author, e-mail: pola@chem.uni.torun.pl.

2. Experimental section

2.1. Materials

Trimethyl phosphite (98%), perfluorinated carboxylic acids (97–99%) and copper powder for organic synthesis were purchased from Aldrich and used without further purification. Acetonitrile of analytical grade (Fluka) was dried over molecular sieves 4A, next over CaH_2 and, finally, was distilled under dry nitrogen from P_4O_{10} prior to use.

2.2. Methods

Thermal studies were performed with a MOM OD-102 Derivatograph (Paulik and Paulik, Hungary). The atmosphere over the sample was nitrogen; the heating range 293–773 K, heating rate 2.5 K/min, sample mass 40–200 mg, the TG range 50, 100 or 200 mg and the reference material Al_2O_3. Powder diffractograms were recorded with an HZ64/A-2 DRON-1 diffractometer using CuK_α radiation, $\lambda = 0.1542$ nm. Mass spectra were recorded on an AMD-640 mass spectrometer using the EI method in the range of 293–573 K. Temperature-variable IR spectra (4000–400 cm^{-1}) were performed with a Perkin–Elmer 2000 FT IR spectrophotometer in the range of 296–463 K, at the pressure of 10^{-2} mbar. Copper was determined using a Carl Zeiss Jena AAS spectrometer with $Cu(NO_3)_2$ solution as the standard.

2.3. Synthesis

The reactions were performed under argon atmosphere using Schlenk techniques. Suitable copper(II) carboxylates $(RCOO)_2Cu$ were synthesised as described in [6]. In the general procedure, copper(II) carboxylate ($3.0 \cdot 10^{-3}$ moles) was placed in the Schlenk tube, either dissolved or suspended in 45 cm^3 of freshly distilled acetonitrile and copper powder ($9.0 \cdot 10^{-3}$ moles) was added. The suspension obtained was stirred until the solution became pale yellow. Next, $P(OMe)_3$ ($6.0 \cdot 10^{-3}$ moles) in acetonitrile (6 cm^3) was added and the reaction mixture stirred for about 12 h at ambient temperature, filtered and the solvent evaporated on vacuum line, leaving pale yellow viscous liquid. The obtained complexes were unstable in air, turning green. The results of Cu determination were as follows (%) (calc./found):

(**1**) $C_{10}H_{18}Cu_2F_6O_{10}P_2$, Cu (21.2/21.8); (**2**) $C_{12}H_{18}Cu_2F_{10}O_{10}P_2$, Cu (18.1/18.4);
(**3**) $C_{14}H_{18}Cu_2F_{14}O_{10}P_2$, Cu (15.9/15.8); (**4**) $C_{20}H_{18}Cu_2F_{26}O_{10}P_2$, Cu (11.5/11.0);
(**5**) $C_{22}H_{18}Cu_2F_{30}O_{10}P_2$, Cu (10.6/10.4); (**6**) $C_{24}H_{18}Cu_2F_{34}O_{10}P_2$, Cu (9.8/9.3);
(**7**) $C_{26}H_{18}Cu_2F_{38}O_{10}P_2$, Cu (9.1/9.0).

The EI mass spectra were recorded for the complexes in order to prove the formulae. The fragments confirming the stoichiometric composition were as follows: $[Cu_2(RCOO)]^+$, $[Cu_2(RCOO)_2]^+$, $[Cu_2(RCOO)\{P(OMe)_3\}]^+$ and $[Cu_2(RCOO)\{P(OMe)_3\}_2]^+$. For the par-

ticular complexes they were detected at ([m/z]): (**1**) 239, 352, 363, 487; (**2**) 289, 452, 413, 537; (**3**) 339, 552, 463, 587; (**4**) 489, 852, 613, 737; (**5**) 539, 952, 663, 787; (**6**) 589, 1052, 713, whereas for (**7**) only $[Cu_2(RCOO)]^+$ – 639 and $[Cu_2(RCOO)\{P(OMe)_3\}]^+$ – 763 were observed.

3. Results and discussion

3.1. Thermal analysis

The results of thermal analysis are given in Table 1. The examination of the thermoanalytical curves suggests a two-stage, exothermic decomposition process of complexes **2–6**, three-stage in the case of **7** and four-stage for complex **1**. The onset temperature of the first exoterm is in the range 298–303 K, suggesting that the perfluorinated chain had a small influence on the thermal stability of complexes studied.

Table 1. Results of the thermal analysis (in Nitrogen)

Compound	Heat effect	Temperature range[a] [K]			Weight loss on TG [%]		Detached group	Final product
		T_i	T_m	T_f	Found	Calc.		
(1) $[Cu_2\{P(OMe)_3\}_2(\mu\text{-}CF_3COO)_2]$	exo	303	343	403	27.9			
	exo	403	438	443	10.7	38.6		
	exo	443	468	478	26.4			
	exo	478	493	723	11.1	37.6	$2CF_3COO$	Cu_2O
(2) $[Cu_2\{P(OMe)_3\}_2(\mu\text{-}C_2F_5COO)_2]$	exo	298	348	448	35.1	35.6	$2P(OMe)_3$	
	exo	448	488	543	44.2	44.1		Cu_2O
(3) $[Cu_2\{P(OMe)_3\}_2(\mu\text{-}C_3F_7COO)_2]$	exo	298	308	353	20.6			
	exo	353	478	508	61.3	82.2		Cu_2O
(4) $[Cu_2\{P(OMe)_3\}_2(\mu\text{-}C_6F_{13}COO)_2]$	exo	298	323	398	22.9	22.5	$2P(OMe)_3$	
	exo	398	458	663	63.7	64.5		Cu_2O
(5) $[Cu_2\{P(OMe)_3\}_2(\mu\text{-}C_7F_{15}COO)_2]$	exo	298	398	413	21.9			
	exo	413	483	618	63.1	84.8	[c]	$3Cu_2O$: $Cu_2P_2O_7$
(6) $[Cu_2\{P(OMe)_3\}_2(\mu\text{-}C_8F_{17}COO)_2]$	exo	298	423	458	73.3			
	exo	458	468	518	15.3	89.0	[c]	Cu_2O
(7) $[Cu_2\{P(OMe)_3\}_2(\mu\text{-}C_9F_{19}COO)_2]$	exo	298	333	363	18.0	17.7	$2P(OMe)_3$	
	exo	373	493	563	69.4			
	exo	563	653	693	4.9	72.1[b]		Cu_2O

[a] T_i – initial temperature, T_m – maximum temperature, T_f – final temperature.

[b] Decomposition connected with the sublimation.

[c] Unable to determine.

In the case of compounds **2**, **4** and **7,** analysis of the thermogravimetric (TG) curves indicates dissociation of two molecules of phosphite in the first step. Moreover, detachment of the carboxylates residues in the last two stages can be proposed for **1**. In the case of complex **7**, the second and third decomposition process was connected

with the sublimation, probably resulting in the formation of $[Cu_2(C_9F_{19}COO)]$ or $[Cu_2(C_9F_{19}COO)_2]$ fragments. Decomposition reactions of compounds (**1** – **7**) were completed in the range of 508–723 K and the final product appeared to be Cu_2O. Only for the complex **5** a mixture of Cu_2O and $Cu_2P_2O_7$ (3 : 1) was observed. Powder diffractograms of the final products revealed lines for Cu_2O – 0.246, 0.214 nm that correspond to those reported in Powder Diffraction File [7]. IR spectra of the final product of **5** revealed strong vibrations in the range of 1065–1071 cm^{-1} that are characteristic of $Cu_2P_2O_7$ [8]. Similar final products were reported for other copper(I) phosphine complexes, e.g. $[Cu\{P(C_6H_5)_3\}_4]BF_4$ and $[Cu_2\{(P(OPh)_3\}_2(\mu\text{-}RCOO)_2]$ [6, 9]. The temperatures of the final product formation (T_f) were altered irregularly for the perfluorinated chains from C_1 to C_9 and in most cases these are in the range acceptable for CVD purposes with the hot wall reactor (625 K).

3.2. Mass spectrometry

Because the natural abundance of copper is ^{63}Cu (69.1 %) and ^{65}Cu (31.9 %), in compounds having one copper atom two signals can be expected with the intensity ratio 2:1. Species with two copper atoms should reveal three peaks with the characteristic 4:4:1 intensity pattern. As an example, the mass spectrum of **4** is presented in Fig. 1.

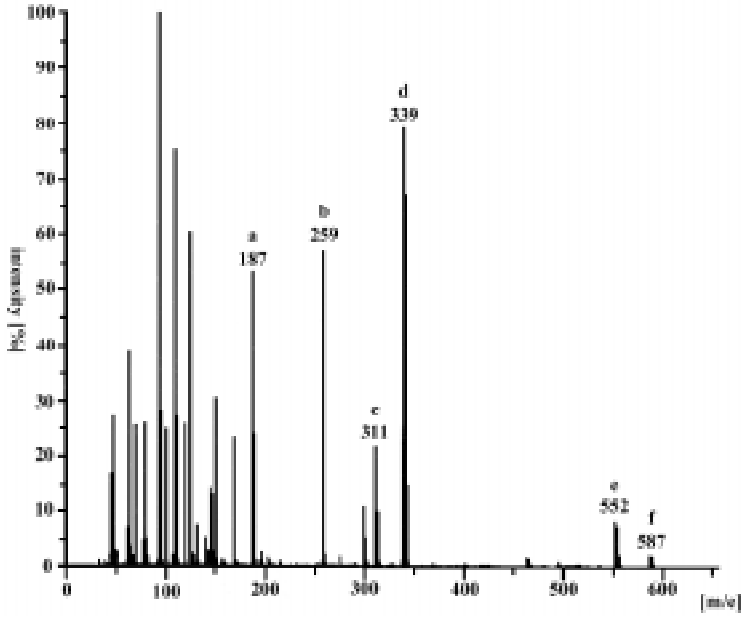

Fig. 1. EI mass spectrum of the complex $[Cu_2\{P(OMe)_3\}_2(\mu\text{-}C_3F_7COO)_2]$ (**3**): a) $[Cu\{P(OMe)_3\}]^+$, b) $[C_3F_7COOPMe]^+$, c) $[Cu\{P(OMe)_3\}_2]^+$, d) $[Cu_2(C_3F_7COO)]^+$, e) $[Cu_2(C_3F_7COO)_2]^+$, f) $[Cu_2(C_3F_7COO)\{P(OMe)_3\}_2]^+$

The analysis of the spectra suggests a dimeric structure for the compounds studied and points to the fragmentation scheme shown in Fig. 2.

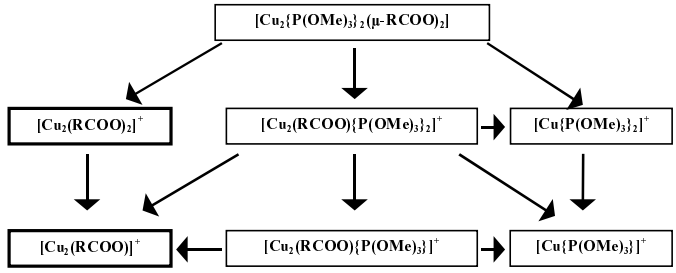

Fig. 2. Fragmentation scheme for the complexes $[Cu_2\{P(OMe)_3\}_2(\mu\text{-}RCOO)_2]$

Among the fragments including copper, the highest intensity was exhibited by $[Cu_2(RCOO)]^+$. The maximum intensity of this fragment varied and for **1** 10% was reached at 441 K, for **3** – 79% at 435 K and 100% in the case of **2** (409 K), **4** (301 K), **5** (470 K), **6** (362 K), **7** (497 K). The lower temperatures were observed for the complexes **2**, **4** and **6** containing the even number of carbons in the carboxylate chain. The compound **4** having the lowest temperature was studied using temperature-variable IR spectroscopy.

3.3. Temperature-variable IR

Temperature-variable IR spectra (296–463 K) recorded for the complex **4** are shown in Fig. 3. Among the bands characteristic of **4** we have chosen: 1682 cm^{-1}

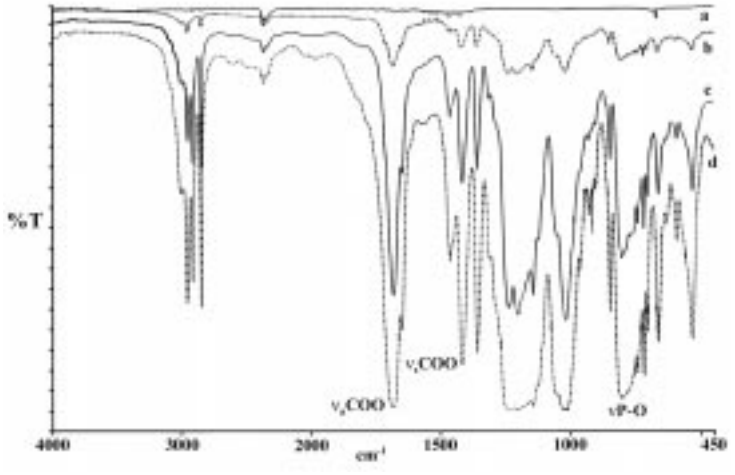

Fig. 3. Temperature-variable IR spectra of $[Cu_2\{P(OMe)_3\}_2(\mu\text{-}C_6F_{13}COO)_2]$ (**4**):
a) t = 0 min, T = 296 K; b) t = 30 min, T = 343 K; c) t = 71 min, T = 413 K;
d) t = 86 min, T = 463 K; t – time, T – temperature

(ν_aCOO), 1417 cm^{-1} (ν_sCOO) and 804 cm^{-1} (νP-O) [10, 11]. Because only the intensity of these bands was increasing during heating, we conclude that only the molecular form of $[Cu_2\{P(OMe)_3\}_2(\mu\text{-}C_6F_{13}COO)_2]$ (**4**) was present in the gas phase. Therefore the complex can be transported as a vapour to the CVD reaction chamber.

4. Conclusions

The thermal analysis data suggests that the compounds studied can be used in CVD of copper oxide films. The decomposition product can be modified however depending on the conditions of the deposition technique. The mass spectra and temperature-variable IR data analysis pointed to $[Cu_2\{P(OMe)_3\}_2(\mu\text{-}C_6F_{13}COO)_2]$ (**4**) as the most suitable potential liquid CVD precursor among the complexes studied.

Acknowledgements

The authors wish to acknowledge the support from the Polish Committee for Scientific Research (KBN) grant No 4 T08C 03923.

References

[1] SZŁYK E., ŁAKOMSKA I., GRODZICKI A., Polish J. Chem., 68 (1994), 1529.
[2] SZŁYK E., ŁAKOMSKA I., GRODZICKI A., Polish J. Chem., 69 (1995), 1103.
[3] SCHULTZ D.L., MARKS T.J., Adv. Mater., 6 (1994), 719.
[4] SZŁYK E., ŁAKOMSKA I., GRODZICKI A., *Trends in Coordination Chemistry*, Slovak Technical University Press, Bratislava, 1995, p. 151.
[5] SZŁYK E., PISZCZEK P., ŁAKOMSKA I., GRODZICKI A., SZATKOWSKI J., BŁASZCZYK T., Chem. Vap. Deposition., 6 (2000), 105.
[6] SZŁYK E., SZYMAŃSKA I., Polyhedron, 18 (1999), 2941.
[7] *Powder Diffraction File*, Sets 5-667; Joint Committee on Diffraction Standards, 1977.
[8] NYQUIST R.A., KAGEL R.O., *Infrared Spectra of Inorganic Compounds*, Academic Press, New York, 1971, pp. 186–187.
[9] DE LUCCA NETO V.A., MAURO A.E., SARGENTELLI V., IONASHITRO M., Thermochim. Acta, 260 (1995), 235.
[10] NAKAMOTO K., *Infrared and Raman Spectra of Inorganic and Coordination Compounds*, Wiley, New York, 1978, p. 230.
[11] *Atlas IK-spectrov fosforoorganicheskikh soedinienij*, Nauka, Moscow, 1977.

Received 3 April 2003
Revised 15 April 2003

Materials Science, *Vol. 21*, *No. 2*, *2003*

Zeta potential and doping in polyaniline dispersions

D. W. O. DE MEDEIROS[1], D. S. DOS SANTOS[2], T. N. C. DANTAS[1], M. R. PEREIRA[1], J. A. GIACOMETTI[3], J. L. C. FONSECA[1]*

[1]Departamento de Química, Universidade Federal do Rio Grande do Norte, Lagoa Nova, Natal, C. P. 1662, RN 59078-970, Brazil

[2]Grupo de Polímeros "Prof. Bernhard Gross", Instituto de Física de São Carlos, Universidade de São Paulo, C. P. 369, São Carlos, SP 13560-970, Brazil

[3]Faculdade de Ciências e Tecnologia de Presidente Prudente, Universidade Estadual Paulista, C. P. 467, Presidente Prudente, SP 19060-900, Brazil

Polyaniline (PAni) has been classified as an intractable polymer, particularly in its conducting form, the emeraldine salt (ES). Therefore one can consider the mixture of water and PAni as a suspension. The conducting form of PAni can be obtained by a doping process known as "acid doping", in which a strong acid turns PAni from its insulating form, the emeraldine base (EB), into the conducting form, the emeraldine salt. With the objective of establishing a correlation between the doping level and the zeta potential of polyaniline dispersions, polyaniline + HCl aqueous suspensions were prepared. Positive zeta potential values for the various suspensions of PAni showed that it acquired positive charges after the doping process. It was also observed an increase in zeta potential values as HCl concentration increased, which could be correlated to UV-visible spectra of PAni suspensions.

Key words: *polyaniline; electrophoretic mobility; zeta potential; doping*

1. Introduction

Polymers derived from organic compounds, with π-electron conjugation and high dopant concentration, are termed conducting organic polymers [1]. These polymers have been extensively studied by researchers due to their large variety of applications, such as rechargeable batteries [2], electrochromic devices [3] and luminescent materials [4] in optical devices. Among these polymers, polyaniline (PAni) is at an

*Corresponding author, e-mail: jlcfonseca@uol.com.br.

outstanding position, mainly due to the relatively simple experimental methods used in its synthesis [5]. This polymer may occur in different redox states, the main structures, as shown in Fig. 1, being leucoemeraldine (LEB), emeraldine (EB), and

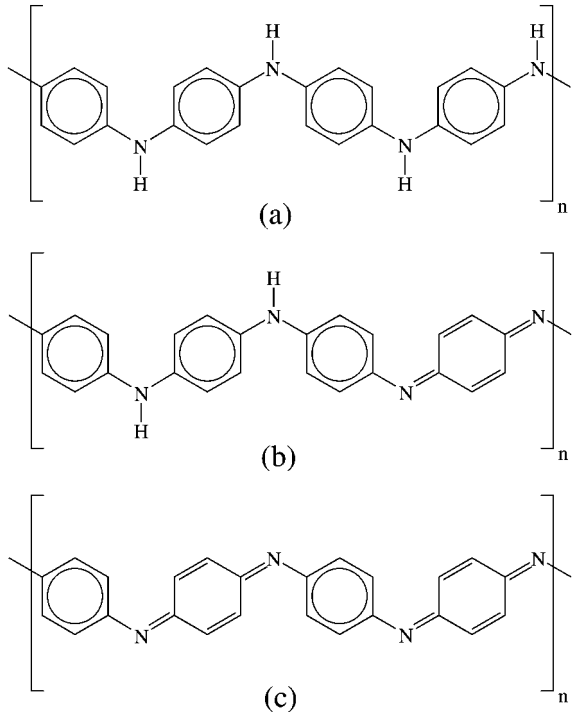

Fig. 1. Basic structures of polyaniline: a) leucoemeraldine base, b) emeraldine base, c) pernigraniline base

pernigraniline (PGB) [6]. All these basic forms are insulating ones. Doping is the reason for the high conductivity and other unique properties of conducting polymers [7]. The fundamental process of doping is a reaction of charge transfer between the organic polymer and a dopant: when charges are removed (or added) to a polymer chain through a chemical reaction, the geometric parameters, such as bond angles, lengths and hybridization, are modified, resulting in a drastic change in conductivity, the levels of doping and oxidation being the most important factors affecting the electric properties of polyaniline [8]. Different dopants produce polyanilines with different properties, suitable for specific applications [9, 10]. As an example, in the case of PAni films, one can find reported in the literature doping by chorona discharge [11]. In fact, one of the most common mechanisms of doping of polyaniline, according to the literature, is known as acid doping, where strong mineral acids change the insulating form EB into the saline conductive one ES [12], as displayed in Fig. 2.

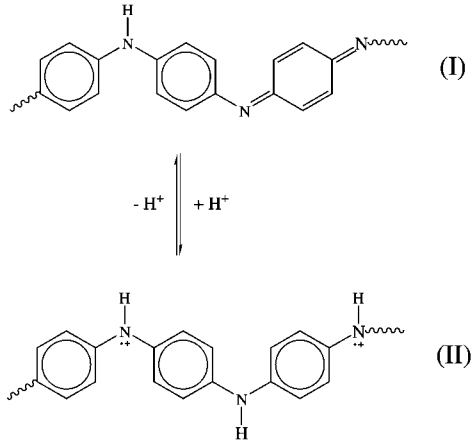

Fig. 2. Scheme representing doping of EB polyaniline for the obtention of emeraldine salt (ES)

Although acid doping occurs without any variation in the number of electrons of the polymeric chain, the protons introduce positive charges there. As a consequence, chemical interaction can be described as a two-stage process [13]:

$$EB + HA \rightarrow EB(H\text{–}A)_{adsorbed} \tag{1}$$

and

$$EB(H\text{–}A)_{adsorbed} \rightarrow EB\text{–}H^{+} + A^{-} \tag{2}$$

where Eq. (1) represents the interaction of the imine polymer group with the acceptor molecule H–A, through hydrogen bonding, and Eq. (2) is the charge separation process in these adsorption complexes. Obviously the acid molecules may react with EB in a similar way and, in a strongly acid medium, the last reaction is equivalent to the acid doping and to the conversion of EB into ES. In this way, we can describe the acid doping of EB as an interaction donnor-acceptor followed by charge separation (charge transfer) in the formed complex. The hydrogen bond given by an acceptor molecule is incorporated to the donnor molecule in the second stage of the transformation.

Polyaniline has frequently been classified as an intractable polymer, particularly in its conductive form, the emeraldine salt (ES). It is feasible, as a consequence, to consider the mixture of polyaniline and water as a colloidal suspension [14], which, depending on the application, may become a problem for the processing of this polymer. As a consequence, the study of particle interactions in these colloids, together with new methods of preparation represents an important step for obtaining dispersions which could be used in an increasingly wider range of technological applications [15]. Regarding particle morphology, Stejskal et al. [16, 17] have analyzed the influence of experimental conditions on the particle shape and size of polyaniline dispersions stabilized by different hydrophilic polymers.

In any colloidal system, several aspects of its behaviour (e.g. rheology [18] and stability [19, 20]) are highly governed by particle–particle particle–solvent interac-

tions. Regarding purely electrostatic interactions, these interactions have been described by the so-called DLVO theory [21], one of its main parameters being the ζ potential, which is defined as the electrical potential at the particle double layer shear plane [22]. This potential, in its turn, is governed by surface particle charges: the higher the density of positive charges, the more positive this potential will be (the opposite being true for negative charges) [23]. The aim of this work is to correlate the level of doping of polyaniline particles (in aqueous suspensions) with ζ potential values of these very particles and relate these data to measurements of electromagnetic absorption in the UV-visible region.

2. Experimental

The polyaniline used in this work was synthesized at the Instituto de Física de São Carlos as described in the literature [24]. The suspensions of PAni in dilute HCl were obtained by the dispersion of 0.05 g of PAni in 50 cm^3 of aqueous solution of HCl. Bidistilled water was used in all experiments. The suspensions were prepared with HCl solutions with the following concentrations: 0.2 $mmol/dm^3$, 1 $mmol/dm^3$, 2 $mmol/dm^3$, 4 $mmol/dm^3$, 6 $mmol/dm^3$, and 8 $mmol/dm^3$. The dispersions were sonicated for 60 s and left at a room temperature for 24 h, since it has been found that sonication of PAni-containing particles would result in their desintegration, generating unstable nanoparticles, which undergo fractal aggregation [25]. Afterwards, ζ potential and electromagnetic absorption measurements were carried out.

2.1. Electrophoretic mobility and ζ potential measurements

The electrophoretic mobility measurements μ_E were carried out using a Zeta-Meter System 3.0+ (Zeta-Meter Inc., USA). The ζ potentials of the polyaniline suspensions were calculated from μ_E by employing the Smoluchowski relationship, assuming that $\kappa a << 1$, where κ is the Debye–Hückel parameter and a is the radius of the particles [26]:

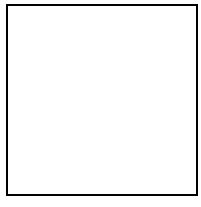

(3)

where ε_0 is the permittivity of vacuum, ε is the relative electric permittivity of water, and η is the viscosity of the disperser phase.

2.2. UV-visible spectroscopy

UV-visible absorption spectra of the suspensions were obtained using a Cary spectrophotometer, model 1E, at room temperature.

3. Results and discussion

Figure 3 displays the values of ζ potential for the polyaniline particles as a function of pH of the disperser phase. One can observe that all potential values are positive, indicating that polyaniline acquired positive charges as a consequence of doping, as discussed before. One can also observe that, as pH decreases, ζ potential increases. It is due to the fact that as more H^+ ions are present in the disperser phase, more polyaniline chains will be doped, implying an increase in the charges on these chains (and, consequently, on the particles surface). As a consequence they move faster than the less doped particles when submitted to the same potential gradient. Butterworth et al. [27] have found the same results with polyaniline synthesized *in situ* with ultrafine silica. In this case, the effect could not be solely related to PAni doping, since polymerization conditions resulted in obtaining particles with a "raspberry" morphology, resultant of bridging flocculation of silica through polyaniline-oxide interaction: as a consequence, an increase in ζ potential with the acid concentration could also be the outcome of neutralization of negative sites which may exist on the silica surface [28].

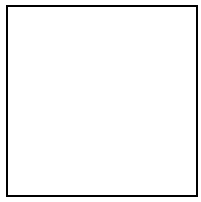

Fig. 3. ζ potential as a function of pH for polyaniline dispersions

If, as seen in the zeta potential measurements, the change in ζ potential for pure polyaniline were due to doping, these changes should be related to changes in the UV-visible absorption spectra of these dispersions. This relation is depicted in Fig. 4, in which UV-visible absorption spectra are plotted as a function of pH for polyaniline dispersions. One can observe in the referred figure that the spectra gradually change from the emeraldine base (pH = 5.6), and, in the more acid conditions (pH = 2.2), the changes in the structure of polyaniline are much more evident in the spectrum, which is characteristic of the emeraldine salt, the doped form of polyaniline [29, 30]: the bands which arise at 435 nm and 720 nm are attributed to the electronic excitation of benzenoid and quinoid rings; increase in protonation of imine groups firstly results in the occurrence of polarons and further protonation results in an increase in the range

of polaron-related conjugation, resulting in a decrease in polaron band energy (shift from 720 nm to 860 nm, blue to dark green). The band at 338 nm appears due to the transition of the conjugated aromatic ring [31], more specifically to a π-π^* transition.

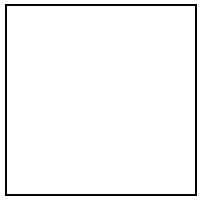

Fig. 4. UV-visible absorption spectra of polyaniline dispersions

According Banerjee et al. [32], polyaniline dispersions should not present more changes in UV-visible spectra for pH below 4, but they observed these changes in PAni–PMVE dispersions; they attributed them to different particle sizes or different macromolecular chain packing: if the same is true for our experiments, it could be the case that, in the present work, pH has influenced macromolecular packing and/or particle size of redispersed PAni; however, in order to inequivocally affirm it for our experiments, light scattering measurements would be necessary.

4. Conclusion

Zeta potential measurements may be used to characterize doping in polyaniline suspensions. The values of zeta potential increase with increasing doping degree of these polymers, as can be confirmed by UV-visible absorption spectroscopy.

Acknowledgments

The authors thank Brazil's Conselho Nacional de Desenvolvimento Científico e Tecnológico (CNPq), Ministério da Ciência e Tecnologia (MCT), Fundação Coordenação de Aperfeiçoamento de Pessoal de Nível Superior (CAPES), Banco do Nordeste, and Pró-Reitoria de Pesquisa e Pós-Graduação da Universidade Federal do Rio Grande do Norte (PPPg-UFRN) for financial support during the course of this work.

References

[1] SYED A.A., DINESAN M.K., Talanta, 38 (1991), 815.
[2] RAHMANIFAR M.S., MOUSAVI M.F., SHAMSIPUR M., J. Power Sources, 110 (2002), 229.
[3] MALTA M., GONZALES E.R., TORRESI R.R., Polymer, 43 (2002), 5895.
[4] DIMITRIEV O.P., KISLYUK V.V., Synth. Met., 132 (2002), 87.
[5] MATTOSO L.H.C., MACDIARMID A.G., EPSTEIN A.J., Synth. Met., 68 (1994), 1.
[6] KANG E.T., NEOH K.G., TAN K.L., Prog. Polym. Sci., 23 (1998), 277.
[7] BARISCI J.N., INNIS L.A.P., KANE-MAGUIRE L.A.P., NORRIS I.D., WALLACE G.G., Synth. Met., 84 (1997), 181.

[8] SULIMENKO T., STEJSKAL J., KŘIVKA I., PROKEŠ J., Eur. Polym. J., 37 (2001), 219.
[9] DOMINIS A.J., SPINKS G.M., KANE-MAGUIRE L.A.P., WALLACE G.G., Synth. Met., 129 (2002), 165.
[10] ZHAN C., ZENG J., YANG X., QIN J., LI Y., Synth. Met., 101 (1999), 731.
[11] JOB A.E., GIACOMETTI J.A., HERRMANN P.P., MATTOSO L.H.C., J. Appl. Phys., 87 (2000), 3878.
[12] HWANG G.W., WU K.Y., LEE H.T., CHEN S.A., Synth. Met., 92 (1998), 39.
[13] MATVEEVA E.S., Synth. Met., 83 (1993), 89.
[14] SU S.J., KURAMOTO N., Synth. Met., 108 (2000), 121.
[15] SOMANI P.R., Mater. Chem. Phys., 77 (2003), 81.
[16] STEJSKAL J., KRATOCHVÍL P., HELMSTEDT M., Langmuir, 12 (1996), 3389.
[17] STEJSKAL J., ŠPIRKOVA M., RIED A., HELMSTEDT M., MOKREVA P., PROKEŠ J., Polymer, 40 (1999), 2487.
[18] ZHOU Z.W., SCALES P.J., BOGER D.V., Chem. Eng Sci., 56 (2001), 2901.
[19] BAUER D., BUCHHAMMER H., FUCHS A., JAEGER W., KILLMANN E., LUNKWITZ K., REHMET R., SCHWARZ S., Coll. Surf. A: Physicochem. Eng. Aspects, 156 (1999), 291.
[20] FUCHS A., KILLMAN E., Colloid Polym. Sci., 279 (2001), 53.
[21] MISSANA T., ADELL A., J. Colloid Interf. Sci., 230 (2000), 150.
[22] MONCHO A., MARTINEZ-LOPEZ F., HIDALGO-ALVA, Coll. Surf. A: Physicochem. Eng. Aspects, 192 (2001), 215.
[23] OHSHIMA H., J. Colloid Interf. Sci., 248 (2002), 499.
[24] MATTOSO L.H.C., MANOHAR S.K., MACDIARMID A.G., EPSTEIN A.J., 33 (1995), 1227.
[25] CHATTOPADHYAY D., BANERJEE S., CHAKRAVORTY D., MANDAL B.M., Langmuir, 14 (1998), 1544.
[26] HUNTER R.J., Colloid. Surface. A: Physicochem. Eng. Aspects, 195 (2001), 205.
[27] BUTTERWORTH M.D., CORRADI R., LASCELLES S.F., MAEDA S., ARMES S.P., J. Colloid Interf. Sci., 174 (1995), 510.
[28] NAWROCKI J., J. Chromatogr. A, 779 (1997), 29.
[29] MCCALL R.P., GINDER J.M., LENG L.M., YE H.J., MANOHAR S.K., MASTERS J.G., ASTURIAS G.E., MACDIARMID A.G., EPSTEIN A.J., Phys. Rev., B41 (1990), 5202.
[30] MASTERS J.G., SUN Y., MACDIARMID A.G., EPSTEIN A.J., Synth. Met., 41 (1991), 715.
[31] MALINAUSKAS A., HOLZE R., Synth. Met., 97 (1998), 31.
[32] BANERJEE P., BHATTACHARYYA S.N., MANDAL B.M., Langmuir, 11 (1995), 2414.

Received 23 April 2003
Revised 19 May 2003